University of Namur

DOCTOR OF SCIENCES

Nonlinear spectroscopy and microscopy studies of fluidic frictions on organic films and of molecular pattern formation by fast micro-contact printing

Lis, Dan

Award date:
2009

Awarding institution:
University of Namur

Link to publication

UNIVERSITY
OF NAMUR
FUNDP

Faculté des Sciences
Centre de recherche en Physique de la
Matière et du Rayonnement (PMR)

Rue de Bruxelles, 61
B-5000 Namur
Tél. +32 (0)81 724490
Fax +32 (0)81 724464
E-mail : dan.lis@fundp.ac.be

Nonlinear spectroscopy and microscopy studies of fluidic frictions on organic films and of molecular pattern formation by fast micro-contact printing

Dissertation présentée par
Dan Lis
en vue de l'obtention du grade de
Docteur en Sciences
Novembre 2009

Composition du Jury :

Dr Yves Caudano
Prof. Benoît Champagne
Dr André Peremans (promoteur)
Dr Abderrahmane Tadjeddine
Prof. Jean-Pol Vigneron

Rempart de la Vierge, 13
B – 5000 Namur (Belgique)

Imprimé en Belgique
ISBN : 978-2-87037-660-7
Dépôt légal : D / 2009 / 1881 / 47

Facultés Universitaires Notre-Dame de la Paix
Faculté des Sciences
Centre de recherche en Physique de la Matière et du Rayonnement
Rue de Bruxelles, 61 – 5000 Namur, Belgique

Etude par spectroscopie et microscopie non linéaires de la friction fluidique sur des films organiques et de la formation rapide de motifs moléculaires par micro impression de contact

par Dan Lis

Résumé:

Nous avons développé les outils théoriques nécessaires nous permettant d'extraire la conformation moléculaire de données fournies par la spectroscopie de génération de fréquence-somme et du second harmonique (SFG & SHG).

La génération du second harmonique nous a permis de caractériser la réorientation d'un colorant (molécule de rhodamine 6G), physisorbé à l'interface solide-liquide, et cela consécutivement à la friction induite par un fluide en mouvement. Cette observation permet de reconsidérer la condition de «non glissement» établie dans la théorie de la mécanique des fluides.

Par la suite, nous avons étudié la cinétique de formation de motifs de monocouches auto-assemblées (SAM), ces derniers étant réalisés par micro-impression de contact (µcp). La possibilité de former des SAM hautement structurées endéans des durées d'impression aussi brèves que 1 seconde, a été démontrée. Celles-ci font état d'une qualité de conformation identique à celle résultant des méthodes d'immersion classiques, et peuvent de surcroit présenter des motifs moléculaires de dimensions micrométriques.

Par après, nous montrons la possibilité de produire des motifs de molécules amphiphiles sur un substrat solide en combinant les méthodes de µcp et de Langmuir-Blodgett.

Finalement, le développement d'un microscope SFG est présenté, ainsi que les premières images de motifs de monocouches moléculaires réalisés par µcp.

Disertation doctorale en Sciences physique

Le 11 décembre 2009
Centre de recherche en Physique de la Matière et du Rayonnement
Promoteur : Dr André Peremans

University of Namur (FUNDP)
Faculty of Sciences
Research Centre in Physics of Matter and Radiation
Rue de Bruxelles, 61 – 5000 Namur, Belgium

Nonlinear spectroscopy and microscopy studies of fluidic frictions on organic films and of molecular pattern formation by fast micro-contact printing

by Dan Lis

Abstract:

We develop on the one hand, theoretical tools allowing us to extract the molecular conformation from sum-frequency and second harmonic generation spectroscopy (SFG & SHG) data.

First, the SHG spectroscopy is employed to characterize the reorientation of rhodamine 6G dye molecules induce by the friction of a moving fluid at the solid-liquid interface. This observation enables to revisit the “no slip” condition of the fluid mechanics theory.

Then, we study the formation kinetics of patterned self-assembled monolayers (SAM) realized by micro-contact printing (µcp). We demonstrate the possibility of building highly structured SAMs within time durations as short as 1 second. These layers possess a conformational quality identical to those resulting from standard immersion methods and may furthermore present molecular patterns of micrometric dimensions.

Next, we show the possibility of realizing solid supported patterns of amphiphilic monolayers by combining µcp and Langmuir-Blodgett methods.

Finally, the development of a SFG microscope is presented along with the first images of SAMs patterns realized by µcp method.

Ph.D. thesis in physical Sciences
November 22th 2009
Research Centre in Physics of Matter and Radiation
Advisor: Dr. André Peremans

Acknowledgments

I would like to express my special thanks to the members of my committee. We all know that, although being an impalpable substance, time appears to be so precious… thank you for yours. Particular thanks to my thesis promoter, Dr. André Peremans for transferring me a part of his precious knowledges. Those valuable skills have successfully helped me to get along in the arena of optical developments, widely required during this thesis. I am especially indebted to Professor Paul Thiry for his meticulous help in many circumstances, his precious advises and his unbreakable optimism. I underline his will to give the means to students to run their projects and ideas through available financial and technical supports.

I would like to express my gratitude as well to the Dr. Alaa Adin Mani for the time we spend together around laser systems and for the precious instructions he gave me on accuracy and patience. Thanks go also to Dr. Laurent Dreesen for giving me tips on the way to handle the SFG spectrometer. Special gratefulness is expressed to my colleagues and friends Dr. Francesca Cecchet and Dr. Yannick Sartenaer. Thanks to you Francesca to let me enter your world of interest for surface sciences. We spend much time in trying to make run or improve a broad panel of experimental devices/processes/methods, and it has always been in a good mood. Your omnipresent help and fruitful scientific ideas have enabled me to overcome many problems and have broadened my scientific horizon. Thanks to you for sharing that with me all along those four years of thesis. Besides, I would like to thank Yannick, for your high didactical capacity that has allowed me to softly integrate the basis of the biology world (…I say basis.. we are physicist!) or at least how to handle and prepare DNA samples (not so glorious after all…). I thank you also as a fiend for the numerous laugh out loud moments we share in the office and in the lab. My thanks go also to Dr. Cedric Volcke for his irreplaceable humour and friendship, although he has spent too much time in Ireland.

Of course, I thank my colleague Laurent Lamard. Even if our research projects do not overlap much, we try ourselves to many funny optical tests to validate passionate discussions, some being unfortunately not feasible because of technical limitations, but also for having share rewarding experiences in live during our holiday treks. I thanks as well my old classmates Nicolas and Matthieu for the many activities spend together, lots of happy memories. This would not go

without the whole academic friend team, thank to Bénédicte, Gilles, Bastien, Frédéric, Xavier, Ludo and all others…

I thanks Dr. Gérard Tourillon for is sharp experience in chemistry as well as Ernest Kakoudji and Laurent Grawet for their help in domains where my incompetence is appreciable, that is among others, electronic, plug-in…; and finally I would like to thanks Vincent Bruyninckx.

I express my gratitude to Dr. Julien Guthmuller and the CTA team for a fruitful collaboration on theoretical simulation. I thank as well the CLIO team (University of Paris) for technical support, and especially Dr. Christophe Humbert and Dr. Bertrand Busson. I thank the Fund for Agricultural and Industrial Research (FRIA) for my four years doctoral grant and the National Fund for Scientific Research (FRS-FNRS) for my 3 month fellowship in 2007. Thanks go also to Professor Steve Granick (University of Illinois) and his team members for their warm welcome and the exciting collaboration with researcher from all over the world.

And finally, I would like to thanks my mother and sister, Michelle and Ména for their support. Even if you don’t know exactly what I have done during all those years, you have always been full of enthusiasm and have endured the odd behavior of a physicist. I thank my cousin Eric for his precious help on lithography processes.

Contents

General introduction

In the human seeking to understand the world under both its macroscopic and microscopic aspects, a wide panel of tools and techniques have been developed by scientists over centuries for providing answers to so many raised questions. Among them, the spectroscopy of the matter characterizes the distribution of one observable quantity as a function of one probe property variation (energy, mass, …). The general expression of probe encompasses electromagnetic waves (radiofrequency, IR, visible, UV, X, gamma), as well as particles (electrons, other ions, …).

It is interesting to notice that the specific case of optical spectroscopies, dealing with UV-visible and IR sources, has played an important role in the history of physics. From the white light analysis by Newton, the resolution of the black body emission in the UV by Planck leading to the energy quantum, and the study of the hydrogen atom spectrum successfully explained through quantum mechanics, many interaction problems between atoms-molecules and photons have been solved through optical spectroscopy applications. It includes a great part of our knowledges about atomic and molecular structures, but also stars, nebulas, galaxies …, that is both microscopic and macroscopic worlds as aforementioned.

From a practical side, optical spectroscopies are non destructive techniques allowing to study solid, liquid and gaseous phases in their volumes or interfaces, as long as the optical probe has access to the targeted location (which involves buried interfaces). Some typical informations that may be retrieved are the determination of rotational, vibrational or electronic energy levels allowing chemical, physical and structural characterizations. Among the many kinds of optical spectroscopies, we will focus all along this thesis on second-order nonlinear mechanisms which require the combination of two distinct photons as a probe.

The first three chapters of this work are dedicated to theoretical considerations about nonlinear optical processes. They will show that such kind of spectroscopy is surface specific, is able to furnish the orientation of the investigated molecular systems and is sensitive to the material structure. By using adequate mathematical tools, we will characterize the optical intensities, see how to extract informations from experimental spectra, and review the different optical processes involved regarding the laser wavelengths,. . ..

From their particular specificities, second-order nonlinear spectroscopies turn out to be suitable to study the molecular organization at interfaces as well as the vibrational and/or electronic dipole transitions associated to the involved chemical components. In the Lasmos/LLS laboratory, those techniques are dedicated to characterize model biochemical films such as lipids (cell membranes), proteins, polymers (DNA), carbon chains, etc. Furthermore, associated solid supported devices and film construction methods (self-assembled monolayers, micro-contact printing, Langmuir-Blodgett, onto metallic substrates, nanoparticles, insulator prisms. . .) are investigated as well.

In this framework, chapter four discusses a second harmonic generation (SHG) spectroscopy study dedicated to characterizing the buried liquid-solid interface. The mechanical strain induced by a moving fluid on a molecular film enables to evaluate the liquid slip occurring at the probed interface. This optical spectroscopic work, at the heart of fluid mechanics, provides accurate informations on a micro-system very sensitive to external disturbances.

Further, we go on with sum-frequency generation (SFG) spectroscopy for a vibrational study of different interfacial systems. After detailing the SFG spectrometer, self assembled monolayers (SAMs) realized by immersion are studied in chapter five to demonstrate the full potential of the molecular conformation retrieval. Next, SAMs realized by the micro-contact printing (μcp) technique are studied as well and compared with those issued from the immersion method, this regarding the quality of the molecular structure. A discussion is given in chapter six about the ability of μcp to form molecular layers of high structural quality within short print durations and, moreover, enabling to produce micrometric molecular patterns.

Chapter seven exposes the Langmuir-Blodgett (LB) technique able to form solid supported lipid films, those latter being investigated by SFG. Next, this LB technique is coupled to μcp in order to pattern lipid layers. Finally, a SFG imaging set up allowing to provide a vibrational map of the interface is presented in the last chapter. This latter enables to give a 2D image of molecular patterns generated by micro-contact printing method.

To summarize, this thesis manages on the one hand, nonlinear optical spectroscopies (SFG, SHG) as well as microscopy, able to give conformational informations (spatially resolved), and, on the other hand, a method allowing to build various molecular patterns on solid substrates (μcp).

Chapter 1

Introduction to nonlinear optics

1.1 Introduction

In this first chapter, the main tools involved in the description of nonlinear spectroscopies are provided. A brief description of the light-matter interaction is given, firstly in a linear approach relatively to the electromagnetic field, then through its power series. The commonly used formalism of the dipolar approximation is adopted after an examination of its validity. Nonlinear optics is then developed within this approximation frame. Then, because of their interface selectivity, we will focused more specifically on second-order nonlinear processes. This particular property will be demonstrated through symmetry consideration of the associated electrical susceptibility. A general expression of the second-order process intensity will be established relatively to the polarization conditions of the light fields. Furthermore, to provide a quantification of those nonlinear phenomena, the modification of intensity undergone during reflection and refraction at interfaces will be described for different experimental configurations through Fresnel coefficients. Along with this, the total interfacial electric field will be provided by the Fresnel factors. Those mathematical expressions will be required afterwards to perform a quantitative analysis through theoretical simulations.

1.2 Linear polarization in matter

The interaction between *light* and *matter* is a fundamental process at the heart of a wide panel of physical phenomena. While the electromagnetic field of an incoming photon is felt at the illuminated surface/interface, it induces in every single molecule a dipole moment $\vec{p}$ (Cm) which can be expressed within the dipolar approximation as:

$$\vec{p}^{(1)} = \varepsilon_0 \overleftrightarrow{\alpha} \cdot \vec{E}, \tag{1.1}$$

where $\overleftrightarrow{\alpha}$ is the microscopic polarizability and " $\cdot$ " is the contracted tensorial product. In the simplest macroscopic description (for which local field effects are neglected), we have to sum over N dipoles per unit volume, the polarization of the matter or electric dipole density (C/m^2) is written as:

$$\vec{P}^{(1)} = N \varepsilon_0 \overleftrightarrow{\alpha} \cdot \vec{E} = \varepsilon_0 \overleftrightarrow{\chi}^{(1)} \cdot \vec{E}, \tag{1.2}$$

with $\overleftrightarrow{\chi}^{(1)}$ the first order electrical susceptibility. This simple expression of the linear polarization is directly proportional to the applied field (supposed homogenous) through the tensor $\overleftrightarrow{\chi}^{(1)}$.

1.3 Nonlinear polarization in matter

In cases where the electric field becomes important, that is to say, of the same order as the Coulombian interaction inside an atomic system, it becomes able to induce anharmonic effects. A general expression of the matter polarization as a function of the power series of the electric field may be written as:

$$\begin{aligned} \vec{P} &= \vec{P}^{(1)} + \vec{P}^{(2)} + \vec{P}^{(3)} + \cdots \\ &= \varepsilon_0 \overleftrightarrow{\chi}^{(1)} \cdot \vec{E} + \varepsilon_0 \overrightarrow{\overleftrightarrow{\chi}}^{(2)} : \vec{E}\vec{E} + \varepsilon_0 \overleftrightarrow{\overleftrightarrow{\chi}}^{(3)} \vdots \vec{E}\vec{E}\vec{E} + \cdots, \end{aligned} \tag{1.3}$$

with $\vec{P}^{(i)}$ the i^{th} order polarization relative to the electric field and $\chi^{(i)}$ the i^{th} order electrical susceptibility tensor. Although the nonlinear susceptibilities are small, especially for higher-order processes, those nonlinear anharmonic effects may become significant if considering large values of the electric field (or resonant effects that intensify the nonlinear susceptibilities.)

Practically, such electric fields can be generated by laser sources, and especially pulsed lasers producing very brief and higly energetic light impulsions. Through those intense sources, optical phenomena of the second, third, fourth order and more may show up [Lee et al., 2006]. Over this thesis, we will however focus on phenomena relying on second-order processes, the polarization behavior of the matter being therefore function of two incident electric fields.

The above theory is defined whitin the dipolar electric approximation frame. This means that any charge distribution is considered only under its monopolar and dipolar natures.

1.4 Validity of the dipolar approximation

The dipolar approximation is widely used, but does it provide a reliable estimation of the physical processes occurring within matter? In this section, we will try to see the validity range of such approximation by illustrated explanations.

The effective polarization (of j^{th} order) induced by an optical field in a medium may be expressed as a series of multipolar terms (dipolar, quadrupolar,...) [Jackson, 2001]:

$$\overrightarrow{P}^{(j)}_{eff} = \overrightarrow{P}^{(j)} + \frac{\mu_0}{i\,\omega}\overrightarrow{\nabla}\times\overrightarrow{M}^{(j)} - \overrightarrow{\nabla}\cdot\overleftrightarrow{Q}^{(j)} + \cdots, \tag{1.4}$$

where $\overrightarrow{P}$, $\overleftrightarrow{Q}$, and $\overrightarrow{M}$ denote electric-dipole polarization, electric-quadrupole polarization, and magnetization, respectively. Higher-order multipoles will be neglected in this discussion since quadrupolar contributions are the most important one after $\overrightarrow{P}$ in the series and should be therefore sufficient to obtain an idea of the dipolar approximation validity. We will consider the expression of the electric field up to its the first derivative:

$$E_i\,(\vec{r}) = E_i\,(\vec{R}) + \sum_j (r_j - R_j)\,\frac{\partial E_i\,(\vec{r})}{\partial r_j}\bigg|_{\vec{r}=\vec{R}}, \tag{1.5}$$

with i, j = x, y, z. Relatively to the origin, the x componant of the electric field is expressed as :

$$E_x\,(\vec{r}) = E_x\,(\vec{0}) + x\,\frac{\partial E_x}{\partial x} + y\,\frac{\partial E_x}{\partial y} + z\,\frac{\partial E_x}{\partial z}, \tag{1.6}$$

which could be rewritten as:

$$E_x\,(\vec{r}) \;=\; E_x\;(\vec{0}) \;+\; \vec{r}\cdot\vec{\nabla}\,E_x\;. \tag{1.7}$$

Finally, the full expression of the electric field is:

$$\vec{E}\,(\vec{r}) \;=\; \vec{E}\;(\vec{0}) \;+\; \vec{r}\cdot\vec{\nabla}\,\vec{E}\;, \tag{1.8}$$

with $\vec{\nabla}\,\vec{E}$ a two dimension matrix.
The first and second-order expressions of the three effective polarization components are the following:

$$\overrightarrow{P}^{(1)}(\omega) \;=\; \epsilon_0\;[\overleftrightarrow{\chi}^{(1)\,D}\cdot\overrightarrow{E}(\omega) \;+\; \overrightarrow{\overleftrightarrow{\chi}}^{(1)\,P} : \overrightarrow{\nabla}\overrightarrow{E}(\omega)]\,, \tag{1.9}$$

$$\overleftrightarrow{Q}^{(1)}(\omega) \;=\; \epsilon_0\;\overrightarrow{\overleftrightarrow{\chi}}^{(1)\,Q}\cdot\overrightarrow{E}(\omega)\,, \tag{1.10}$$

$$\overrightarrow{M}^{(1)}(\omega) \;=\; \epsilon_0\;\overleftrightarrow{\chi}^{(1)\,M}\cdot\overrightarrow{E}(\omega)\,, \tag{1.11}$$

and

$$\begin{aligned}\overrightarrow{P}^{(2)}(\omega) \;=\; &\epsilon_0\;\overrightarrow{\overleftrightarrow{\chi}}^{(2)\,D} : \overrightarrow{E}(\omega_1)\overrightarrow{E}(\omega_2) + \\ &\epsilon_0\;[\overleftrightarrow{\overleftrightarrow{\chi}}^{(2)\,P1} \vdots\; \overrightarrow{\nabla}\overrightarrow{E}(\omega_1)\overrightarrow{E}(\omega_2) + \\ &\qquad\overleftrightarrow{\overleftrightarrow{\chi}}^{(2)\,P2} \vdots\; \overrightarrow{E}(\omega_1)\overrightarrow{\nabla}\overrightarrow{E}(\omega_2)]\,,\end{aligned} \tag{1.12}$$

$$\overleftrightarrow{Q}^{(2)}(\omega) \;=\; \epsilon_0\;\overleftrightarrow{\overleftrightarrow{\chi}}^{(2)\,Q} : \overrightarrow{E}(\omega_1)\overrightarrow{E}(\omega_2)\,, \tag{1.13}$$

$$\overrightarrow{M}^{(2)}(\omega) \;=\; \epsilon_0\;\overrightarrow{\overleftrightarrow{\chi}}^{(2)\,M} : \overrightarrow{E}(\omega_1)\overrightarrow{E}(\omega_2)\,, \tag{1.14}$$

with χ^D, χ^P, χ^Q, and χ^M, the electric dipole-dipole susceptibility, the electric dipole-quadrupole susceptibility, the electric quadrupole-dipole susceptibility (those two latter being related to each other), and the magnetic dipole-electric dipole susceptibility.

We will provide a signification to those terms and see which ones are dominant over the others and under which conditions. Let us first do it with the terms included in the effective first order polarization, since one single field effect is easier to represent. The first step is to understand how the polarization of matter induced by a field and its gradient may lead to an electric dipole contribution, added to an electric quadrupole one and finally, to a magnetic component. Once the different contribution mechanisms understood, it will be easier to see the respective importance of each effect. Let us consider an electric field polarized along z, having a ω pulsation, and being associated to a plane wave with a wave vector $\overrightarrow{K}$ along the x axis as described in figure 1.1.

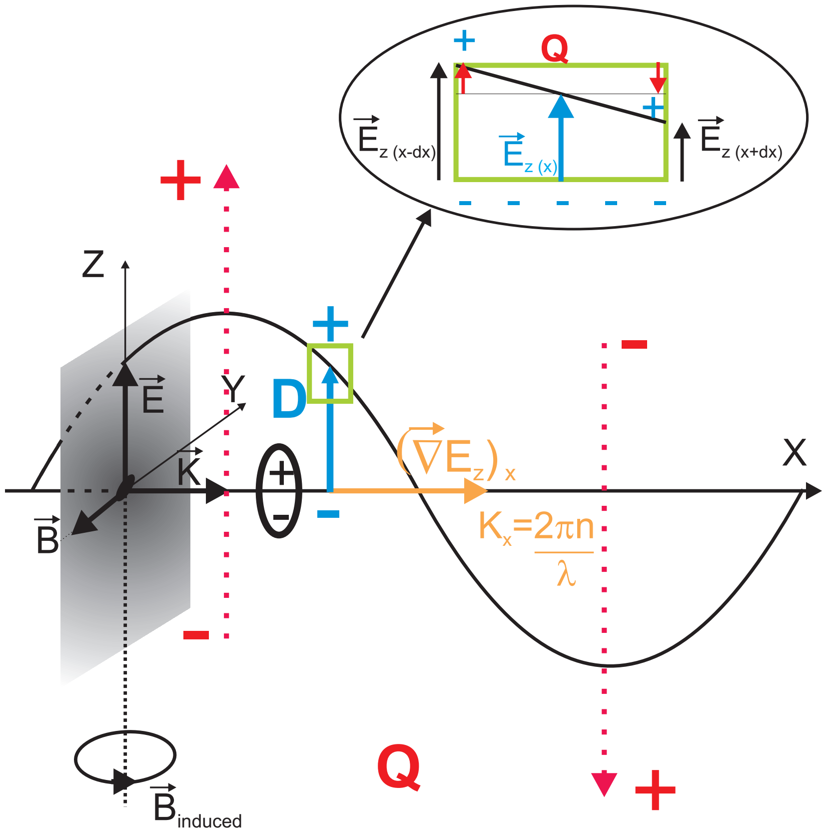

Figure 1.1: *Scheme of a charge repartition behaviour within an electromagnetic field.*

The electric field (blue) will induce a dipolar charge repartition (D blue) of the matter. The intensity of the phenomenon is proportional to the $\overrightarrow{E}$ field through $\overleftrightarrow{\chi}^{(1)D}$ (left part of the equation 1.9). The right part of the same equation (1.9) is associated to the electric field gradient. Its value is extracted from the plane wave function as follows:

$$\vec{E}\,(\vec{r},\,t) \;=\; \vec{E}_0\; e^{\,i\,(\vec{K}\cdot\vec{r}-\omega\,t)}. \tag{1.15}$$

Since we consider a wave plane, we get:

$$\begin{aligned} E_z &= E_{0z}\; e^{\,i\,(K_x\cdot x-\omega\,t)}\;, \\ E_y &= E_{0y} \;=\; 0\;, \\ E_x &= E_{0x} \;=\; 0\;. \end{aligned} \tag{1.16}$$

Consequently, the field gradient components are expressed as follow:

$$\begin{aligned} \vec{\nabla} E_z &= i\; E_{0z}\; K_x\; \vec{e}_x \;=\; (i\,E_{0z}\,K_x,\,0,\,0)\;, \\ \vec{\nabla} E_y &= (0,\,0,\,0)\;, \\ \vec{\nabla} E_x &= (0,\,0,\,0)\;, \\ with \quad K_x &= \frac{2\pi n}{\lambda}\;. \end{aligned} \tag{1.17}$$

Note that this description based on a plane wave may be considered close to the reality. Indeed, the intensity of the electric field in the plane is usually modelized by a gaussian intensity distribution (i.e. the one of a laser beam) centered on the x axis. The gaussian shape is expected to be of macroscopic dimension (fraction of milimeter at best for a regular beam) and thus large in comparison to the wavelength λ. The in-plane intensity can thus be assumed nearly constant on a microscopic scale ($(\vec{\nabla}\,E_z)_z = 0$), validating therefore the plane wave representation.

From this description, it results that the field gradient goes along the x propagation axis and is inversely proportional to the wavelength. The modification of the dipolar charge repartition induced by the electric field gradient is thus smaller for an IR beam than for a visible one. Moreover, if the probed system of charges is considered of molecular dimension (nm), it may be assumed small in comparison to the wavelenghts (IR-Vis, μm). This is true since the matter polarisation is a sum of N dipoles per unit volume, each of them being associated to a single molecule. The electric field gradient acting on such single system of charges is very smooth, and its effect may thus be considered small in front of the field effect itself. Finally, since the wavelengths are large, a reasonable variation of their value do not change much the electric field gradient component (if the IR frequency is scanned i.e.). The field gradient effect may thus be considered as a constant.

This above deduction is done for molecule in a bulk phase, thus without considering interfacial interactions. In a general way, surface and interface may cause a sharp electric field modification. This latter field may be absorbed within small distance (metal) or modified from the different relative dielectic constant involve when entering the new medium. Consequently, strong electric field gradients may show up at interfacial locations with effects that may become important regarding the field effect itself.

The quadrupolar effects, expressed in equation 1.10 and shown in red in figure 1.1 are also function of the frequency through the slope of the sinusoidal wave. The distortion of the dipolar charges repartition is thus a function of the frequency. Once again, if the probed molecular system is considered small in front of the involved wavelength, the quadrupolar effects resulting from the field will be weak (as shown at the top of figure 1.1). Besides, as before, a small variation of the involved wavelength will not induce a noticable variation of the quadrupolar effects, that may thus be considered as constant. Once again, this is valid for a system in bulk phase. Any interactions with surfaces and interfaces are likely to give rise to strong electric field and thus to important quadrupolar effects. Such important contribution have been reported in different works [Guyot-Sionnest et al., 1986] [Zhu and Wong, 1992] [Shen, 1999].

Finally, the third equation (1.11) makes reference to the magnetic field induced by the electric field through the magnetization and resulting from the movement of free charges. This $\vec{B}$ field is rotational and centered on the electric field axis. It may itself in return induce electric fields that modify the dipolar charges repartition. However, to happen, this will require charge motions and a high magnetization ability to become important. Thus it may be ignored in most cases, and especially within organic probed films (insulators), the only exception being in metallic bulk samples. In this particular situation, magnetic effects are considered but as a constant contribution with the frequency.

It may be interesting to notice that two contribution locations have to be considered, one specific to the interface, the other dedicated to the bulk medium crossed by the incident light field. The bulk contribution may usually be considered as far more important than the surface one (especially if we consider an interfacial monolayer) simply because of the higher amount of interacting matter [Guyot-Sionnest and Shen, 1988]. This is however subject to exceptions with cases presenting a weak bulk effect. This study being perfomed mainly on metallic substrates, bulk effects will be assumed to be dominant.

An imporant property that will be demonstrated in section 1.6, states that in the case of even-order nonlinear phenomena (2^{nd}, 4^{th}...), the electric dipole contribution vanishes within centrosymmetric media (the largest part of common bulk phase). Therefore, for this class of nonlinear effects, it makes sense to consider only the surface electric dipole, along with the bulk electric quadrupole and the bulk magnetic dipole. This result is resumed in table 1.1,

Monolayer		Bulk
Dipole $\vec{E}$	>>>	~~Dipole $\vec{E} = 0$~~
~~Dipole $\vec{B}$~~	<<<	Dipole $\vec{B}$
~~Quadrupole $\vec{E}$~~	<<<	Quadrupole $\vec{E}$

Table 1.1: *Multipolar contribution to the polarization for even-order nonlinear effects in a medium with inversion symmetry.*

The overall consequence is that within a studied thin film, the dipolar effects are important and isolated since they are usually forbidden in the centrosymmetric bulk. The pure electric dipolar part is highly dependent on the frequency (through energy transition moment, either electronic or vibrational), even if the field gradient is considered as a constant (see equation 1.9). The quadrupolar effect is dominated by the bulk (we assume so for metallic interfaces at least) and may also be assumed as a constant over the spectroscopic measurement, as well as magnetic contribution (if the bulk is metallic, if not it is negligible). The dipolar approximation frame may therefore be adopted to deal with frequency resonant process, while the neglected effects will show up under the form of a non resonant frequency independent contribution. This constant intensity background includes mainly effects from the substrate and does not preclude the interpretation of the spectroscopic results.

Notice that the relative importance of those different contributions greatly depends upon the beam polarizations, the experimental set-up (reflection at a metallic interface, total internal reflection in a prism...), the wavelengths involved... [Corn and Higgins, 1994] [Guyot-Sionnest et al., 1986] [Tepper et al., 1990] [Zhu and Wong, 1992].

1.5 Second-order polarization

In order to isolate the different effects taking part in second-order processes, let us consider two distinct electric fields interacting with some matter. Those fields oscillate at pulsations ω_1 and ω_2, are electrically polarized along Z and propagate in the OX direction. In x=0, we get:

$$\begin{aligned} E_1(t) &= E_{1z}\cos(\omega_1 t)\,, \\ E_2(t) &= E_{2z}\cos(\omega_2 t)\,. \end{aligned} \tag{1.18}$$

The second-order electric polarization (for instance the one along x) resulting from this light-matter interaction is expressed as:

$$\begin{aligned} \mathrm{p}_x^{(2)} &= \epsilon_0\,\chi_{xzz}^{(2)}\,(E_1(t)+E_2(t))\,(E_1(t)+E_2(t)) \\ &= \epsilon_0\,\chi_{xzz}^{(2)}\,E_1^2(t) + \epsilon_0\,\chi_{xzz}^{(2)}\,E_2^2(t) + 2\,\epsilon_0\,\chi_{xzz}^{(2)}\,E_1(t)\,E_2(t)\,, \end{aligned} \tag{1.19}$$

which gives after some trigonometric manipulations:

$$\begin{aligned} \mathrm{p}_x^{(2)} &= \epsilon_0\,\chi_{xzz}^{(2)}\,\frac{E_{1z}^2}{2} + \epsilon_0\,\chi_{xzz}^{(2)}\,\frac{E_{2z}^2}{2} \\ &+ \epsilon_0\,\chi_{xzz}^{(2)}\,\frac{E_{1z}^2}{2}\,\cos(2\omega_1 t) \\ &+ \epsilon_0\,\chi_{xzz}^{(2)}\,\frac{E_{2z}^2}{2}\,\cos(2\omega_2 t) \\ &+ \epsilon_0\,\chi_{xzz}^{(2)}\,E_{1z}\,E_{2z}\,\cos[(\omega_1+\omega_2)t] \\ &+ \epsilon_0\,\chi_{xzz}^{(2)}\,E_{1z}\,E_{2z}\,\cos[(\omega_1-\omega_2)t]\,. \end{aligned} \tag{1.20}$$

The first term shows an electric field of null frequency, that is to say a permanent polarization originating from the presence of electric charges at the surface of the illuminated material. This phenomenon, defined as the "optical rectification" produces a static field from a dynamic one. The next two terms show frequencies amounting to twice the incident ones. The resulting light waves are associated to the "second harmonic generation" (SHG) process. The fourth term is related to the "sum-frequency generation" (SFG) process for which a new photon of frequency amounting to the sum of both incident photon ones is produced. Finally, the last one refers to the "Difference-frequency generation" (DFG) also called "parametric mixing process". In this case, the new generated photon has a frequency equal to the positive difference between the two incoming photon ones. Note that if the two incoming photons have the same angular frequency $\omega_1 = \omega_2$, the DFG process is nothing else than the optical rectification, while the SHG and SFG processes are identical. Therefore, the five phenomena are initiated from the last two ones only, the first three being only particular cases when the two photons come from the same source.

Equation 1.20 shows the relationship between the component of the nonlinear polarization vector and the different components of the susceptibility tensor through the particular choice of the polarization. It appears possible, by performing an appropriated choice of the three beam polarizations, to quantify each tensor component value directly from the polarization amplitude. However, while a s polarized beam (that is an electric field polarization perpendicular to the incident plane) probes well the "y" component of the tensor only, a p polarized beam (that is an electric field polarization parallel to the incident plane) involves both the "x" and "z" components, as depicted in figure 1.2.

The only way to isolate a pure "z" or "x" component would be to send the incoming beam with an incidence angle θ of 90° or 0°, respectively, which is however not a regular configuration (especially because the Z component of the total interfacial electric field undergoes a very sharp drop for θ close to 90°, see section 1.8, figure 1.6, along with the experimental impossibility to reach 90°). If the experiment is not carried out in this particular set up, an individual quantification of the χ component is not allowed unambiguously since for a fixed polarization configuration, the corresponding matter polarization term will be described by more than one susceptibility component.

To overcome this problematic situation, it is interesting to take advantage of the intrinsic symmetry properties of the susceptibility tensor that could greatly simplify the tensor structure.

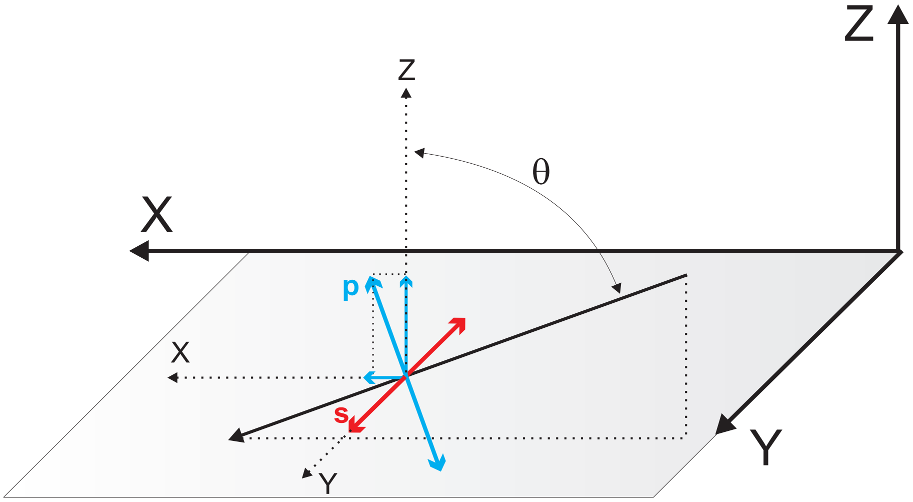

Figure 1.2: Scheme of p and s polarization component projections on the xyz axes.

1.6 Symmetry properties of the $\chi^{(2)}$ tensor

1.6.1 Centrosymmetric materials

One major property of nonlinear optical phenomena relies on the central symmetry notion. In a centrosymmetric medium, the polarization produced by the electric field is, besides being aligned with it, identical in norm for every direction. Therefore, an electric field inversion within a centrosymmetric medium involves a strict polarization inversion. If we consider the general expression of the even-order polarization, we get:

$$\overrightarrow{P}^{(2n)} = \overleftrightarrow{\chi}^{(2n)} \cdot \overrightarrow{E}^{2n} \qquad n = 1, 2, 3, \cdots . \tag{1.21}$$

The figure 1.3 show the matter polarization in function of the electric field. Three configurations are depicted: linear activity in a centrosymmetric medium, nonlinear activity in a centrosymmetric medium, and finally nonlinear activity in a non centrosymmetric medium. In case of centrosymmetry, the amplitude of the polarization effect is equal for $|\vec{E}|$ or -$|\vec{E}|$, while its direction is inverted.

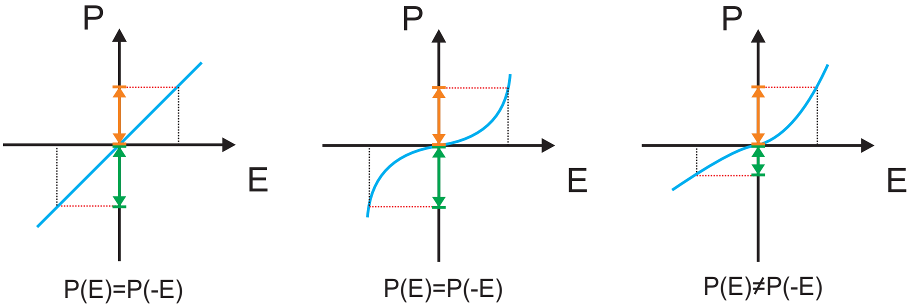

Figure 1.3: *Polarization in function of the electric field for a linear centrosymmetric medium (left), a nonlinear centrosymmetric medium (center), a nonlinear non centrosymmetric medium (right).*

We therefore get:

$$\begin{aligned} -\vec{P}^{(2n)} &= \overleftrightarrow{\chi}^{(2n)} \cdot (-\vec{E})^{2n} \\ &= \overleftrightarrow{\chi}^{(2n)} \cdot (\vec{E})^{2n} \cdot (-1)^{2n} \\ &= \vec{P}^{(2n)} \end{aligned} \tag{1.22}$$

We can thus write:

$$\begin{aligned} \overleftrightarrow{\chi}^{(2n)} \cdot (\vec{E})^{2n} &= -\overleftrightarrow{\chi}^{(2n)} \cdot (\vec{E})^{2n}, \\ \overleftrightarrow{\chi}^{(2n)} &= -\overleftrightarrow{\chi}^{(2n)}. \end{aligned} \tag{1.23}$$

Therefore, for all even-order nonlinear processes we get:

$$\Rightarrow \quad \overleftrightarrow{\chi}^{(2n)} = \overleftrightarrow{0}. \tag{1.24}$$

This observation that all even-order nonlinear effects can not exist in centrosymmetric media (that is to say: all amorphous materials plus eleven crystalline classes among the 32), is stated within the validity of the electric dipolar approximation. Note that this does not hold for incoherent processes such i.e. diffusion. Moreover, while the electric dipolar contribution to second-order nonlinear processes fully vanishes in centrosymmetric bulk surrounding, the electric quadrupolar and magnetic dipolar ones do not.

1.6.2 Surfaces and interfaces

A large majority of usual materials displays a bulk isotropy regarding their optical properties, excluding some crystalline classes and a few materials that could present a fortuitous anisotropic defect distribution. However, the specific case of interfaces represents a non centrosymmetric location relatively to the surface normal, allowing even-order nonlinear optical processes to be generated. Therefore, analysis methods based upon those optical mechanisms turn out to be well suited for interfacial system studies since they are intrinsically surface specific.

Besides this break of central symmetry along the surface normal, symmetry properties in the surface plan itself have to be considered. One commonly accepted hypothesis consists of assuming the studied interfacial film to be symmetric relatively to the azimuthal z axis, plus any mirror plane operation (the plane being perpendicular to the interface and including the z axis). Notice that the mirror plane operation is stronger than the rotation since any rotation may be decomposed in a sequence of two mirror plane operations, while some particular mirror plane operation may never be reproduced by rotation operation). While this particular condition has been established, the electrical susceptibility tensor has to remain unchanged by mirror plane symmetry operations. The expression of this electrical susceptibility after the symmetry operations is:

$$\chi^{(2)}_{lmn} = \sum_{ijk} \alpha_{li}\, \alpha_{mj}\, \alpha_{nk}\, \chi^{(2)}_{ijk} \tag{1.25}$$

with α, the mirror plane symmetry operator that acts over each subscript to apply the frame change from one basis to another. Those operators are 3x3 matrices as defined hereafter:

$$\alpha_{(x\,plane)} = \begin{pmatrix} -1 & 0 & 0 \\ 0 & 1 & 0 \\ 0 & 0 & 1 \end{pmatrix}, \tag{1.26}$$

$$\alpha_{(y\,plane)} = \begin{pmatrix} 1 & 0 & 0 \\ 0 & -1 & 0 \\ 0 & 0 & 1 \end{pmatrix}. \tag{1.27}$$

Lets first apply a x plane mirror operator to the susceptibility tensor, that is the $\alpha_{(x\,plane)}$ operation. In order to verify the in-plane symmetry invariance of χ, the following equality should hold:

$$\begin{aligned}\chi^{(2)}_{lmn} &= \sum_{ijk} id(-1)_{i=x}\ id(-1)_{j=x}\ id(-1)_{k=x}\ \chi_{ijk} \\ &= \chi^{(2)}_{ijk}\,.\end{aligned} \tag{1.28}$$

with $id(-1)_{i=x}$ the identity matrice, but amounting to -1 when i=x. The only way to satisfy it is to get an even value of x subscript, in our case, 0 or 2. The same approach with a plane normal to y leads to a even value of y subscript. At the end, the planar symmetry properties of the interface impose several (20) susceptibility tensor components to vanishe, namely:

$$\begin{aligned}&\chi^{(2)}_{yyy},\ \chi^{(2)}_{zzy},\ \chi^{(2)}_{zyz},\ \chi^{(2)}_{yzz},\ \chi^{(2)}_{xxy},\\ &\chi^{(2)}_{xyx},\ \chi^{(2)}_{yxx},\ \chi^{(2)}_{xxx},\ \chi^{(2)}_{zzx},\ \chi^{(2)}_{zxz},\\ &\chi^{(2)}_{xzz},\ \chi^{(2)}_{yyx},\ \chi^{(2)}_{yxy},\ \chi^{(2)}_{xyy},\ \chi^{(2)}_{xyz},\\ &\chi^{(2)}_{xzy},\ \chi^{(2)}_{yxz},\ \chi^{(2)}_{yzx},\ \chi^{(2)}_{zxy},\ \chi^{(2)}_{zyx}\,.\end{aligned} \tag{1.29}$$

The planar symmetry imposes the x axis not to be distinguishable from the y one. Consequently, among the seven remaining terms, we have the following equalities:

$$\begin{aligned}\chi^{(2)}_{yyz} &= \chi^{(2)}_{xxz}\\ \chi^{(2)}_{yzy} &= \chi^{(2)}_{xzx}\\ \chi^{(2)}_{zyy} &= \chi^{(2)}_{zxx}\\ \chi^{(2)}_{zzz}&\,.\end{aligned} \tag{1.30}$$

Consequently, when the surface isotropy is posed, any second-order nonlinear phenomenon outgoing from interfaces (such as the sum-frequency generation one), relies exclusively on four independent components of the susceptibility tensor. Moreover, if the two incident photons have the same frequency (SHG), both latter subscripts may be equally exchanged. Indeed, by convention, the first subscript matches the nonlinear generated photon (SFG, SHG, DFG...), the second is for the higher frequency incident photon and the last matches the remaining one. We therefore obtain:

$$\begin{aligned}&\chi^{(2)}_{xxz} = \chi^{(2)}_{xzx}\\&\chi^{(2)}_{zxx}\\&\chi^{(2)}_{zzz}\,.\end{aligned} \tag{1.31}$$

The second harmonic generation may thus be described by only three components of the second-order susceptibility [Dick et al., 1985] [Simpson and Rowlen, 2000].

Now that we have taken advantage of the intrinsic symmetry properties of the susceptibility tensor through interfacial considerations, it is important to notice that it becomes possible to obtain a single relation (or close to it) between the polarization and the second-order susceptibility elements as discussed previously in section 1.5 through equation 1.20. It is therefore possible, under some conditions, to quantify all the $\chi^{(2)}$ elements from the polarization response of the interface when probed by a second-order process. This question will be extensively discussed in chapter 2.

1.7 Intensity of nonlinear second-order processes

The intensity of nonlinear second-order processes depends firstly on both incident beam intensities, and secondly on the square modulus of the effective $\chi^{(2)}_{(eff)}$:

$$I_{(\omega_3)} \propto |\chi^{(2)}_{(eff)}|^2 \; I_{(\omega_1)} \; I_{(\omega_2)}\,. \tag{1.32}$$

The value of the effective $\chi_{(eff)}$ is related to the experimental geometry through the Fresnel coefficients (described in the section 1.8). Those latter quantify the electric field modifications undergone during any reflection and refraction. They allow to constitute a link between the physical macroscopic $\chi^{(2)}$ and the measured effective one [Hore et al., 2005, Sung et al., 2005]:

$$\chi^{(2)}_{IJK,(eff)} = [F_{II}\, e_I]_{(\omega_3)}\; \chi^{(2)}_{IJK} : [F_{JJ}\, e_J]_{(\omega_2)}[F_{KK}\, e_K]_{(\omega_1)}\,, \tag{1.33}$$

with $\overrightarrow{e}_{(\omega)}$, a unit polarization vector, and $\overleftrightarrow{F}_{(\omega)}$, the Fresnel factor tensor, both for an electric field of ω pulsation.

Consequently to the in plane isotropy, we see through equation 1.30 that the different non vanishing susceptibility components lead to only 4 polarization combinations (the other leading to a zero intensity process), namely:

$$I_{ppp}\ , \quad I_{ssp}\ , \quad I_{sps}\ , \quad I_{pss}\,. \tag{1.34}$$

For the SHG case, only three intensities should be considered:

$$\begin{aligned} I_{ppp} &= I_{pp} \\ I_{ssp} &= I_{sps} = I_{s:45^\circ} \\ I_{pss} &= I_{ps}\,. \end{aligned} \tag{1.35}$$

Those last equalities are valid for collinear incident beams, that is to say for two incident photons originating from the same and unique beam (the most common experimental set up in SHG). The necessity to polarize the incident beam at 45° is then fully justified since the reconstruction of the vectorial projection allows to obtain one s polarized photon, and one p polarized.

In order to quantify those intensities (a necessary step for further information retrieval), expressions of the Fresnel coefficients/factors based on experimental parameters are required. The following section is dedicated to this task.

1.8 Fresnel coefficients - Fresnel factors

1.8.1 Fresnel coefficients

Fresnel coefficients are dimensionless quantities that define the amplitudes of transmitted and reflected electromagnetic waves relatively to the interfacial incident one. In the following section, we will deduce their expressions in terms of incidence angle and refractive index only.

s polarization

The passing of a light beam (pulsation ω, s polarized) through an interface goes along with a refracted and a reflected component as shown in the figure 1.4. The associated mathematical expressions may easily be deduced from the scheme.

Namely, θ_1 and θ_2 are the incidence and refraction angles, $\overrightarrow{E'}$ and $\overrightarrow{B'}$ the refracted electric and magnetic fields, $\overrightarrow{E"}$ and $\overrightarrow{B"}$the reflected ones. Let us choose the s polarized incident electric field $\vec{E}$ as a vector outgoing from the sheet plane. The $\overrightarrow{E}$, $\overrightarrow{B}$, $\overrightarrow{K}$ trihedra being direct, the magnetic field is deduced directly from the propagation direction $\vec{K}$ (fig 1.4). From the interfacial continuity conditions of the field, we may readily obtained the following relationship (note: since the $\overrightarrow{E}$ field is s polarized, the $\overrightarrow{B}$ one is p polarized):

$$\begin{aligned} E &= -E'' + E' \quad \Rightarrow \quad E + E'' = E' \,, \\ -\frac{B}{\mu_1}\cos\theta_1 + \frac{B''}{\mu_1}\cos\theta_1 &= -\frac{B'}{\mu_2}\cos\theta_2 \,. \end{aligned} \tag{1.36}$$

With $\mu = \mu_0\,\mu_r$, and μ_1 being the μ_r for medium 1. From the Maxwell equation, and the definition of plane waves [Jackson, 2001]:

$$\begin{aligned} \overrightarrow{\nabla} \times \overrightarrow{E} &= -\frac{\partial \overrightarrow{B}}{\partial t} \,, \\ i\overrightarrow{k} \times \overrightarrow{E} &= i\omega \overrightarrow{B} \,, \\ \omega\overrightarrow{B} &= \overrightarrow{k} \times \overrightarrow{E} \,, \\ \omega|\overrightarrow{B}| &= |\overrightarrow{k}| \cdot |\overrightarrow{E}| \,, \\ |\overrightarrow{B}| &= \frac{n}{c}\,|\overrightarrow{E}| \,, \end{aligned} \tag{1.37}$$

we obtain:

$$\begin{aligned} E + E'' &= E' \,, \\ \frac{n_1}{\mu_1}(E - E'')\cos\theta_1 &= \frac{n_2}{\mu_2}E'\cos\theta_2 \,. \end{aligned} \tag{1.38}$$

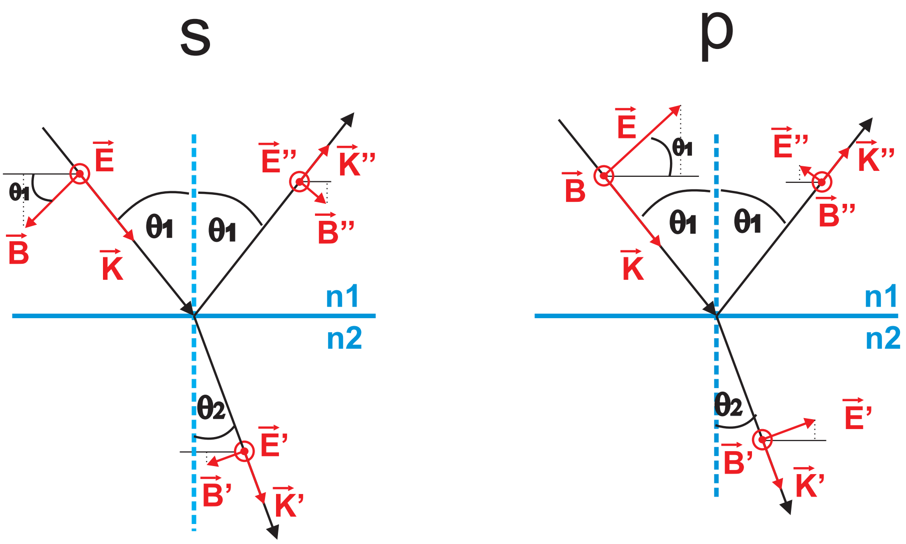

Figure 1.4: *Scheme of the reflected and refracted components at the interface.*

If we consider non magnetic materials, we have $\mu_1 = \mu_2 = 1$. By eliminating E" (respectively E') from the relation, we obtain the transmission (respectively, reflection) coefficient of the incident wave:

$$\begin{aligned} n_1\,(2E - E')\cos\theta_1 &= n_2\,E'\,\cos\theta_2\,, \\ \Rightarrow \quad 2\,n_1\,E\,\cos\theta_1 &= n_1\,E'\,\cos\theta_1 + n_2\,E'\,\cos\theta_2\,. \end{aligned} \tag{1.39}$$

The Fresnel transmission coefficient E'/E thus reads:

$$t^{\omega}_{s12} = \frac{2\,n^{\omega}_1\,\cos\theta^{\omega}_1}{n^{\omega}_1\,\cos\theta^{\omega}_1 + n^{\omega}_2\,\cos\theta^{\omega}_2}\,. \tag{1.40}$$

The reflection coefficient E"/E amounts to:

$$r^{\omega}_{s12} = \frac{n^{\omega}_1\,\cos\theta^{\omega}_1 - n^{\omega}_2\,\cos\theta^{\omega}_2}{n^{\omega}_1\,\cos\theta^{\omega}_1 + n^{\omega}_2\,\cos\theta^{\omega}_2}\,. \tag{1.41}$$

In order to rewrite those expression as a function of the incidence angle only, we may use the Snell's law expression to establish the following relations:

$$\begin{aligned} n_2 \sin\theta_2 &= n_1 \sin\theta_1 \,, \\ \sin\theta_2 &= \sin\theta_1 \frac{n_1}{n_2} \,, \end{aligned} \tag{1.42}$$

$$\cos\theta_2 = \sqrt{1 - \sin^2\theta_2} = \sqrt{1 - \sin^2\theta_1 \frac{n_1^2}{n_2^2}} = \sqrt{1 - \sin^2\theta_1 \frac{\epsilon_1}{\epsilon_2}} \,,$$

the Fresnel coefficients associated to the reflection and refraction processes are therefore:

$$r^{\omega}_{s12} = \frac{\cos\theta^{\omega}_1 - \sqrt{\frac{\epsilon^{\omega}_2}{\epsilon^{\omega}_1} - \sin^2\theta^{\omega}_1}}{\cos\theta^{\omega}_1 + \sqrt{\frac{\epsilon^{\omega}_2}{\epsilon^{\omega}_1} - \sin^2\theta^{\omega}_1}} \,, \tag{1.43}$$

$$t^{\omega}_{s12} = \frac{2\cos\theta^{\omega}_1}{\cos\theta^{\omega}_1 + \sqrt{\frac{\epsilon^{\omega}_2}{\epsilon^{\omega}_1} - \sin^2\theta^{\omega}_1}} \,. \tag{1.44}$$

Note that for the total internal refection (TIR) case, Snell's law implies that the square root argument becomes negative. If we consider a non absorbing medium of pure real index, this is solved by taking the minus sign out of the square root as an imaginary part.

$$r^{\omega}_{s12} = \frac{\cos\theta^{\omega}_1 - i\sqrt{\sin^2\theta^{\omega}_1 - \frac{\epsilon^{\omega}_2}{\epsilon^{\omega}_1}}}{\cos\theta^{\omega}_1 + i\sqrt{\sin^2\theta^{\omega}_1 - \frac{\epsilon^{\omega}_2}{\epsilon^{\omega}_1}}} \,. \tag{1.45}$$

It is interesting to note that in this TIR configuration, the modulus of the above expression is equal to unity, meaning that the incident intensity is fully reflected, as suggested by the Total Internal Reflection expression.

p polarization

As before, let us choose an arbitrary orientation for the p polarized electric field vector, while the associated magnetic field direction is deduced from the direct trihedra relation (as shown in figure 1.4). The continuity condition implies:

$$\begin{aligned} E\ \cos\theta_1 &= E'\ \cos\theta_2 + E''\ \cos\theta_1\,, \\ \frac{B}{\mu_1} + \frac{B''}{\mu_1} &= \frac{B'}{\mu_2}\,. \end{aligned} \tag{1.46}$$

[+4*mm*]

From the relation between the E and B amplitudes, for non magnetic materials, we obtain:

$$\begin{aligned} (E - E'')\ \cos\theta_1 &= E'\ \cos\theta_2\,, \\ E + E'' &= \frac{n_2}{n_1} E'\,. \end{aligned} \tag{1.47}$$

By eliminating E" (respectively E') from the expression, we get the transmission coefficient (respectively reflection) of the incoming light wave:

$$\begin{aligned} E'' &= \frac{n_2}{n_1} E' - E\,, \\ (2\,E - \frac{n_2}{n_1} E')\cos\theta_1 &= E'\ \cos\theta_2\,, \\ \Rightarrow\ 2\,E\ \cos\theta_1 &= E'\ \cos\theta_2 + \frac{n_2}{n_1} E'\ \cos\theta_1\,. \end{aligned} \tag{1.48}$$

The Fresnel coefficient for the E'/E transmission is thus:

$$t^{\omega}_{p12} = \frac{2\,n^{\omega}_1\ \cos\theta^{\omega}_1}{n^{\omega}_2\ \cos\theta^{\omega}_1 + n^{\omega}_1\ \cos\theta^{\omega}_2}\,. \tag{1.49}$$

The one for the reflection reads:

$$r^{\omega}_{p12} = \frac{n^{\omega}_2\ \cos\theta^{\omega}_1 - n^{\omega}_1\ \cos\theta^{\omega}_2}{n^{\omega}_2\ \cos\theta^{\omega}_1 + n^{\omega}_1\ \cos\theta^{\omega}_2}\,. \tag{1.50}$$

As for the s polarisation, the Fresnel coefficients may be rewritten only in function of θ_1^ω as follows:

$$r_{p12}^{\omega} = \frac{\frac{\epsilon_2^\omega}{\epsilon_1^\omega}\cos\theta_1^\omega - \sqrt{\frac{\epsilon_2^\omega}{\epsilon_1^\omega} - \sin^2\theta_1^\omega}}{\frac{\epsilon_2^\omega}{\epsilon_1^\omega}\cos\theta_1^\omega + \sqrt{\frac{\epsilon_2^\omega}{\epsilon_1^\omega} - \sin^2\theta_1^\omega}}, \tag{1.51}$$

$$t_{p12}^{\omega} = \frac{2\cos\theta_1^\omega\sqrt{\frac{\epsilon_2^\omega}{\epsilon_1^\omega}}}{\frac{\epsilon_2^\omega}{\epsilon_1^\omega}\cos\theta_1^\omega + \sqrt{\frac{\epsilon_2^\omega}{\epsilon_1^\omega} - \sin^2\theta_1^\omega}}. \tag{1.52}$$

The expression of the TIR coefficient is achieved, as before, by taking an imaginary part out of the square root:

$$r_{p12}^{\omega} = \frac{\frac{\epsilon_2^\omega}{\epsilon_1^\omega}\cos\theta_1^\omega - i\sqrt{\sin^2\theta_1^\omega - \frac{\epsilon_2^\omega}{\epsilon_1^\omega}}}{\frac{\epsilon_2^\omega}{\epsilon_1^\omega}\cos\theta_1^\omega + i\sqrt{\sin^2\theta_1^\omega - \frac{\epsilon_2^\omega}{\epsilon_1^\omega}}}. \tag{1.53}$$

The above comment about the intensity modulus of the s polarization holds also for the p one.

1.8.2 Fresnel factors

We define the Fresnel factors mentioned in the χ_{eff} expression (equation 1.33) as the total electric field amplitude at the interface [Simpson and Rowlen, 2000]. Those factors are of course expressed through the Fresnel coefficients and are equal to the sum of the incident E_0 and reflected E_r electric field contributions ($E_{tot} = E_0 + E_r$), normalized relatively to the incident electric field amplitude E_0. They are defined in the x, y, and z direction. The amplitude of the total field along those three axes are:

$$\begin{aligned} E_{(tot)x} &= F_{xx}\,E_0\,, \\ E_{(tot)y} &= F_{yy}\,E_0\,, \\ E_{(tot)z} &= F_{zz}\,E_0\,. \end{aligned} \tag{1.54}$$

As shown in figure 1.5, we have:

Polarization projection on y axis = s polarisation

Polarisation projection on x axis = p polarisation × $\cos\theta$

Polarisation projection on z axis = p polarisation × $\sin\theta$

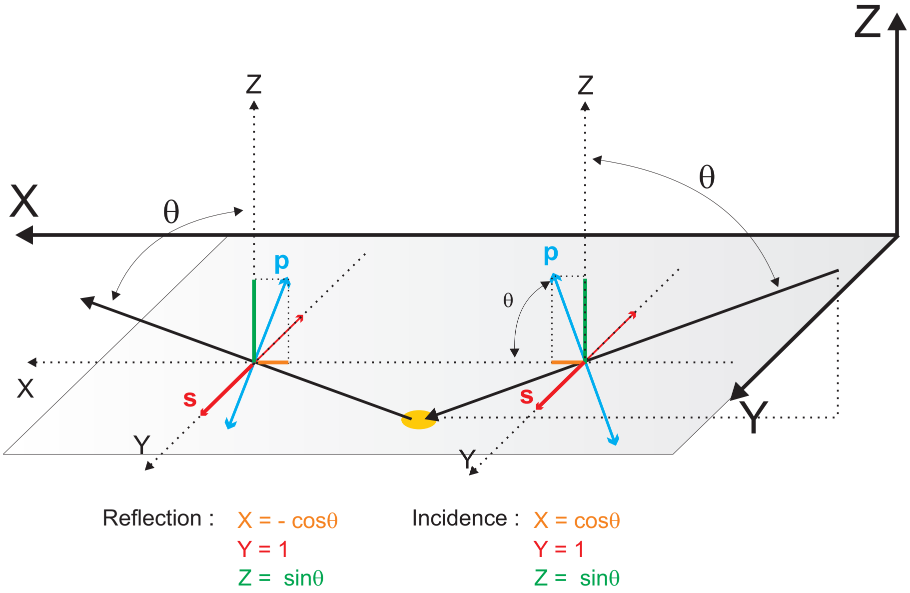

Figure 1.5: *Projection of incident and reflected polarizations on xyz axes.*

Based on the relation F = E_{tot}/E_i, we may express the diagonal terms of the Fresnel factor tensor. We will consider two experimental set up, first the reflection on a metallic surface, and second the TIR configuration.

Reflection on a Metallic Surface

$$F_{xx} = \frac{E_{0|p}\cos\theta - E_{r|p}\cos\theta}{E_{0|p}} = [1 - r^{\omega}_{p12}]\cos\theta,$$

$$F_{xx} = \frac{2\sqrt{\frac{\epsilon^{\omega}_2}{\epsilon^{\omega}_1} - \sin^2\theta^{\omega}_1}}{\frac{\epsilon^{\omega}_2}{\epsilon^{\omega}_1}\cos\theta^{\omega}_1 + \sqrt{\frac{\epsilon^{\omega}_2}{\epsilon^{\omega}_1} - \sin^2\theta^{\omega}_1}}\cos\theta, \tag{1.55}$$

$$F_{yy} = \frac{E_{0|s} + E_{r|s}}{E_{0|s}} = [1 + r^{\omega}_{s12}],$$

$$F_{yy} = \frac{2\cos\theta^{\omega}_1}{\cos\theta^{\omega}_1 + \sqrt{\frac{\epsilon^{\omega}_2}{\epsilon^{\omega}_1} - \sin^2\theta^{\omega}_1}}, \tag{1.56}$$

$$F_{zz} = \frac{E_{0|p}\sin\theta + E_{r|p}\sin\theta}{E_{0|p}} = [1 + r^{\omega}_{p12}]\sin\theta,$$

$$F_{zz} = \frac{2\frac{\epsilon^{\omega}_2}{\epsilon^{\omega}_1}\cos\theta^{\omega}_1}{\frac{\epsilon^{\omega}_2}{\epsilon^{\omega}_1}\cos\theta^{\omega}_1 + \sqrt{\frac{\epsilon^{\omega}_2}{\epsilon^{\omega}_1} - \sin^2\theta^{\omega}_1}}\sin\theta. \tag{1.57}$$

In order to provide a quantification of those Fresnel factors, the following table gives values for a visible beam (532 nm) incident on a platinum metallic surface with an incident angle of 55° with respect to the normal (as described in figure 1.5):

λ	532 nm	θ	55,0°
n	2,08	k	3,63
F_{xx}	0,488 - 0,455i	$e_x F_{xx}$ (p)	0,280 - 0,258i
F_{yy}	0,146 - 0,206i	$e_y F_{yy}$ (s)	0,146 - 0,206i
F_{zz}	$[1{,}512+0{,}450i]/\epsilon_{(layer)}$	$e_z F_{zz}$ (p)	$[1{,}238+0{,}368i]/\epsilon_{(layer)}$

Table 1.2: *Fresnel factors for a 532 nm beam incident on a platinum surface at an angle of 55° with respect to the normal.*

In order to see the angular dependence of the Fresnel factors, we plot their modulus for a 532 nm wavelength incident on a platinum surface:

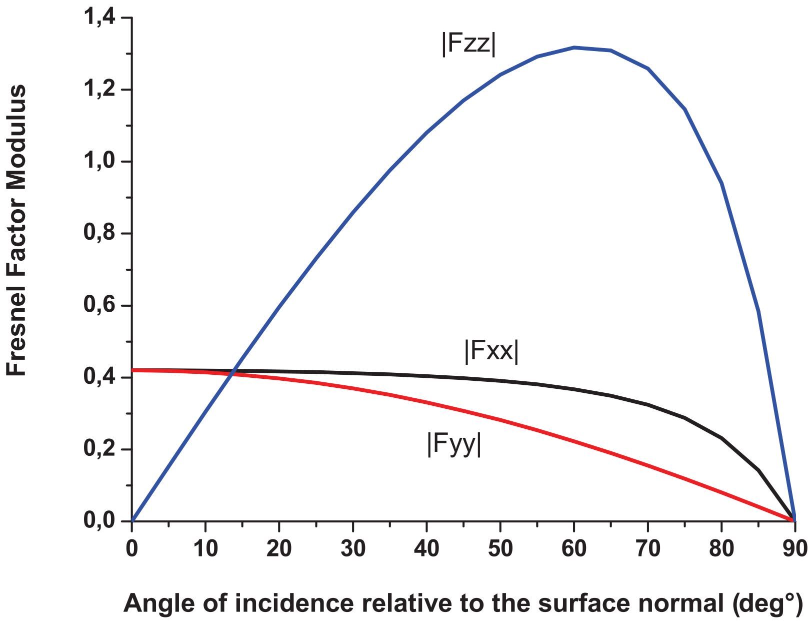

Figure 1.6: *Modulus of the Fresnel factors in function of the incidence angle. The wavelength is 532 nm, the surface is platinum.*

Total Internal Reflection (TIR)

In a total internal reflection configuration (it involves the light beam travelling from a higher refractive index medium towards a lower one) that typically happens when using a prism, we need to consider the entrance interface n_1/n_2 (air to prism), the TIR one n_2/n_3 (i.e. prism to air or water), and finally, the exit n_2/n_1 one (prism to air).

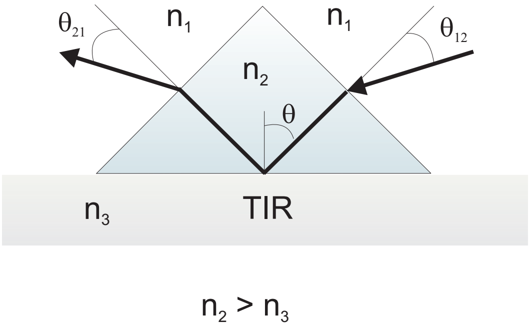

Figure 1.7: *Scheme of the total internal reflection process at a prism interface.*

The Fresnel factors at the TIR interface (typically, to calculate the total electric field resulting from a ω_i incident pulsation that will take part in the nonlinear process at the interface) are [Simpson et al., 2000]:

$$F_{yy}^{\omega_i} = t_{s12}^{\omega_i}[1 + r_{s23}^{\omega_i}], \tag{1.58}$$

$$F_{xx}^{\omega_i} = t_{p12}^{\omega_i}[1 - r_{p23}^{\omega_i}]\cos\theta^{\omega_i}, \tag{1.59}$$

$$F_{zz}^{\omega_i} = t_{p12}^{\omega_i}[1 + r_{p23}^{\omega_i}]\sin\theta^{\omega_i}. \tag{1.60}$$

since we have to consider the loss at the first interface to calculate the total electric field at the prism hypothenuse. The total field outside of the prism (typically, to calculate the intensity of the new generated nonlinear field with a ω_{nl} (nonlinear) after having taken into account the loss during the exit from the prism) is expressed as follows:

$$F_{yy}^{\omega_{nl}} = t_{s21}^{\omega_{nl}}\,[1 + r_{s23}^{\omega_{nl}}]\,, \tag{1.61}$$

$$F_{xx}^{\omega_{nl}} = t_{p21}^{\omega_{nl}}\,[1 - r_{p23}^{\omega_{nl}}]\,\cos\theta^{\omega_{nl}}\,, \tag{1.62}$$

$$F_{zz}^{\omega_{nl}} = t_{p21}^{\omega_{nl}}\,[1 + r_{p23}^{\omega_{nl}}]\,\sin\theta^{\omega_{nl}}\,. \tag{1.63}$$

1.8.3 Fresnel factors for a thin interfacial film

Spectroscopic analysis dedicated to study thin interfacial films or deposits, involves light beams that interact with a three layers system, typically air or water, the interfacial film of interest, and the substrate. Although the film is defined as "thin", its optical properties within a few nanometer thickness are far from being negligible as far as the interfacial reflection/refraction properties are concerned. In order to take them into account, we need to multiply the Fresnel factors along the z axis by $\varepsilon_1/\varepsilon_{film}$ (as suggested in table 1.2). Only the z component has to be modified from the interfacial continuity conditions of the field (conservation of the parallel components to the interface). In the case of biological deposition, the film may be assumed to be electrically insulating. Its dielectric constant is therefore a pure real number, usually assumed to be close to 1.4 (in the involved spectral region) [Wang et al., 2001] [Zhuang et al., 1999]. Knowing that air (medium 1) has a dielectric constant close to unity, the thin film may be estimated to modify the z Fresnel factor by a coefficient of around 0.7 in an air-solid configuration.

1.9 Resume

We have presented a approximate approach of the matter polarization by an electromagnetic wave. After having considered the validity of the electric dipole approximation, we have focused on the specific second-order optical processes. Symmetry considerations of the electrical susceptibility $\chi^{(2)}$ tensor determine the strength of those nonlinear mechanisms through their interface specific sensibility. We introduced the Fresnel coefficients to express the electric field at the interface, those latter being inferred from a simple optical scheme. Those factors have been expressed for different experimental configurations that will be used later in this manuscript. We now have the basic tools to go further into the comprehension and the running of second-order effects through spectroscopic studies.

1.10 Bibliography

[Corn and Higgins, 1994] Corn, R. M. and Higgins, D. A. (1994). Optical second harmonic generation as a probe of surface chemistry. Chem. Rev., 94:107–125.

[Dick et al., 1985] Dick, B., Gierulski, A., and Marowsky, G. (1985). Determination of the nonlinear optical susceptibility x(2) of surface-layers by sum and difference frequency generation in reflection and transmission. Applied Physics B-Photophysics and Laser Chemistry, 38:107–116.

[Guyot-Sionnest et al., 1986] Guyot-Sionnest, P., Chen, W., and Shen, Y. R. (1986). General considerations on optical second-harmonic generation from surfaces and interfaces. Physical Review B, 33(12):8254.

[Guyot-Sionnest and Shen, 1988] Guyot-Sionnest, P. and Shen, Y. R. (1988). Bulk contribution in surface 2nd-harmonic generation. Physical Review B, 38(12):7985–7989.

[Hore et al., 2005] Hore, D. K., Beaman, D. K., Parks, D. H., and Richmond, G. L. (2005). Whole-molecule approach for determining orientation at isotropic surfaces by nonlinear vibrational spectroscopy. Journal of Physical Chemistry B, 109(35):16846–16851.

[Jackson, 2001] Jackson, J. D. (2001). Classical Electrodynamics. Dunod.

[Lee et al., 2006] Lee, S. H., Wang, J., Krimm, S., and Chen, Z. (2006). Irreducible representation and projection operator application to understanding nonlinear optical phenomena: Hyper-raman, sum frequency generation, and four-wave mixing spectroscopy. Journal of Physical Chemistry A, 110(22):7035–7044.

[Shen, 1999] Shen, Y. R. (1999). Surface contribution versus bulk contribution in surface nonlinear optical spectroscopy. Applied Physics B-Lasers and Optics, 68(3):295–300.

[Simpson and Rowlen, 2000] Simpson, G. J. and Rowlen, K. L. (2000). Orientation-insensitive methodology for second harmonic generation. 1. theory. Analytical Chemistry, 72(15):3399–3406.

[Simpson et al., 2000] Simpson, G. J., Westerbuhr, S. G., and Rowlen, K. L. (2000). Molecular orientation and angular distribution probed by angle-resolved absorbance and second harmonic generation. Analytical Chemistry, 72(5):887–898.

[Sung et al., 2005] Sung, J. H., Park, K., and Kim, D. (2005). Surfaces of alcohol-water mixtures studied by sum-frequency generation vibrational spectroscopy. Journal of Physical Chemistry B, 109(39):18507–18514.

[Tepper et al., 1990] Tepper, P., Zink, J. C., Reif, J., and Matthias, E. (1990). Fresnel enhancement in 2nd-harmonic generation from rear surfaces of transparent media. Physical Review B, 42(15):9685–9688.

[Wang et al., 2001] Wang, J., Chen, C. Y., Buck, S. M., and Chen, Z. (2001). Molecular chemical structure on poly(methyl methacrylate) (pmma) surface studied by sum frequency generation (sfg) vibrational spectroscopy. J. Phys. Chem. B, 105(48):12118–12125.

[Zhu and Wong, 1992] Zhu, X. D. and Wong, A. (1992). Multipolar contributions to coherent optical 2nd-harmonic generation at an interface between 2 isotropic media - a quantum-electrodynamic calculation. Physical Review B, 46(4):2540–2544.

[Zhuang et al., 1999] Zhuang, X., Miranda, P. B., Kim, D., and Shen, Y. R. (1999). Mapping molecular orientation and conformation at interfaces by surface nonlinear optics. Phys. Rev. B, 59(19):12632–12640.

Chapter 2

Second-order nonlinear spectroscopies

2.1 Introduction

From their "central symmetry breaking" requirement, spectroscopies based on optical second-order effects reveal themselves to be exclusively surfaces and interfaces sensitive (since most of the material bulks are centosymmetric). Likewise, they are able to provide precious conformational and structural informations on a molecular system. The different kinds of non-linear effects correlated to a wide range of optical frequencies lead to the possibility to probe different surface properties such as the electronic or/and the vibrational ones. The Second Harmonic Generation (SHG) and Sum-Frequency Generation (SFG) processes turn out to be the most commonly used for such purposes in the second-order non-linear field. Although both of them rely on the χ^2 second-order electrical susceptibility, the SHG probes it through electronic transitions (visible-UV frequency), while the SFG requires at the same time electronic (visible) and vibrational (infrared) activities. In this chapter, we will attempt to distinguish those two spectroscopies. Starting from the general expression of the polarization, two distinct experimental procedures (one for the SFG, the other for the SHG) are adopted to extract molecular orientational informations (implying that the SHG is not processed as a particular case of the SFG). The most appropriate analysis procedures for these well distinct spectroscopies are determined and are compared with each other to underline their respective strength and weakness.

2.2 Expression of second-order polarizations

From the section 1.3, we may express the second-order nonlinear polarization as [Dick et al., 1985]:

$$\begin{pmatrix} P_x^{(2)} \\ P_y^{(2)} \\ P_z^{(2)} \end{pmatrix} \propto \begin{pmatrix} \chi_{xxx}^{(2)} & \chi_{xxy}^{(2)} & \chi_{xxz}^{(2)} & \chi_{xyx}^{(2)} & \chi_{xyy}^{(2)} & \chi_{xyz}^{(2)} & \chi_{xzx}^{(2)} & \chi_{xzy}^{(2)} & \chi_{xzz}^{(2)} \\ \chi_{yxx}^{(2)} & \chi_{yxy}^{(2)} & \chi_{yxz}^{(2)} & \chi_{yyx}^{(2)} & \chi_{yyy}^{(2)} & \chi_{yyz}^{(2)} & \chi_{yzx}^{(2)} & \chi_{yzy}^{(2)} & \chi_{yzz}^{(2)} \\ \chi_{zxx}^{(2)} & \chi_{zxy}^{(2)} & \chi_{zxz}^{(2)} & \chi_{zyx}^{(2)} & \chi_{zyy}^{(2)} & \chi_{zyz}^{(2)} & \chi_{zzx}^{(2)} & \chi_{zzy}^{(2)} & \chi_{zzz}^{(2)} \end{pmatrix} \begin{pmatrix} E_{2x}\, E_{1x} \\ E_{2x}\, E_{1y} \\ E_{2x}\, E_{1z} \\ E_{2y}\, E_{1x} \\ E_{2y}\, E_{1y} \\ E_{2y}\, E_{1z} \\ E_{2z}\, E_{1x} \\ E_{2z}\, E_{1y} \\ E_{2z}\, E_{1z} \end{pmatrix} \tag{2.1}$$

This leads when considering only the seven non vanishing coefficients from the azimuthal surface symmetry (colored in blue), to :

$$P_x^{(2)} = \chi_{xxz}^{(2)}\, E_{2x}\, E_{1z} + \chi_{xzx}^{(2)}\, E_{2z}\, E_{1x}\,, \tag{2.2}$$

$$P_y^{(2)} = \chi_{yyz}^{(2)}\, E_{2y}\, E_{1z} + \chi_{yzy}^{(2)}\, E_{2z}\, E_{1y}\,, \tag{2.3}$$

$$P_z^{(2)} = \chi_{zxx}^{(2)}\, E_{2x}\, E_{1x} + \chi_{zyy}^{(2)}\, E_{2y}\, E_{1y} + \chi_{zzz}^{(2)}\, E_{2z}\, E_{1z}\,. \tag{2.4}$$

From the Fresnel factors expressions in section 1.8.2, we get :

$$\begin{array}{lll} \left.\begin{array}{l} E_{ix} = F_{ixx}\, E_0 \\ E_{iz} = F_{izz}\, E_0 \end{array}\right\} & \text{for a p polarized beam}\,, \\ E_{iy} = F_{iyy}\, E_0 & \text{for a s polarized beam}\,. \end{array} \tag{2.5}$$

Those expressions are valid for incoming beams either s (y) or p (x and z) polarized. We may now provide more general relations for beams having an angle of polarization γ with respect to the plane of incidence ($\gamma = 0^\circ \rightarrow p \quad \gamma = 90^\circ \rightarrow s$), relations no longer expressed through the fields but rather through the beam intensities:

$$\begin{aligned} E_{ix} &\propto F_{ixx}\,\sqrt{I_0}\,\cos\gamma\,, \\ E_{iy} &\propto F_{iyy}\,\sqrt{I_0}\,\sin\gamma\,, \\ E_{iz} &\propto F_{izz}\,\sqrt{I_0}\,\cos\gamma\,. \end{aligned} \tag{2.6}$$

We will choose the subscript "i" as follow:

1 : incident lower frequency beam ,
2 : incident higher frequency beam ,
3 : second-order generated beam .

The different components of the polarization as a function of the angle γ may now be expressed as follows:

$$\begin{aligned} P^{(2)}_x \propto [\chi^{(2)}_{xxz}\,F_{1zz}\,F_{2xx}\,\cos\gamma_1\,\cos\gamma_2 \;+& \\ \chi^{(2)}_{xzx}\,F_{1xx}\,F_{2zz}\,\cos\gamma_1\,\cos\gamma_2]\,\sqrt{I_1 I_2}\,,& \end{aligned} \tag{2.7}$$

$$\begin{aligned} P^{(2)}_y \propto [\chi^{(2)}_{yyz}\,F_{1zz}\,F_{2yy}\,\cos\gamma_1\,\sin\gamma_2 \;+& \\ \chi^{(2)}_{yzy}\,F_{1yy}\,F_{2zz}\,\sin\gamma_1\,\cos\gamma_2]\,\sqrt{I_1 I_2}\,,& \end{aligned} \tag{2.8}$$

$$\begin{aligned} P^{(2)}_z \propto [\chi^{(2)}_{zxx}\,F_{1xx}\,F_{2xx}\,\cos\gamma_1\,\cos\gamma_2 \;+& \\ \chi^{(2)}_{zyy}\,F_{1yy}\,F_{2yy}\,\sin\gamma_1\,\sin\gamma_2 \;+& \\ \chi^{(2)}_{zzz}\,F_{1zz}\,F_{2zz}\,\cos\gamma_1\,\cos\gamma_2]\,\sqrt{I_1 I_2}\,.& \end{aligned} \tag{2.9}$$

2.3 Expression of second-order intensities

2.3.1 Sum-frequency generation

The second-order generated beam intensity either in s or p polarization is [Dick et al., 1985]:

$$\begin{aligned} I_s^{\omega_3}(\gamma) &\propto \left| F_{3yy} P_y^{(2)} \right|^2 \\ &\propto \left| \chi_{yyz}^{(2)} a_1 \cos\gamma_1 \sin\gamma_2 + \chi_{yzy}^{(2)} a_2 \sin\gamma_1 \cos\gamma_2 \right|^2 I_1 I_2 , \end{aligned} \tag{2.10}$$

$$\begin{aligned} I_p^{\omega_3}(\gamma) &\propto \left| F_{3xx} P_x^{(2)} + F_{3zz} P_z^{(2)} \right|^2 \\ &\propto \Big| \chi_{xxz}^{(2)} a_3 \cos\gamma_1 \cos\gamma_2 + \\ &\quad \chi_{xzx}^{(2)} a_4 \cos\gamma_1 \cos\gamma_2 + \chi_{zzz}^{(2)} a_7 \cos\gamma_1 \cos\gamma_2 + \\ &\quad \chi_{zxx}^{(2)} (a_5 \cos\gamma_1 \cos\gamma_2 + a_6 \sin\gamma_1 \sin\gamma_2) \Big|^2 I_1 I_2 , \end{aligned} \tag{2.11}$$

with $a_1 \rightarrow a_7$ coefficients based on Fresnel factors and defined as follows:

$$\begin{aligned} a_1 &= F_{3yy} F_{2yy} F_{1zz} = F_{yyz} \\ a_2 &= F_{3yy} F_{2zz} F_{1yy} = F_{yzy} \\ a_3 &= F_{3xx} F_{2xx} F_{1zz} = F_{xxz} \\ a_4 &= F_{3xx} F_{2zz} F_{1xx} = F_{xzx} \\ a_5 &= F_{3zz} F_{2xx} F_{1xx} = F_{zxx} \\ a_6 &= F_{3zz} F_{2yy} F_{1yy} = F_{zyy} \\ a_7 &= F_{3zz} F_{2zz} F_{1zz} = F_{zzz} , \end{aligned} \tag{2.12}$$

while adopting the same order convention as for the $\chi^{(2)}$ indices (that is: non linear photon, higher frequency photon, lower frequency photon).

We may now write from equation 2.10 and 2.11 (when keeping the same "x" and "y" notation) the intensities of the four non vanishing polarization combinations for such second-order process ($\gamma = 0^\circ$ (p) , $\gamma = 90^\circ$ (s)):

$$I^{\omega_3}_{ppp} \propto \left| \chi^{(2)}_{xxz}\, a_3 + \chi^{(2)}_{xzx}\, a_4 + \chi^{(2)}_{zxx}\, a_5 + \chi^{(2)}_{zzz}\, a_7 \right|^2 I_1 I_2 \,, \tag{2.13}$$

$$I^{\omega_3}_{ssp} \propto \left| \chi^{(2)}_{yyz}\, a_1 \right|^2 I_1 I_2 \,, \tag{2.14}$$

$$I^{\omega_3}_{sps} \propto \left| \chi^{(2)}_{xzx}\, a_2 \right|^2 I_1 I_2 \,, \tag{2.15}$$

$$I^{\omega_3}_{pss} \propto \left| \chi^{(2)}_{zxx}\, a_6 \right|^2 I_1 I_2 \,. \tag{2.16}$$

2.3.2 Second harmonic generation

Let us now rewrite those expressions for the particular case of second harmonic generation. We get the following experimental conditions:

$$SHG = \begin{cases} \text{colinear beams} \\ \gamma_1 = \gamma_2 = \gamma \\ \chi^{(2)}_{xxz} = \chi^{(2)}_{xzx} \\ F_{1xx} = F_{2xx} = F_{xx} \\ F_{1yy} = F_{2yy} = F_{yy} \\ F_{1zz} = F_{2zz} = F_{zz} \,. \end{cases} \tag{2.17}$$

The second-order generated beam intensity in s or p polarization now reads:

$$\begin{aligned} I^{2\omega}_s(\gamma) &\propto \left| \chi^{(2)}_{xxz}\, b_1\, 2\, \sin\gamma\, \cos\gamma \right|^2 (I^\omega)^2 \\ &\propto \left| \chi^{(2)}_{xxz}\, b_1\, \sin 2\gamma \right|^2 (I^\omega)^2 \,, \end{aligned} \tag{2.18}$$

$$\begin{aligned} I^{2\omega}_p(\gamma) \propto \Big| & \chi^{(2)}_{zxx}\, b_2\, \sin^2\gamma + \\ & (\chi^{(2)}_{xxz}\, b_3 + \chi^{(2)}_{zxx}\, b_4 + \chi^{(2)}_{zzz}\, b_5)\cos^2\gamma \Big|^2 (I^\omega)^2 \,. \end{aligned} \tag{2.19}$$

The only three allowed combinations based on p or s polarization are:

$$I_{pp}^{2\omega} \propto \left| \chi_{xxz}^{(2)} b_3 + \chi_{zxx}^{(2)} b_4 + \chi_{zzz} b_5 \right|^2 (I^{\omega})^2 , \tag{2.20}$$

$$I_{ps}^{2\omega} \propto \left| \chi_{zxx}^{(2)} b_2 \right|^2 (I^{\omega})^2 , \tag{2.21}$$

$$I_{s45}^{2\omega} \propto \left| \chi_{xxz}^{(2)} b_1 \right|^2 (I^{\omega})^2 , \tag{2.22}$$

with $b_1 \to b_5$ coefficients based on the Fresnel factors as before:

$$\begin{aligned} b_1 &= F_{3yy} F_{yy} F_{zz} = F_{yyz} \qquad & b_2 &= F_{3zz} F_{yy} F_{yy} = F_{zyy} \\ b_4 &= F_{3zz} F_{xx} F_{xx} = F_{zxx} \qquad & b_5 &= F_{3zz} F_{zz} F_{zz} = F_{zzz} \\ b_3 &= 2 F_{3xx} F_{xx} F_{zz} = F_{xxz} . \end{aligned} \tag{2.23}$$

2.4 Quantification of $\chi^{(2)}$ from spectroscopy

2.4.1 Second harmonic generation

To extract information from equations 2.18 and 2.19, let us illustrate the inner sine and cosine relations in absolute value:

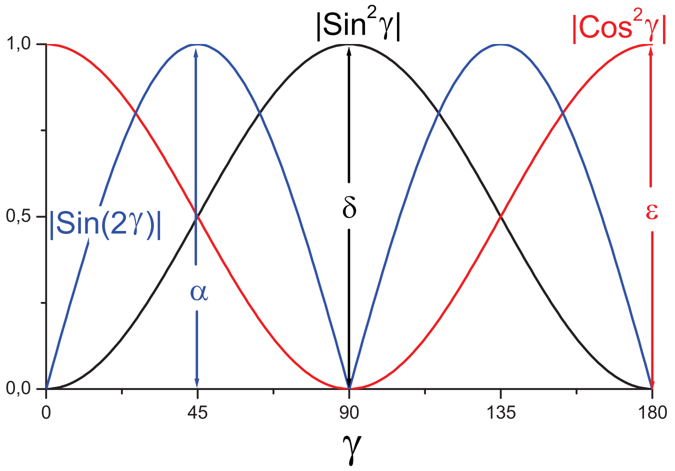

Figure 2.1: Representation of SHG intensity coefficients.

It is possible, for particular γ values, to isolate the $\chi^{(2)}_{xxz}$ and $\chi^{(2)}_{zxx}$, and thus to determined $\chi^{(2)}_{zzz}$ as well. Indeed, I_s depends on $(\sin 2\gamma)$, while I_{s45} represents the relative value of $\chi^{(2)}_{xxz}$ at 45° (intensity α in figure 2.1 from the sine unity). For I_p intensity, the s incident polarization leading to I_{ps} represents $\chi^{(2)}_{zxx}$ for the highest value of the sin^2 (δ on the figure). Finally, the p incident polarization leading to I_{pp} represents a combination of $\chi^{(2)}_{xxz}$, $\chi^{(2)}_{zxx}$, $\chi^{(2)}_{zzz}$ matching the maxima of the cos^2 (ϵ on the figure).

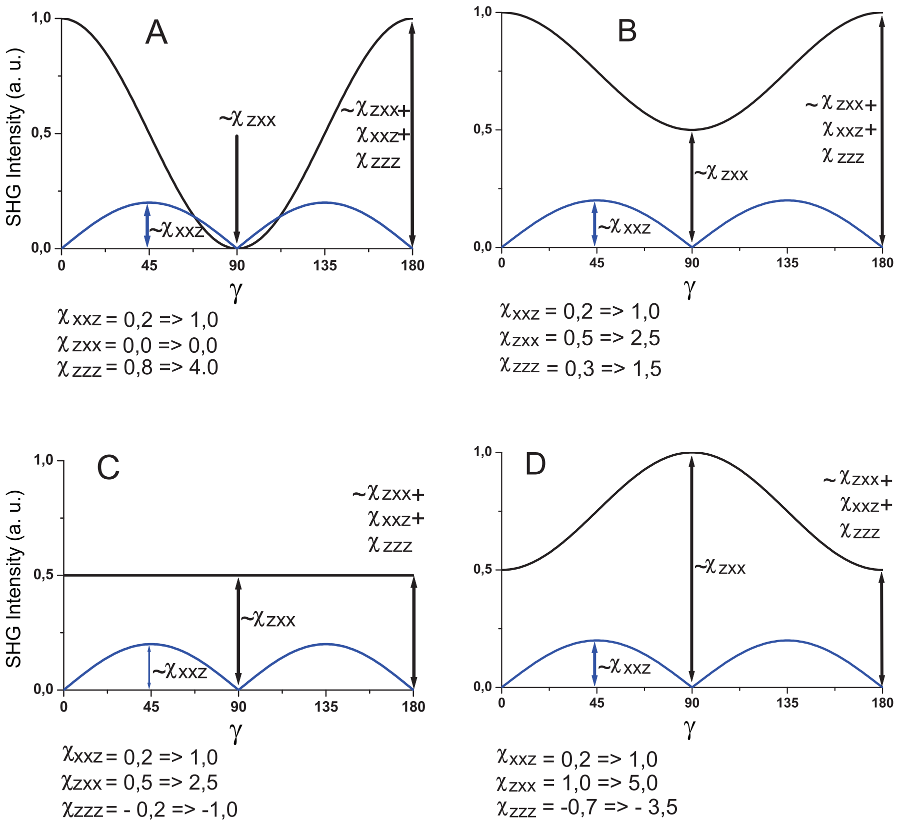

Figure 2.2: *Illustration of the different experimental SHG curves that may be obtained and the associated* $\chi^{(2)}$ *element values. The* I_s *intensity is the blue curve while the* I_p *is in black.*

From experimental measurements of the SHG intensity in both s and p polarizations while scanning the incident polarization from 0° to 180°, it is possible to extract relative values for the three elements $\chi^{(2)}_{zzx}$, $\chi^{(2)}_{xxz}$ and $\chi^{(2)}_{zzz}$. Different experimental curve trends are depicted in the figure 2.2 to show the representation of the different component values.

Notice that this is a rough quantification of the $\chi^{(2)}$ components that has been given since the Fresnel factors are set to unity. The goal is well to provide one idea of the $\chi^{(2)}$ component behavior relatively to the SHG curve modifications, but certainly not an accurate measurement.

However, it shows that, one single set of s and p polarization measurements carried out on a surface is enough to extract the second-order susceptibility value in SHG.

2.4.2 Sum-frequency generation

Through equation 2.13 - 2.16, it is possible to provide relative values for the 4 $\chi^{(2)}$ components from polarized spectroscopy (but only on insulating substrates since the 4 polarization combinations are required. This is thus not allowed on metallic surfaces). Note that this quantification is specific to a particular vibrational mode, and thus to a chemical group activity (selected by the IR wavelength).

2.5 Molecular orientation

Since the χ^2 tensor elements may be quantified from the polarization dependent nonlinear spectroscopy, we can obtain the averaged molecular orientation parameters. Those latter link the macroscopic second-order electrical susceptibility to the microscopic second-order polarisability β through [Hirose et al., 1992]:

$$\begin{aligned} \chi^{(2)}_{IJK} &= N_s \sum_{ijk} \langle R_{Ii} R_{Jj} R_{Kk} \rangle B_{ijk} \\ &= N_s \sum_{ijk} \langle T^{ijk}_{IJK}(\theta, \phi, \xi) \rangle B_{ijk} , \end{aligned} \tag{2.24}$$

where N_s is the surface molecular density and $\langle R_{Ii} R_{Jj} R_{Kk} \rangle$ is the ensemble average of the product of three direction cosines, R_{Xx}, between the laboratory and molecular coordinate systems. The product of direction cosines can be expressed as a function $T_{IJK}(\theta, \phi, \xi)$, where the molecular angles θ, ϕ and ξ are defined relatively to the laboratory frame as shown in figure 2.3.

The transformation from the molecular (ijk) to the laboratory (IJK) coordinate system is achieved by the use of the Euler rotation matrices through Euler angles (θ, ϕ, ξ). The switch of reference frames leads to the expression of the $\chi^{(2)}_{IJK}$ tensor components as a function of the β_{ijk} through Euler angles via equation 2.24. This mathematical relationship enables the calculation of the averaged molecular orientation on the surface.

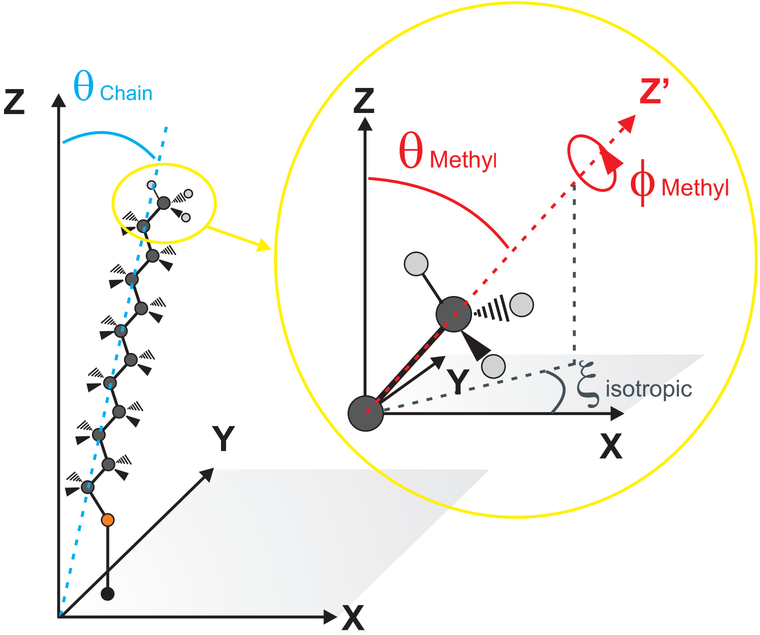

Figure 2.3: *Typical molecule (alkane chain) and the associated definition of the θ, ϕ and ξ angles relating the molecular coordinates to the laboratory surface ones. The azimuthal angle ξ is averaged by the surface symmetry.*

In the general case of a second-order process, only four components of $\chi^{(2)}_{IJK}$ remain. Those latter are expressed as a function of the three Euler angles along with the 27 second-order polarizability β_{ijk} components. The orientation determination seems thus to require a strict quantification of the β tensor. However, under certain conditions, it is possible to go around this restriction. Indeed, if on the one hand, a few dominant terms may be identified among the 27 β_{ijk} components, and on the other hand, some assumptions can be set on the orientational parameters, it becomes possible to define angular values without a strict quantification of the β tensor (a few component ratios are enough). The first and most regular assumption results from the azimuthal surface symmetry, for which the molecule are assumed to be randomly oriented around the surface normal (z axis). This latter has already been applied to the $\chi^{(2)}$ tensor so as only 4 components remain independent. T_{IJK} is thus integrated over ξ (0° to 2π), leading the orientational parameters to be resumed to θ and ϕ only. Then, a more restrictive simplification of T_{IJK} may be performed if an isotropy on the twist angle ϕ is as well assumed. This is valid only for specific cases (those which enable to retrieve the molecular orientation without a strict quantification of β_{ijk}!) and leaves θ as sole angular parameter.

Next, to solve this equation set, a few dominant β_{ijk} components have to be determined. Note that for the SFG case, 4 $\chi^{(2)}_{IJK}$ are known, while it is only three in SHG. However, because those are relative values, only three unknowns can be fixed from the SFG measurements and two from the SHG ones. Since one unknown is inevitably the angular parameter (only theta for this method), it results that the SFG can handle two β_{ijk} components at the most while it is a single one for the SHG. In the SFG case however, three components may be employed under certain conditions. Indeed, it is possible to express one unknown in function of the other, and to quantify this ratio between these two components from the Raman depolarization ratio of the molecule (investigated by [Dick, 1985], [Hore et al., 2005]).

Finally, this particular step of relying on defined dominant components, and the efficiency of the method, represent the practical difference between the SFG and the SHG spectroscopy. Indeed, while the second-order polarizability in SHG is based upon electronic transitions, strongly directional processes that easily lead to one or two dominant β_{ijk} components, the second-order polarizability involved in SFG results from both the Raman and infrared vibrational activities (demonstrated in the next chapter). Therefore, this last technique claims to be more complex, so that only very simple linear molecules adsorbed on surfaces and owning a clear symmetrical axis, enable the assumption of dominant hyperpolarisability tensor elements [Superfine et al., 1991]. As soon as the complexity of the molecule increases, the assumption over a single/double dominant term(s) becomes more and more incorrect [Hirose et al., 1993].

Consequently, the retrieval of the molecular orientation without a strict quantification of the β tensor is more specifically applied in the SHG case. For this latter, a single dominant β_{ijk} component is commonly assumed and gives good results for molecules having a net electronic transition axis. In the case of the SFG, this method is not so successful as for the SHG [Chin et al., 1992] [Galletto et al., 2003] [Gough, 1989] [Guyot-Sionnest et al., 1987] [Guyot-Sionnest et al., 1988] [Hatch et al., 1992] [Hirose et al., 1993].

2.6 Necessity to calculate the second-order polarizability

Historically, after the first communication on SFG spectroscopy in 1987 written by Zhu, X. D. and Shen, Y. R. [Zhu et al., 1987] [Superfine et al., 1988], a few papers dealing with SFG have processed the analysis in the same primary way as for the SHG case, that is through one single dominant β_{ijk} [Superfine et al., 1991]. A few years later (around 1992), Raman simulations leading to theoretical depolarization ratios allowed multi dominant terms to be used [Chin et al., 1992], as it is done for SHG studies. At this point, the sole difference between the two spectroscopies relies on the nature of the dipole moment transition allowing to measure the electronic dipole orientation within the molecule, or the vibrational dipole located in a particular chemical group. Only θ angle could be determined, and for SFG spectroscopy, only on insulating substrates, those latter enabling the whole set of polarization combinations to be used.

Since those conditions are very restrictive, the next step was to provide both Raman and infrared activities (either from *ab initio* or analytical methods), defining therefore wholly the β_{ijk} for a given vibrational mode within a given chemical group. Since the number of parameters was reduced, both the tilt and twist angles become accessible (notice that even now, the azimuthal isotropy is still assumed), and angular retrievement becomes even possible on non insulating substrates.

In this work, from the β_{ijk} calculated values, SFG experimental spectra may be simulated. The simulated intensity ratio between different vibrational mode may be modified through the adjustment of both the molecular tilt and twist angles. Practically, spectra are recorded for fixed incident polarization and the best fit to simulated data provides angular values. This SFG spectra simulation is widely explained in chapter 5. Besides, SHG measurements are performed as explained in the previous section, that is, by identifying a dominant component among the unknown β tensor.

2.7 Resume

The second-order polarization is written under its general expression, relying on Fresnel factors and angular considerations. The intensities of second-order processes are deduced, first as a function of the incident beam polarizations, and second for specific s and p incident polarizations (as it is done for SFG spectroscopy). Next, adjustments are made to this general expression in order to describe the SHG mechanism intensity. From all those expressions, methods to extract the value of the non vanishing $\chi^{(2)}_{IJK}$ elements are given for both SFG and SHG. This step is widely illustrated in order to provide a visual data processing capacity to the reader.

From those known values of χ, molecular orientation deductions can be performed. A description of one usual method to extract such structural informations from the measurements is provided, method based on the assumption of a single/double dominant β_{ijk} element(s). Finally, the validity of this method for SHG and SFG are discussed. It turns out that it is more appropriated for SHG and that a full determination of the hyperpolarizability components from theoretical computations is better suited to process the SFG data and retrieve orientational informations.

2.8 Bibliography

[Chin et al., 1992] Chin, R. P., Huang, J. Y., Shen, Y. R., Chuang, T. J., Seki, H., and Buck, M. (1992). Vibrational-spectra of hydrogen on diamond c(111)-(1x1). Physical Review B, 45(3):1522–1524.

[Dick, 1985] Dick, B. (1985). Irreducible tensor analysis of sum- and difference-frequency generation in partially oriented samples. Chem. Phys., 96:199–215.

[Dick et al., 1985] Dick, B., Gierulski, A., and Marowsky, G. (1985). Determination of the nonlinear optical susceptibility x(2) of surface-layers by sum and difference frequency generation in reflection and transmission. Applied Physics B-Photophysics and Laser Chemistry, 38:107–116.

[Galletto et al., 2003] Galletto, P., Unterhalt, H., and Rupprechter, G. (2003). The molecular orientation of co on pd(111): a polarization-dependent sfg study. Chemical Physics Letters, 367(5-6):785–790.

[Gough, 1989] Gough, K. M. (1989). Theoretical-analysis of molecular polarizabilities and polarizability derivatives in hydrocarbons. Journal of Chemical Physics, 91(4):2424–2432.

[Guyot-Sionnest et al., 1987] Guyot-Sionnest, P., Hunt, J. H., and Shen, Y. R. (1987). Sum-frequency vibrational spectroscopy of a langmuir film - study of molecular-orientation of a two-dimensional system. Physical Review Letters, 59(14):1597–1600.

[Guyot-Sionnest et al., 1988] Guyot-Sionnest, P., Superfine, R., Hunt, J. H., and Shen, Y. R. (1988). Vibrational spectroscopy of a silane monolayer at air solid and liquid solid interfaces using sum-frequency generation. Chemical Physics Letters, 144(1):1–5.

[Hatch et al., 1992] Hatch, S. R., Polizzotti, R. S., Dougal, S., and Rabinowitz, P. (1992). Surface vibrational spectroscopy of the vapor solid and liquid solid interface of acetonitrile on zro2. Chemical Physics Letters, 196(1-2):97–102.

[Hirose et al., 1992] Hirose, C., Akamatsu, N., and Domen, K. (1992). Formulas for the analysis of the surface sfg spectrum and transformation coefficients of cartesian sfg tensor components. Applied Spectroscopy, 46(6):1051–1072.

[Hirose et al., 1993] Hirose, C., Yamamoto, H., Akamatsu, N., and Domen, K. (1993). Orientation analysis by simulation of vibrational sum-frequency generation spectrum - ch stretching bands of the methyl-group. Journal of Physical Chemistry, 97(39):10064–10069.

[Hore et al., 2005] Hore, D. K., Beaman, D. K., Parks, D. H., and Richmond, G. L. (2005). Whole-molecule approach for determining orientation at isotropic surfaces by nonlinear vibrational spectroscopy. Journal of Physical Chemistry B, 109(35):16846–16851.

[Superfine et al., 1988] Superfine, R., Guyot-Sionnest, P., Hunt, J. H., Kao, C. T., and Shen, Y. R. (1988). Surface vibrational spectroscopy of molecular adsorbates on metals and semiconductors by infrared visible sum-frequency generation. Surface Science, 200(1):L445–L450.

[Superfine et al., 1991] Superfine, R., Huang, J. Y., and Shen, Y. R. (1991). Nonlinear optical studies of the pure liquid vapor interface - vibrational-spectra and polar ordering. Physical Review Letters, 66(8):1066–1069.

[Zhu et al., 1987] Zhu, X. D., Suhr, H., and Shen, Y. R. (1987). Surface vibrational spectroscopy by infrared-visible sum frequency generation. Physical Review B, 35(6):3047–3050.

Chapter 3

Theoretical considerations on the second-order polarizability

3.1 Introduction

In order to perform theoretical simulations and provide the nonlinear polarizability needed to retrieve orientation parameters from probed molecular films, the expression of β has to be described and quantified. This chapter is therefore dedicated to the understanding of the general expression of the polarizability β_{ijk} through quantum mechanical considerations. From this common theoretical background, striking links will be set up between the different kinds of nonlinear spectroscopy processes. It will allow to distinguish between the SHG and SFG processes but also to rank the processes as a function of their resonances, from the non resonant SHG to the doubly resonant DR-SFG, passing through the simply resonant SR-SFG.

3.2 Calculation of the second-order polarizability from the density matrix formalism

This section uses quantum mechanical tools to describe the origin of the second-order electrical polarizability. Since it is not the primary goal of this thesis to make a quantum description of such nonlinear process, we widely refer in the following sections to a Nonlinear Optics book [Boyd, 2003] and also to targeted publication [Lin et al., 1996]. This may help the reader to find basic elements or beginnings of theoretical procedures.

The calculation of the second-order nonlinear polarizability of a given quantum mechanical system can be performed from the system wave function $\Psi(\overrightarrow{r}, t)$ (expressed here in the $|\overrightarrow{r}\rangle$ representation). This latter is indeed sufficient to describe all the system physical properties and constitutes a solution to the time-dependent Schrödinger equation:

$$i\hbar \frac{\partial \Psi(\overrightarrow{r}, t)}{\partial t} = \widehat{H}\Psi(\overrightarrow{r}, t), \tag{3.1}$$

with $\widehat{H}$, the Hamiltonian operator.

Within the quantum mechanical formalism, any system, being either isolated or submitted to fixed external constraints, is fully described through its eigenstates. However, when a system shows an evolution based on fluctuating elements, statistical averages are strongly requested. The density matrix formalism is capable of treating effects such as collisional broadening of involved resonances resulting from optical processes (SFG, SHG...), effects that can not be described by the simple theoretical formalism based on the system wave function. The density matrix is therefore able to describe the statistical state of a quantum system.

In this formalism, the wave function of a system known to be in a particular state s is:

$$\Psi_s(\overrightarrow{r}, t) = \sum_n C_n^s(t)\, u_n(\overrightarrow{r}), \tag{3.2}$$

where $C_n^s(t)$ is an expansion coefficient which gives the probability amplitude that the system (in state s) is in energy eigenstate n at time t (with: $\sum_n |C_n^s(t)|^2 = 1$), while $u_n(\overrightarrow{r})$ is a function that gives the spatial distribution of the energy eigenstate n. Finally, the wave function of a particular system state is, within this formalism, a sum over all the possible energy eigenstates, each one of those being balanced by the the expansion coefficient.

From equation 3.1 and 3.2, we have:

$$i\hbar \sum_n \frac{d\,C_n^s(t)}{dt}\, u_n(\overrightarrow{r}) \;=\; \sum_n C_n^s(t)\, \hat{H}\, u_n(\overrightarrow{r})\,. \tag{3.3}$$

By multiplying each side of the equality by u_m^* and integrating over the whole space, one get:

$$i\hbar \frac{d\,C_m^s(t)}{dt} \;=\; \sum_n H_{mn}\, C_n^s(t)\,, \tag{3.4}$$

knowing that:

$$H_{mn} \;=\; \int u_m^*(\overrightarrow{r})\, \hat{H}\, u_n(\overrightarrow{r})\, d^3\overrightarrow{r}\,, \tag{3.5}$$

but also that $u_n(\overrightarrow{r})$ are orthonormal functions obeying therefore:

$$\int u_m^*(\overrightarrow{r})\, u_n(\overrightarrow{r})\, d^3\overrightarrow{r} \;=\; \delta_{mn}\,. \tag{3.6}$$

In order to define the density matrix elements, let us denote by p_s the probability to find the system in the quantum state $|\Psi_s\rangle$. The density operator which represents the whole collection of these states reads:

$$\widehat{\rho} \;=\; \sum_s p_s |\Psi_s\rangle\langle\Psi_s|\,. \tag{3.7}$$

The elements of the density matrix are thus defined by:

$$\begin{aligned} \rho_{nm} \;&=\; \langle u_n|\widehat{\rho}|u_m\rangle \\ &=\; \sum_s p_s \langle u_n|\Psi_s\rangle\langle\Psi_s|u_m\rangle\,. \end{aligned} \tag{3.8}$$

If equation 3.2 is rewritten just in term of the states:

$$|\Psi_s(t)\rangle \;=\; \sum_n C_n^s(t)\, |u_n^s\rangle\,, \tag{3.9}$$

the different elements of the density matrix are now expressed as:

$$\rho_{nm} = \sum_s p_s \, C_n^s(t) \, C_m^{s*}(t) \,. \tag{3.10}$$

Notice that the n and m indices are running over all the energy eigenstates of the system. The density matrix is thus a square matrix of dimension equal to the system eigenstates number. Its diagonal elements ρ_{nn} represent the probability to find the system in its energy eigenstate n (related therefore to the energy states population). The off-diagonal elements ρ_{nm} will be non zero if the system is in a coherent superposition of energy eigenstates n and m. Moreover, we will see that electric dipole moments that may be induced in the system are proportional to those density matrix off-diagonal elements.

In order to express the dipole moment of the system (able to oscillate at specific resonant frequencies), and thus the polarizability linked to this dipole moment through the electric field, let us introduce the definition of the expectation value for an observable quantity A within a system in quantum state s:

$$\langle A_s \rangle = \langle \Psi_s | \widehat{A} | \Psi_s \rangle \,. \tag{3.11}$$

Through the definition of the quantum state $|\Psi_s\rangle$ (equation 3.9), we get:

$$\langle A_s \rangle = \sum_{mn} C_m^{s*} \, C_n^s \, A_{s,mn} \,. \tag{3.12}$$

Beside this, the expected value of an observable quantity A when the exact state of the system is not known (which justifies the use of the density matrix formalism required for such situation with collisions or evolutionary interacting systems), is given by:

$$\begin{aligned} \langle A \rangle &= \sum_s p_s \langle A_s \rangle && (3.13) \\ &= \sum_s p_s \sum_{nm} C_m^{s*} \, C_n^s \, A_{s,mn} && (3.14) \\ &= \sum_{nm} \rho_{nm} \, A_{mn} \; [= \; tr(\widehat{\rho A})] \,. && (3.15) \end{aligned}$$

The observable dipole moment (from which the polarizability may be deduced) is thus expressed:

$$\langle \mu \rangle = \sum_{nm} \rho_{nm} \, \mu_{mn} \,. \tag{3.16}$$

Since the observable dipole moment is an expectation value that evolves in time, we have to determine how the density matrix itself evolves with time. We therefore have to go through the density matrix equation of motion:

$$\dot{\rho}_{nm} = \sum_s \frac{d\,p_s}{dt} C_n^s C_m^{s*} + \sum_s p_s \Big(C_m^{s*} \frac{d\,C_n^s}{dt} + \frac{d\,C_m^{s*}}{dt} C_n^s \Big) . \tag{3.17}$$

From equation 3.4, we have:

$$C_m^{s*} \frac{d\,C_n^s}{dt} = \frac{-i}{\hbar} C_m^{s*} \sum_q H_{nq} C_q^s , \tag{3.18}$$

$$C_n^s \frac{d\,C_m^{s*}}{dt} = \frac{i}{\hbar} C_n^s \sum_q H_{mq}^* C_q^{s*} = \frac{i}{\hbar} C_n^s \sum_q H_{qm} C_q^{s*} . \tag{3.19}$$

The density matrix equation of motion thus becomes (p_s is assumed time independent):

$$\dot{\rho}_{nm} = \sum_s p_s \frac{i}{\hbar} \sum_q \Big(C_n^s C_q^{s*} H_{qm} - C_m^{s*} C_q^s H_{nq} \Big) , \tag{3.20}$$

$$= \frac{i}{\hbar} \sum_q \Big(\rho_{nq} H_{qm} - H_{nq} \rho_{qm} \Big) , \tag{3.21}$$

which gives when the sommation over q is performed:

$$\dot{\rho}_{nm} = \frac{i}{\hbar} (\hat{\rho} \hat{H} - \hat{H} \hat{\rho})_{nm} = \frac{-i}{\hbar} [\, \hat{H} \, , \hat{\rho}]_{nm} . \tag{3.22}$$

The time evolution of the density matrix is described through its commutation with the Hamiltonian operator. However, though this latter allows to describe the evolution in time of a quantum system, certain interactions (such as those resulting from collisions, resonances broadening,...) cannot be adequatly explained by this operator. Such effects are considered by adding phenomenological damping terms into the equation 3.22:

$$\dot{\rho}_{nm} = \frac{-i}{\hbar} [\, \hat{H} \, , \hat{\rho}]_{nm} - \Gamma_{nm} (\rho_{nm} - \rho_{nm}^{eq}) , \tag{3.23}$$

with the damping term meaning that ρ_{nm} relaxes to its equilibrium state ρ_{nm}^{eq} at a decay rate Γ_{nm}. To solve this equation, a perturbation technique is employed, in which the Hamiltonian is split into two parts as:

$$\hat{H} = \hat{H}_0 + \hat{V}(t) , \tag{3.24}$$

$\hat{H}$ being written as the sum of an $\hat{H}_0$ field-free Hamiltonian and a $\hat{V}$(t) interaction Hamiltonian describing the interaction of the system with an electromagnetic field.
To solve the perturbed density matrix equation of motion, let us pose a solution of ρ_{nm} in a power series of a small perturbation λ:

$$\rho_{nm} \;=\; \rho^{(0)}_{nm} \,+\, \lambda\,\rho^{(1)}_{nm} \,+\, \lambda^2 \rho^{(2)}_{nm} \,\cdots\,, \tag{3.25}$$

where $\lambda \in [0{,}1]$ characterizes the strength of the perturbation. This solution should hold for any value of λ, involving each order of the equation 3.25 to satisfy individually the perturbed density matrix equation of motion. After injection of equation 3.25 into equation 3.23, we obtain that each perturbed order term is linked by a recurrence relation, the last two terms $\rho^{(1)}$ and $\rho^{(2)}$ being thus expressed if the first $\rho^{(0)}$ is known. From this general perturbation procedure, the density matrix elements may be quantified. The solution for the second-order of the perturbation reads:

$$\rho^{(2)}_{nm} \;=\; e^{-(i\omega_{nm}+\Gamma_{nm})t} \int_{-\infty}^{t} \frac{-i}{\hbar}[\,\hat{V}\,,\,\hat{\rho}^{(1)}]_{nm}\, e^{(i\omega_{nm}+\Gamma_{nm})t'}\,dt'\,, \tag{3.26}$$

which becomes after developments:

$$\begin{aligned}
\rho^{(2)}_{nm} \;=\; & \sum_{l}\sum_{pq} e^{-i(\omega_p+\omega_q)t} \\
\times & \left[\frac{\rho^{(0)}_{mm}-\rho^{(0)}_{ll}}{\hbar^2} \, \frac{[\,\mu_{nl}\,\cdot\,E(\omega_q)\,][\,\mu_{lm}\,\cdot\,E(\omega_p)\,]}{[(\omega_{nm}\,-\,\omega_p\,-\,\omega_q)-i\Gamma_{nm}\,][(\omega_{lm}\,-\,\omega_p)-i\Gamma_{lm}]} \right. \\
- & \left. \frac{\rho^{(0)}_{ll}-\rho^{(0)}_{nn}}{\hbar^2} \, \frac{[\,\mu_{nl}\,\cdot\,E(\omega_p)\,][\,\mu_{lm}\,\cdot\,E(\omega_q)\,]}{[(\omega_{nm}\,-\,\omega_p\,-\,\omega_q)-i\Gamma_{nm}\,][(\omega_{nl}\,-\,\omega_p)-i\Gamma_{nl}]} \right] \\
\equiv\; & \sum_{l}\sum_{pq} K_{nml}\, e^{-i(\omega_p+\omega_q)t}\,.
\end{aligned} \tag{3.27}$$

The dipole moment of the system is expressed as (equation 3.16):

$$\langle\mu\rangle \;=\; \sum_{nm} \rho_{nm}\,\mu_{mn}\,, \tag{3.28}$$

the time-frequency dependence being defined as:

$$\langle\mu\rangle \;=\; \sum_{r} \langle\mu(\omega_r)\rangle\, e^{-i\omega_r t}\,. \tag{3.29}$$

By making equal equations 3.28 and 3.29, we can isolate $\langle\mu(\omega_r)\rangle$ for a frequency ω_r. The dipole moment oscillating at a particular frequency $\omega_p + \omega_q$ is thus expressed (through equations 3.27, 3.28 and 3.29):

$$\begin{aligned}\langle\mu^{(2)}(\omega_p + \omega_q)\rangle &= \sum_{nml}\sum_{pq} K_{nml}\,\mu_{mn}\,, \\ &= \beta(\omega_p + \omega_q)\,E(\omega_p)\,E(\omega_q)\,, \end{aligned} \tag{3.30}$$

and is linked to the second-order polarizability through the electric fields.

In order to get a general expression, different mathematical operations such as permutation symmetries, indice replacements, and population of states simplifications have to be performed. Finally, the full expression of this second-order microscopic polarizability (at T° = 0K, the population is only in the ground state "0", l is thus fixe to 1 and $\rho_{00} = 1$) for general frequencies $\omega_1,\ \omega_2\ and\ \omega_3$ is:

$$\begin{aligned}&\beta_{ijk}(\omega_3;\omega_2,\omega_1) \\ &= \frac{1}{2\hbar^2}\sum_{nm}\left\{\frac{\mu^i_{0n}\,\mu^j_{nm}\,\mu^k_{m0}}{[(\omega_{n0}-\omega_1-\omega_2)-i\Gamma_{n0}][(\omega_{m0}-\omega_1)-i\Gamma_{m0}]}\right. \\ &\quad+\frac{\mu^i_{0n}\,\mu^k_{nm}\,\mu^j_{m0}}{[(\omega_{n0}-\omega_1-\omega_2)-i\Gamma_{n0}][(\omega_{m0}-\omega_2)-i\Gamma_{m0}]} \\ &\quad+\frac{\mu^k_{0n}\,\mu^i_{nm}\,\mu^j_{m0}}{[(\omega_{mn}-\omega_1-\omega_2)-i\Gamma_{mn}][(\omega_{n0}+\omega_1)+i\Gamma_{n0}]} \\ &\quad+\frac{\mu^j_{0n}\,\mu^i_{nm}\,\mu^k_{m0}}{[(\omega_{mn}-\omega_1-\omega_2)-i\Gamma_{mn}][(\omega_{n0}+\omega_2)+i\Gamma_{n0}]} \\ &\quad+\frac{\mu^j_{0n}\,\mu^i_{nm}\,\mu^k_{m0}}{[(\omega_{nm}+\omega_1+\omega_2)+i\Gamma_{nm}][(\omega_{m0}-\omega_1)-i\Gamma_{m0}]} \\ &\quad+\frac{\mu^k_{0n}\,\mu^i_{nm}\,\mu^j_{m0}}{[(\omega_{nm}+\omega_1+\omega_2)+i\Gamma_{nm}][(\omega_{m0}-\omega_2)-i\Gamma_{m0}]} \\ &\quad+\frac{\mu^k_{0n}\,\mu^j_{nm}\,\mu^i_{m0}}{[(\omega_{m0}+\omega_1+\omega_2)+i\Gamma_{m0}][(\omega_{n0}+\omega_1)+i\Gamma_{n0}]} \\ &\quad\left.+\frac{\mu^j_{0n}\,\mu^k_{nm}\,\mu^i_{m0}}{[(\omega_{m0}+\omega_1+\omega_2)+i\Gamma_{m0}][(\omega_{n0}+\omega_2)+i\Gamma_{n0}]}\right\}, \end{aligned} \tag{3.31}$$

The corresponding three-level system is shown in figure 3.1. μ^j_{nm} quantities are defined as follows:

$$\mu^j_{nm} = \langle\psi_n|\mu^j|\psi_m\rangle, \tag{3.32}$$

μ^j_{nm} representing the matrix element of the displacement operator μ^j along the molecular axis j (within the orthogonal Cartesian axis system ijk in which β_{ijk} is expressed) between the system states $|\psi_n\rangle$ and $|\psi_m\rangle$. From this general expression, we may review the different second-order mechanisms as well as the different resonant processes, all being quantified through the rank three $\beta^{(2)}$ - 27 component tensor.

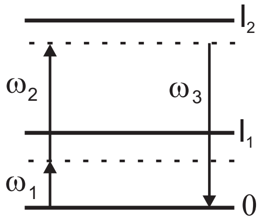

Figure 3.1: *Energy level diagram of a general second-order process.*

Based on figure 3.1, one can realize that there are actually four cases of SFG and SHG. The resonance/off-resonance (ω_1 matches the states l_1), the off-resonance /resonance (ω_3 matches the states l_2), the resonance/resonance (ω_1 and ω_3 match respectively the states l_1 and l_3), and finally the off-resonance/off-resonance (no match between frequencies and states).We will simply describe the two mechanisms involved in this thesis, namely, the SHG off-resonance/off-resonance and the resonance/off-resonance SR-SFG. The resonance/resonance DR-SFG case will not be developed, although all the necessary tools have been presented.

3.3 Resonance/off-resonance SR-SFG

The whole procedure has been extracted from the publication of [Lin et al., 1996]. The SFG spectroscopy usually relies on one infrared (ω_1) and one visible (ω_2) photon. The IR energy range matches vibrational transitions, while the UV-visible matches electronic transitions. In the resonance/off-resonance SR-SFG case, only the IR ω_1 photon is assumed to induce a vibrational resonance in the probed molecular system, while the visible/SFG frequency ω_2/ω_3 is expected to be far from any possible electronic transition. Thus, from the resonance of ω_1 with the 0m transition (see figure 3.2), only two terms of the second-order polarizability general expression (equation 3.31) are considered, namely those including (ω_{mo} - ω_1), while the six others (non resonant including ω_2 and $\omega_{_{SFG}}$) are no longer taken into account. Actually, this non resonant part contributes as a constant value over the scanned IR frequencies (and so the scanned SFG ones). The second-order nonlinear polarizability is thus written as:

$$\begin{aligned}
&\beta_{ijk}\left(\omega_{_{SFG}};\omega_{Vis},\omega_{IR}\right)\\
&=\frac{1}{2\hbar^2}\sum_{nm}\left\{\frac{\mu^i_{0n}\,\mu^j_{nm}\,\mu^k_{m0}}{\left[\left(\omega_{n0}-\omega_{SFG}\right)\right]\left[\left(\omega_{m0}-\omega_{IR}\right)-i\Gamma_{m0}\right]}\right.\\
&\quad+\left.\frac{\mu^j_{0n}\,\mu^i_{nm}\,\mu^k_{m0}}{\left[\left(\omega_{nm}+\omega_{SFG}\right)\right]\left[\left(\omega_{m0}-\omega_{IR}\right)-i\Gamma_{m0}\right]}\right\}.
\end{aligned}\tag{3.33}$$

Note that only the Γ_{m0} is still significant and thus considered. Furthermore, even if the non resonant part is ignored in this procedure, the non zero value of $\beta_{_{NR}}$ is taken into consideration elsewhere (into the macroscopic non resonant electrical susceptibility term, $\chi^{(2)}_{_{NR}} = |A_{_{NR}}|\, e^{i\phi}$).

The energy level diagram of this SR-SFG case is shown hereafter:

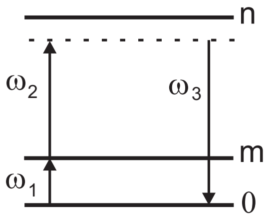

Figure 3.2: *Energy level diagram of resonance/off-resonance SFG.*

To go further, let us express the matrix element of the displacement operator $\widehat{\mu}$ in terms of molecular properties. This will be helpful to quantify the β_{ijk} factors. First we introduce the Born-Oppenheimer approximation to separate the vibrational and the electronic wavefunctions. The 0,l,m states become now respectively *gv*, *gv*', and *ku*. Here, *g* and *k* denote the electronic states, while *v*, *v*' and *u* represent the vibrational states (as shown in figure 3.3).

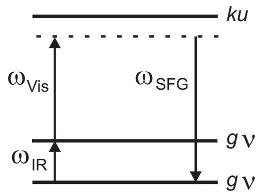

Figure 3.3: *Energy level diagram of resonance/off-resonance SFG in the B-O approximation.*

In the B-O approximation frame, equation 3.33 becomes:

$$\beta_{ijk}\left(\omega_{SFG};\omega_{Vis},\omega_{IR}\right) \tag{3.34}$$

$$= \frac{1}{2\hbar^2}\sum_{v,v',k,u}\frac{\mu^{k}_{gv',gv}}{[(\omega_{gv',gv}-\omega_{IR})-i\Gamma_{gv',gv}]}\times \tag{3.35}$$

$$\left\{\frac{\mu^{i}_{gv,ku}\,\mu^{j}_{ku,gv'}}{[(\omega_{ku,gv}-\omega_{SFG})]}+\frac{\mu^{j}_{gv,ku}\,\mu^{i}_{ku,gv'}}{[(\omega_{ku,gv'}+\omega_{SFG})]}\right\}.$$

Next, always in the B-O approximation, molecular wave functions as ψ_{gv} can be written as the product of an electronic wave function Φ_g (i.e. the electronic ground state *g*) and a vibrational wave function Θ_v (i.e. the vibrational *v* state of the electronic state *g*).

$$\psi_{gv} = \Phi_g(e)\,\Theta_v(Q)\,, \tag{3.36}$$

with e and Q the sets of electronic and vibrational coordinates, respectively. Thus, we get:

$$\begin{aligned}\mu^{i}_{gv,ku} &= \langle\psi_{gv}|\,\mu^{i}\,|\psi_{ku}\rangle = \langle\Phi_g\Theta_v|\,\mu^{i}\,|\Phi_k\Theta_u\rangle \\ &= \langle\Theta_v|\,\mu^{i}_{gk}\,|\Theta_u\rangle\,,\end{aligned} \tag{3.37}$$

where

$$\mu^{i}_{gk} = \langle\Phi_g(e)|\,\mu^{i}\,|\Phi_k(e)\rangle\,, \tag{3.38}$$

represents the electronic transition moment for the $g \leftrightarrow k$ transition. In order to evaluate the different elements of the dipole moment matrix, such as $\mu^i_{gv,ku}$, both integrations over the electronic and vibrational moments have to be carried out. The electronic integration is first performed through equation 3.38 to obtain the electronic transition moment $\mu^i_{g,k}$. This last term depending itself on vibrational coordinates, its vibrational integration is further realized in equation 3.37.

Before rewriting the expression of the β_{ijk} accounting for the separation of the electronic and vibrational degrees of freedom, let us introduce a second approximation, the one due to Placzek [Lin et al., 1996]. It tells that since the energy differences between electronic states are larger that the ones between vibrational states (UV-Vis energy is about 10 times higher than the IR one), one may write (k ≠ g):

$$\omega_{ku,gv} \simeq \omega_{kg} \simeq \omega_{ku,gv'} \, . \tag{3.39}$$

We may now rewrite equation 3.35 as follows:

$$\begin{aligned} &\beta_{ijk}\left(\omega_{SFG};\omega_{Vis},\omega_{IR}\right) \\ &= \frac{1}{2\hbar^2}\sum_{v,v',k,u}\frac{\langle\Theta_{v'}|\,\mu^k_{gg}\,|\Theta_v\rangle}{[(\omega_{gv',gv}-\omega_{IR})-i\Gamma_{gv',gv}]}\times \\ &\qquad\left\{\frac{\langle\Theta_v|\,\mu^i_{gk}\,|\Theta_u\rangle\,\langle\Theta_u|\,\mu^j_{kg}\,|\Theta_{v'}\rangle}{[(\omega_{kg}-\omega_{SFG})]}+\right. \\ &\qquad\qquad\left.\frac{\langle\Theta_v|\,\mu^j_{gk}\,|\Theta_u\rangle\,\langle\Theta_u|\,\mu^i_{kg}\,|\Theta_{v'}\rangle}{[(\omega_{kg}+\omega_{SFG})]}\right\}, \end{aligned} \tag{3.40}$$

with the closure relation $\sum_u |\Theta_u\rangle\,\langle\Theta_u| = 1$, we get:

$$\begin{aligned} &\beta_{ijk}\left(\omega_{SFG};\omega_{Vis},\omega_{IR}\right) \\ &= \frac{1}{2\hbar^2}\sum_{v,v'}\frac{\langle\Theta_{v'}|\,\mu^k_{gg}\,|\Theta_v\rangle}{[(\omega_{gv',gv}-\omega_{IR})-i\Gamma_{gv',gv}]}\,\langle\Theta_v|\,\alpha^{ij}_{gg}\,|\Theta_{v'}\rangle\,, \end{aligned} \tag{3.41}$$

with:

$$\alpha^{ij}_{gg} = \sum_k\left\{\frac{\mu^i_{gk}\mu^j_{kg}}{(\omega_{kg}-\omega_{SFG})}+\frac{\mu^j_{gk}\mu^i_{kg}}{(\omega_{kg}+\omega_{SFG})}\right\}, \tag{3.42}$$

where α^{ij}_{gg} is one component of the electronic polarizability and μ^k_{gg} of the dipole moment, both at the electronic ground state. Since they depend on vibrational coordinates, they can be expanded into power series with respect to the vibrational mode coordinate Q_q evaluated at the equilibrium (0 subscript):

$$\mu^k_{gg} = \mu^k_{gg_0} + \sum_q \left(\frac{\partial \mu^k_{gg}}{\partial Q_q}\right)_0 Q_q + \ldots , \tag{3.43}$$

$$\alpha^{ij}_{gg} = \alpha^{ij}_{gg_0} + \sum_q \left(\frac{\partial \alpha^{ij}_{gg}}{\partial Q_q}\right)_0 Q_q + \ldots . \tag{3.44}$$

Restricting 3.43 and 3.44 to the first order in Q, the final expression of the second-order polarizability as a function of the polarizability α^{ij} (Raman activity) and the dipole moment μ^k (IR activity) reads:

$$\begin{aligned}&\beta_{ijk}(\omega_{SFG}; \omega_{Vis}, \omega_{IR}) \\ &= \frac{1}{2\hbar^2} \sum_{v,v',q} \frac{|\langle \Theta_{v'}|\, Q_q\, |\Theta_v\rangle|^2}{[(\omega_{gv',gv} - \omega_{IR}) - i\Gamma_{gv',gv}]} \left(\frac{\partial \mu^k_{gg}}{\partial Q_q}\right)_0 \left(\frac{\partial \alpha^{ij}_{gg}}{\partial Q_q}\right)_0 ,\end{aligned} \tag{3.45}$$

where the transition moment of the vibrational mode coordinates between two vibrational states (the square modulus inner expression) is worth the harmonic oscillator energy $(\hbar/2\omega_q)^{(1/2)}$. Moreover, among all possible values of v and v', the only allowed ones are when the transition occurs between two adjacent vibrational states of the same vibrational mode, respecting $|\Delta v| = (0)$ and 1, from the IR selection rules. The $\omega_{gv',gv}$ is thus resume to ω_q. Finally, both terms $\langle \Theta_{v'}|\, \mu^k_{gg_0}\, |\Theta_v\rangle$ and $\langle \Theta_{v'}|\, \alpha^{ij}_{gg_0}\, |\Theta_v\rangle$ (not written) are a constant non resonant terms at equilibrium.

The second-order polarizability expression for the IR SR-SFG is then:

$$\beta_{ijk}(\omega_{SFG}; \omega_{Vis}, \omega_{IR}) = \frac{1}{4\hbar\omega_q} \sum_q \frac{(\frac{\partial \mu^k}{\partial Q_q})_0 (\frac{\partial \alpha^{ij}}{\partial Q_q})_0}{\omega_q - \omega_{IR} - i\Gamma_q} . \tag{3.46}$$

This expression underlines the necessity of both IR and Raman activities in the SFG process. Besides, the best ways to simulate SFG spectra and to retrieve orientational informations from those theoretical expressions have been studied in a recent work performed in our institution [Guthmuller et al., 2009].

3.4 off-resonance/off-resonance SHG

In this thesis, SHG experiments have been performed with ω_1=ω_2, and ω_3 included in the "visible" range (around 780 nm / 390 nm). Since the experiments have been carried out at fixed frequency (only the polarizations of the beams are tuned to extract molecular information, while the frequency is always kept fixed), the involved wavelengths and probed systems may be such that no resonance is induced. Therefore, there is no resonance at all among the 8 terms of equation 3.31, all of them being considered even if they are constant. It provides invariable β_{ijk} components value over the used frequencies (that are kept fixed here but may be scanned far from any resonance in a general concept). The corresponding energy level diagram is shown in figure 3.4.

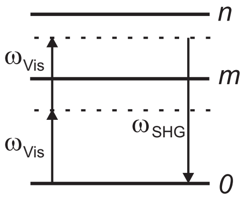

Figure 3.4: *Energy level diagram of off-resonance/off-resonance SHG.*

Since we have the following equality:

$$
\begin{aligned}
&\frac{1}{(\omega_{mn}-\omega_{SHG})(\omega_{n0}+\omega_{Vis})}+\frac{1}{(-\omega_{mn}+\omega_{SHG})(\omega_{m0}-\omega_{Vis})}\\
&=\frac{1}{(\omega_{mn}-\omega_{SHG})}\left[\frac{1}{\omega_{n0}+\omega_{Vis}}-\frac{1}{\omega_{m0}-\omega_{Vis}}\right]\\
&=\frac{1}{(\omega_{mn}-\omega_{SHG})}\left[\frac{\omega_{m0}-\omega_{Vis}-\omega_{n0}-\omega_{Vis}}{(\omega_{n0}+\omega_{Vis})(\omega_{m0}-\omega_{Vis})}\right]\\
&=\frac{1}{(\omega_{mn}-\omega_{SHG})}\left[\frac{\omega_{mn}-\omega_{SHG}}{(\omega_{n0}+\omega_{Vis})(\omega_{m0}-\omega_{Vis})}\right]\\
&=\frac{1}{(\omega_{n0}+\omega_{Vis})(\omega_{m0}-\omega_{Vis})},
\end{aligned}
\tag{3.47}
$$

and because all the damping terms from the equation 3.31 are removed, the expression of the β_{ijk} can thus be rewritten as follows:

$$\begin{aligned}
&\beta_{ijk}\left(\omega_{SHG};\omega_{Vis},\omega_{Vis}\right) \\
&= \frac{1}{2\hbar^2}\sum_{nm}\left\{\frac{(\mu^i_{0n}\,\mu^j_{nm}\,\mu^k_{m0}) + (\mu^i_{0n}\,\mu^k_{nm}\,\mu^j_{m0})}{[(\omega_{n0}-\omega_{SHG})][(\omega_{m0}-\omega_{Vis})]}\right. \\
&\quad + \frac{(\mu^j_{0n}\,\mu^i_{nm}\,\mu^k_{m0}) + (\mu^k_{0n}\,\mu^i_{nm}\,\mu^j_{m0})}{[(\omega_{n0}+\omega_{Vis})][(\omega_{m0}-\omega_{Vis})]} \\
&\quad \left. + \frac{(\mu^k_{0n}\,\mu^j_{nm}\,\mu^i_{m0}) + (\mu^j_{0n}\,\mu^k_{nm}\,\mu^i_{m0})}{[(\omega_{m0}+\omega_{SHG})][(\omega_{n0}+\omega_{Vis})]}\right\},
\end{aligned} \tag{3.48}$$

with μ^i_{0n} representing the matrix element of the displacement operator μ^i along the ith molecular axis between electronic states ψ_0 and ψ_n. There is a wide pannel of means for evaluating those elements, with a broad degree of relevance. For isolated chromophores or dyes, sum-over-states (SOS) approaches can be used to determine the involved wave functions and energies [Botek and Champagne, 2002]. As a matter of course, there are more terms involved in the mathematical expression of β_{ijk} in comparison with any resonant process (since those non-resonant terms are neglected in presence of resonant ones).

3.5 Resume

The general expression of the β_{ijk} has been deduced from the quantum mechanical density matrix formalism. Next, it has been developed for singly resonant SFG and off-resonant SHG. Through those theoretical expressions, one can understand why the resonant SFG process needs both the Raman and the IR activities to be active, while the SHG required only electronic transition moments.

3.6 Bibliography

[Botek and Champagne, 2002] Botek, E. and Champagne, B. (2002). Quantum-chemistry simulations of second-harmonic and sum-frequency generation of organic layers. Applied Physics B-Lasers and Optics, 74(7-8):627–634.

[Boyd, 2003] Boyd, R. W. (2003). Nonlinear optics, second edition. Academic Press, page Chapter 3.

[Guthmuller et al., 2009] Guthmuller, J., Cecchet, F., Lis, D., Caudano, Y., Mani, A. A., Thiry, A. P., Peremans, A., and Champagne, B. (2009). Theoretical simulation of vibrational sum-frequency generation spectra from density functional theory: Application to p-nitrothiophenol and 2,4-dinitroaniline. ChemPhysChem, 10:1–13.

[Lin et al., 1996] Lin, S. H., Hayashi, M., Islampour, R., Yu, J., Yang, D. Y., and Wu, G. Y. C. (1996). Molecular theory of second-order sum-frequency generation. Physica B, 222(1-3):191–208.

Chapter 4

Second harmonic generation spectroscopy

4.1 Introduction

The second harmonic generation (SHG) mechanism is the very first second-order process experimentally brought to bear [Franken et al., 1961]. It is indeed the simplest one since only a unique laser beam is required to generate frequency doubled photons from a nonlinear material. For fifty years, techniques, experimental set up and studied systems have been improved drastically through state-of-the-art spectroscopic researches. Nowadays, such powerful technique has been widely extended, for example to biological applications where it is used to obtain living-cell membrane imaging.

In this chapter, we will take advantage of the molecular orientation retrievement capability of the SHG spectroscopy through concepts established in chapter 1, 2, and 3. This capacity will allow us to follow the evolution of the molecular disposition taking place at a liquid-solid interface while under a stress initiated by a liquid flow. This common phenomenon of a free liquid running on solid surfaces is indeed complex and, even now, questions are still open about the fact that liquids may or may not slip on surfaces. After a brief review on what has already been done on this topic, we will attempt to provide answers from the interfacial liquid-molecule interaction probed by SHG. The experimental set up is described, and the results are discussed.

This work on SHG spectroscopy has been carried out in the Materials Research Laboratory (MRL) of the University of Illinois at Urbana-Champaign (UIUC), USA. This is the result of a six month project realized in the laboratory of Professor Steve Granick [Granick-Group, 2007].

4.2 Solid-liquid interfaces: hystory of a slippery question

The question if whether or not a fluid slips on solid surfaces has been raised since the 19th century. The fluid mechanics states the "no slip condition" as a basic hypothesis, imposing a dynamic equilibrium between the fluid and the surface through a null speed of the liquid immediately adjacent to the solid surface [Massey, 1989]. This assumption involves a liquid speed gradient normal to the surface and agrees well with the mean flow condition far from boundaries. It has almost never been caught out all along the last century, during which hydrodynamics gave rise to many experimental data agreeing well with theoretical models based on this postulate. As a proof, consider this citation from a fluid mechanics text book published only two decades ago [Massey, 1989]:

"In other words there is no relative motion between the fluid and the solid. This fact may seem surprising but it is undoubtedly true. No matter how smooth the solid surface or how small the viscosity of the fluid, the particles immediately adjacent to the surface do not move relative to it. It is perhaps not without interest that Newton’s term for viscosity was «defectus lubricitatis» - «lack of slipperiness». Even for a fluid that does not «wet» the surface, this rule is not violated."

This simple assumption allows to explain a lot of every day life observations, such as the fact that a simple clear water rinse of soapy dishes or even hands, allows only removing the superficial part of the soap lather, or the fact that, blowing on a surface to remove dusts only lets disappear the largest dust particles, but never the tiniest ones very close to the solid surface (as shown in figure 4.1) [Granick et al., 2003]. But does this assumption still holds on a micrometric scale... or even on a nanometric one? What about on a single fluid molecular layer scale?

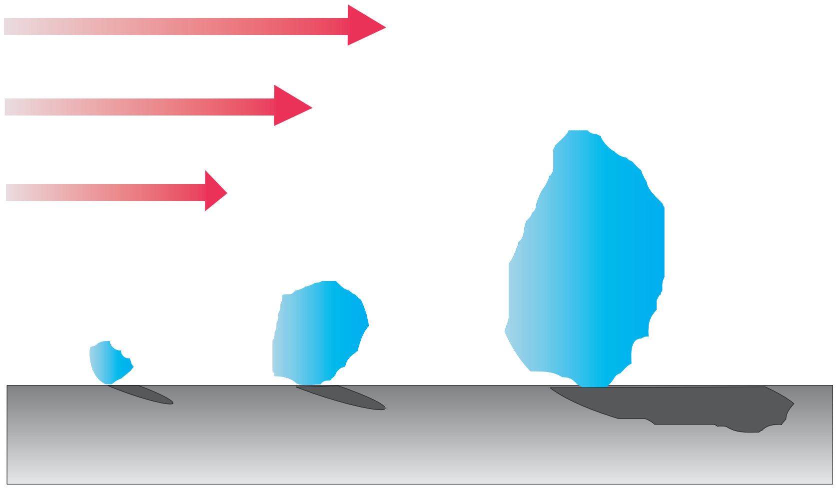

Figure 4.1: *The no slip condition schematized through a current every day live observation: blowing on a dusty surface only removes the largest particles, but never the tiniest ones because of the air speed gradient.*

In the last two decades, doubts have been emitted in different specialized research fields such as high molecular mass and high shear rate fluids (melted polymers) [Migler et al., 1993], and kinetic friction of a 10 molecules thick liquid film [Reiter et al., 1994]. Different theoretical and experimental studies have been realized in order to explain and to quantify such phenomena. These works inevitably go toward miniaturized systems for which the liquid volume to surface ratio increases, and therefore leads to an easier detection of any slippery effect.

Works based on the liquid pressure-flow relation within nanochannels [Giordano and Cheng, 2001], confined fluid force apparatus measurements [Zhu and Granick, 2001], and the most recent technique, the fluorescent particle image velocimetry [Jin et al., 2004] [Pit et al., 2000], show all that a slip of the liquid occurs, and that it is related to the mean fluid velocity. Moreover, different considerations about the liquid wetting properties [Schmatko et al., 2005] as well as the surface wetting and mechanical properties [Barrat and Bocquet, 1999] [Joseph et al., 2006] have been reported to play important roles. What is the next step?

4.3 SHG spectroscopy to specifically probe liquid-solid interfaces

The key point of this quest to understand and define the slipperiness of liquids on solid surfaces is the dimension of the probed liquid film. However, there are two ways to proceed. First, working with condensed fluid films presenting the smallest amount of molecular layers (mainly with friction force apparatus) and measure physical properties of the solid-liquid interaction. Second, working with a half space of free-liquid where the goal is to characterize the liquid speed gradient from the border to the channel center. In this second method, the challenge consists of isolating the fluid dynamics information layer by layer as close to the interface as possible.

The most recent works regarding this latter method are using nanometric fluorescent particles (quantum dots - 10 nm, technique more generally called nano particle image velocimetry - n piv), illuminated by a laser field confined in a 100 nm thickness layer from the surface through evanescent wave concept [Pouya et al., 2005]. They measure in this 100 nm liquid film, an average liquid velocity amounting to 1% of the mean flow speed. Even if this result is important and provides quite accurate data, we do not know yet what is really going on as close to the interface as one single molecular dimension, that is to say, a few Å-nm.

A solution to overcome this limitation would be to go through second-order nonlinear optics which is specifically surface sensitive. Since a fluid is in average centrosymmetric, it shall not generate a nonlinear signal, this assumption is supposed to hold even for moving fluids (proved later by the experiment). Therefore, by determining the orientation of interfacial molecules (placed there only as a tool to detect the liquid-surface dynamical interactions) and by monitoring the angular modification while exposed to a liquid flow, it becomes possible to characterize the stress induced on the surface, and this, in a molecular size range from the wall through the fluid mechanical action.

4.4 Experimental conditions: molecule, set up...

The experiment is ran in a quartz micro flow cell (Starna-cell, 48-Q-0.1) of 100 μm thickness. The SHG is produced in a total internal reflection (TIR) configuration at the liquid-solid cell interface. This is achieved through the use of a quartz prism (Ealing, $\lambda/10$, laser quality right angle fused silica prism) placed side by side with the flow cell and the use of an appropriate index oil (glycerol, Sigma-Aldrich 99,8%) to ensure a refractive index continuity. A schematic drawing of the set up is presented in figure 4.2.

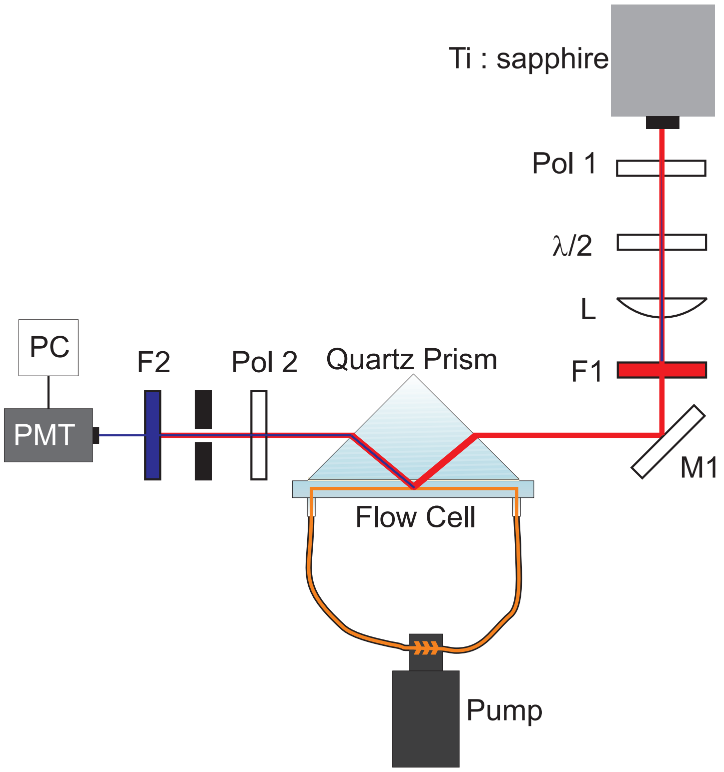

Figure 4.2: *Drawing of the SHG set up. Pol 1 - polarizer ; $\lambda/2$ - half wave plate ; L - lens ; F1 - 390 nm filter ; M1 - mirror ; Pol 2 - analyzer ; F2 - 780 nm band filter ; PMT - photomultiplier tube ; PC - personal computer.*

The choice of the TIR configuration is based on different requirements. Likewise, the beam does not go through the liquid solution. The interface is probed only by the evanescent field during the TIR process. Since the TIR condition may be achieved only if the light beam comes from a higher refractive index medium to a lower one, the solid medium should hold the highest index. This latter have to be transparent for the laser radiation, and set up in a way to minimize the loss of intensity when the beam enters and leaves it. A regular quartz prism represents a fair choice regarding the laser source.

Briefly, a mode locked Ti:sapphire oscillator (spectra physics, tsunami 3960), producing a 82 MHz pulse train with 100 fs pulse duration and being tunable from 750 to 850 nm, is sent on the interface. Prior probing this latter, the beam firstly passes through a polarizer and a half wave plate in order to control the incident polarization. A lens is then placed to focus the beam on the interface. Just before producing the second harmonic signal, a filter (Ealing, color glass filter RG665) is placed to remove any previous SHG that might be generated by any optical component such as mirror or wave plate. Hence, by using a prism, the beam is directed to the liquid-cell interface in a total internal reflection configuration. The generated second harmonic beam goes through an analyzer in order to be either s or p polarized, after what it is sent towards 3 different filters, two colour glass filters (Ealing BG39) to remove all the fundamental wavelength component and a pass band filter (Ealing 35-3204) to remove the surrounding light. Thereafter, the pure SHG signal went through a photomultiplier tube (Hamamatsu), prior being counted by a boxcar integrator and readed by a Labview interface.

Regarding the quartz cell, tapping mode AFM reveals that its surface has a mean roughness of 2 nm over a 10 μm side square area. Relatively speaking, we may compare interfacial molecules over this 100 μm^2 location as a flower carpet spreading over a 1 km^2 field where the most prominent holes and humps would size 10 cm high and 20 m in diameter. The flow cell may therefore be assumed to be flat and the flow profile immedialely adjacent to it, poorly affected by the surface morphology.

The liquid flow in the cell is induced by a pump in a closed circuit set up (Micropump ®- Cavity style pump heads + Modular gear pump drive). This magnetically driven pump ensures a smooth, accurate and pulseless fluid delivery. Moreover, since the mechanical action is magnetically driven remotely, there is absolutely no contact between the liquid chamber and the engine compartment. The connections between the flow cell and the pump are made by some laboratory tubing (Tygon R-3603, NALGENE 180) with diameters of 3.2 mm (1/8 inch) and 6.4

mm (1/4 inch). The particularly choice of the tube is based on the viscosity of the liquid only, since the real section of the flow is limited by the flow cell section itself (100 μm × 8 mm). However, since the value of the fluid viscosity is varied on a wide scale, the need of a larger tube section is justified in order to maximize the flow through the Poiseuille's law when working at high viscosity. The control of different shear rates is achieved by tuning the variable flow of the pump and by the use of appropriate tube section. The effective liquid speed in the cell was a few 10 cm/s.

The required fluid viscosity is obtained by mixing pure water with glycerol (Sigma-Aldrich, purity 99.8 %) in variable proportion [Dorsey, 1940]. The final liquid viscosity is included between η = 1 mPa s (pure water) and η = 50 mPa s (79 % in weight of glycerol, 21% of water). At "high viscosity" ($\eta \geq 20$), the solution is allowed to outgas during 30 minutes in a vacuum desiccator to remove all the air bubbles introduced during the mixing process. The overall capacity of the pump-tube-cell circuit was included in the 10 - 40 ml range, depending upon the tube diameter.

The chosen molecule for this study is the rhodamine 6G dye. This latter has a strong electrical dipole moment that enables to perform an efficient physisorption over charged interfaces like quartz. As a dye, it is also well disolved in water based mixture. The rhodamine solution concentration is $5\,10^{-5}$ M, determined from previous studies [Kikteva et al., 1999] [Simpson and Rowlen, 2000b] [Slyadneva et al., 1999] as being the maximal concentration before the formation of aggregates.

The rhodamine physisorption at the quartz interface is performed directly by the injection of the dye based solution into the circuit. As depicted in figure 4.2, the solution is injected through the tube and the pump; thereafter the pump is run slowly a few seconds to fill up the micro flow cell, after which some delay is required for the dye interfacial concentration to reach its equilibrium through the physisorption process. While this is achieved, the spectroscopy study can begin.

The laser wavelength used in this experiment is 780 nm, based upon the electronic levels of the rhodamine (see figure 4.3). Indeed, the first excited electronic transition $S_0 \rightarrow S_1$ of the rhodamine is located at 529 nm with a dipole moment lying along the x' axis, the second transition $S_0 \rightarrow S_2$ is at 347 nm with the dipole moment along the z' axis and finally the $S_1 \rightarrow S_2$ transition is at 1010 nm along the x' axis (figure 4.3). Therefore, by using 780 nm, the first energy state is avoided with a single photon, as well as the second energy states with a two-photon energy process. The will to avoid any resonant interaction is made on purpose since this could lead to the generation of fluorescence which is a massive source of optical pollution, but can also lead to large photon absorption that may result in molecular damages at the probed interface.

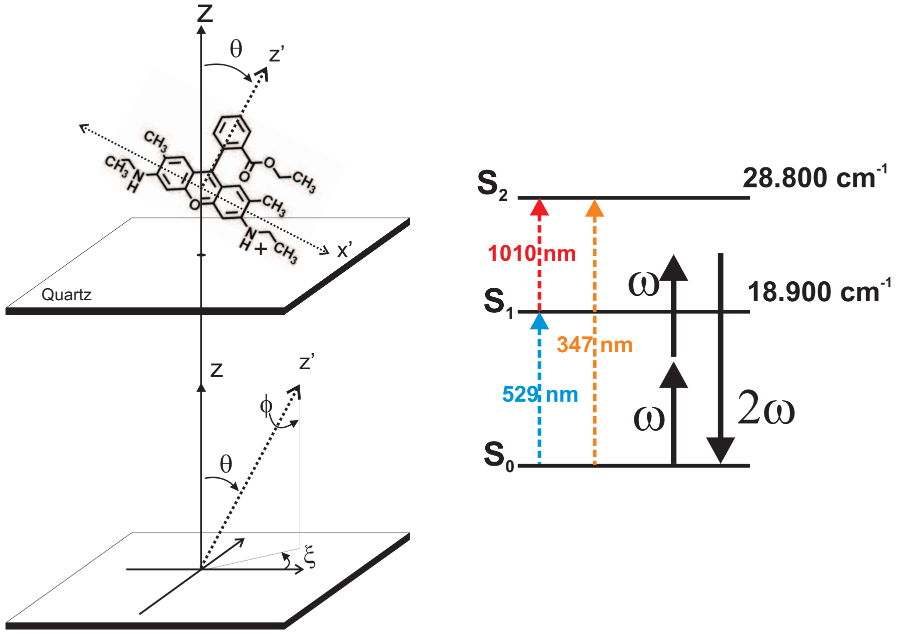

Figure 4.3: *Left. Rhodamine 6G molecule; the definition of the molecular axes x' and z', and the definition of the angles θ, ξ, ϕ relating the molecular coordinates to the surface ones. As defined in previous papers, θ is the angle between z' and the surface normal z. Right. Picture of the electronic levels of the R6G molecule. The chosen laser wavelengths, that is 780 nm (12820 cm^{-1}) and thus 390 nm from the SHG (25640 cm^{-1}) avoid any resonant process.*

Prior to running an experiment, a defined cleaning procedure is repeated each time before the injection of a new solution: the cell is cleaned through a repetitive injection/bath of ethanol, methanol, chlorhydric acid, and 18 MΩ bidistilled water. All tubes are changed prior to each new injection and new tubes are toroughly cleaned with pure water before usage. Finally, the pump is rinsed under water, then allowed to run in a small closed circuit configuration (without the flow cell, just a tube ring) several times with methanol and then water. This step is not negligible since small rhodamine aggregates appear into the solution while running the pump after a few days off. Those dye aggregates actually stick off the pump inner walls, what fully justifies the previous cleaning steps. The quartz prism is also cleaned under pure water and methanol since it is in contact with glycerol, used as index oil between the flow cell and the prism itself.

In order to achieve the total internal reflection condition at the liquid-cell interface, the incident angle of the fundamental beam (780 nm) on the prism entrance is adapted for each different glycerol mixture through Snell's law. Furthermore, in order to maximize the signal, the TIR angle value is chosen right after the critical angle. Indeed, a larger angle requires (for the quartz, air and water refractive index) the fundamental beam to go through the prism entry face with a larger incident angle (relatively to the interface normal), what leads to a decrease in the transmission coefficient. Note that this observation is based on intensities and not on electric field values, since we did not take Fresnel factors into account. Experimentally speaking, the TIR angle on the probed interface is around 70° from the normal.

Finally, prior to using the rhodamine solution, the SHG experiment was carried out with pure water to collect the quartz-water interface signature but also the glycerol-quartz one. Besides, free running water on the quartz interface was also investigated. The signals from all of those configurations were weak and, by far, small in comparison to the rhodamine layer signal intensity.

4.5 SHG measurements: the rhodamine orientation

The measurement procedure, described in the figure 4.4, is the following: a fundamental laser beam at 780 nm in sent to the rhodamine interface. Its polarization is beforehand controlled by a half wave plate. Initiated from the second-order susceptibility of the probed layer, two incoming photons will produce a single frequency doubled photon containing informations relative to the interfacial molecules. This SHG beam is emitted in a direction determined by the momentum conservation rule of the incoming photons and has a certain polarization distribution characteristic of the molecular orientation. To collect the SHG photons in a determined polarization (s or p), an analyzer is used. Hence, by scanning the incident polarization (780 nm), two different SHG intensity curves (s or p analyzer position) are recorded.

In order to simplify the second-order susceptibility tensor as well as angular parameters, assumptions are often made on molecular disposition symmetry. The more commonly assumed in dye studies is the in-plane azimuthal symmetry, which leaves the $\chi^{(2)}$ tensor expressed through three components only. This appears to be an easy step, but what is going on in our case where we plan to apply a moving and directional fluid on the surface?

Actually, we have two choices. First we can break the isotropy hypothesis and expect the molecular distribution to fairly align on the liquid flow. This is actually a huge task because the degree of anisotropy will evolve with time. Indeed, in this scenario, the molecules are expected to go from an isotropic distribution (before the flow is set on) over 360° to a certain width x° in the molecular distribution, reaches as an equilibrium state after a certain duration. Besides the fact that we have to handle a full component $\chi^{(2)}$ tensor, the isotropy hypothesis evolves during the measurement. This solution is far too complex to be solved here (if it is even ever possible!).

The second possibility is to keep the in-plane isotropy hypothesis over the whole measurement. This may first appear senseless, but we have two arguments to justify this choice. First, we have mentioned in section 4.3 that n-piv study measures a 1 % speed component over a 100 nm liquid layer from the interface. The speed component when acting even closer to the interface is for sure even smaller; this is well the reason why liquid slip is so difficult to observe. Is it thus careful to assume the fluid effect to be sufficient to produce a molecular alignment? Would it be unreasonable to consider a final distribution width X° so close to 360° that the isotropy hypothesis may hold? The second argument follows an observation realized in a R6G dye diffusion study. Some members among the professor Granick's team have shown that the dye, in a static condition, undergoes a rotational movement in a nanosecond range along the Z axis [Bae et al.,]. Since we are using an 82 MHz femtosecond pulsed laser, each one of these short pulses record one particular molecular distribution, those latter being averaged over a large pulse quantity. Even if once again, it may appear difficult to extent this observation to our dynamics work, we can put forward that the fluid effect on the dye is very smooth when as closed to the surface as nanometers, and is assumed to be not sufficient to annihilate this nanosecond time scale rotational movement. Finally, even if the isotropy postulate justification is found to be questionable, as it is actually the case for many works, it is the only way to process the SHG data here, the variable anisotropy conditions being too complicated to handle. It is however a very good topic for further investigations. Let us see what information we can obtained when posing the in-plane isotropy.

In this case, the ξ angle can be averaged from 0 to 2π. Moreover, the assumption of a random distribution of ϕ over 0 to 2π as it is often realized for dyes, leads to expressions of χ_{IJK} in terms of β_{ijk} and θ only [Higgins et al., 1992].

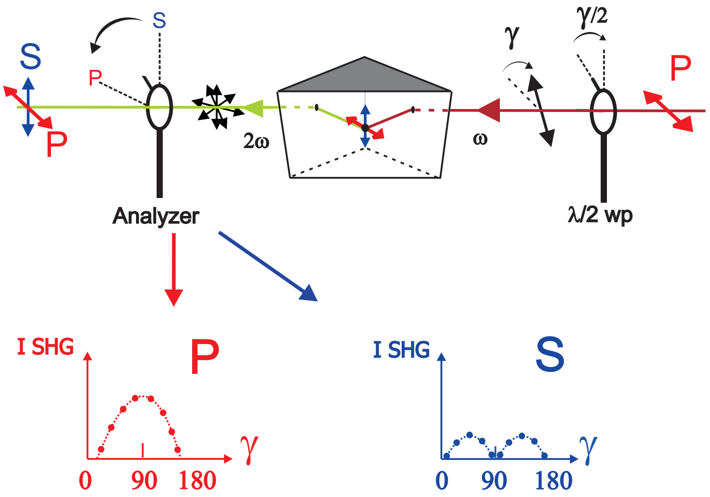

Figure 4.4: *Schematic drawing of the measurement. The polarization of the incident fundamental beam (780nm) is controlled through a half wave plate. Hence, the second harmonic is generated at the interface, with its own distribution of polarization. An analyzer is then used to select only one SHG polarisation component (s or p). Both s and p analyzer positions lead to a SHG intensity curve when scanning the incident polarization angle from 0 to 180˚.*

Let us rewrite equations 2.18 and 2.19 (Section 2.3) describing the intensity of such SHG beam in function of the incident polarization angle:

$$I_s^{2\omega}(\gamma) = \left|\chi_{xxz}\, b_1 \sin 2\gamma\right|^2 (I^\omega)^2 , \tag{4.1}$$

$$I_p^{2\omega}(\gamma) = \Big|\chi_{zxx}\, b_2 \sin^2\gamma + (\chi_{xxz}\, b_3 + \chi_{zxx}\, b_4 + \chi_{zzz}\, b_5)\cos^2\gamma\Big|^2 (I^\omega)^2 , \tag{4.2}$$

with I^{ω} the intensity of the fundamental laser beam, $I^{2\omega}$ the second harmonic signal intensity, the s and p subscripts point out the SHG polarization set by the analyzer, γ is the polarization angle of the fundamental beam relatively to the p polarization (as shown in figure 4.4). The b_i are coefficients depending upon the geometry of the set up and are described by the Fresnel factors (see section 1.8). Overall, they take into account the single refraction at the prism entry face, the total internal reflection occurring at the liquid-solid interface, and the refraction while the beam leaves the prism. From mathematical expressions 4.1 and 4.2, it becomes possible to fit the experimental curves obtained (explained in figure 4.4), and thus to extract the values of the second-order susceptibility tensor (as described in section 2.4).

The dominance of a single molecular polarizability tensor component based on a specific electronic transition resonance is often assumed in such dye based study [Peterson and Harris, 1989] [Dilazzaro et al., 1985] [Higgins et al., 1992]. However, other works attract attention to the fact that a single dominant molecular polarizability tensor component is not sufficient to achieve a correct description of the molecular response [Slyadneva et al., 1999] [Kikteva et al., 1999] [Kikteva et al., 2000] [Campbell et al., 1990] [Higgins et al., 1991] [Corn and Higgins, 1994] (discussed in section 2.5 and 2.6). Anyway, this experiment being run with wavelengths especially chosen to avoid any resonances, no assumption could be made on a dominant x' or z' polarized dipole moment resulting from an enhanced π electronic transition. Nevertheless, the majority of the studies carried out off resonance agree to consider both β_{zxx} and β_{xxz} to contribute to the total molecular polarizability for the rhodamine dye case [Slyadneva et al., 1999] [Kikteva et al., 1999] [Higgins et al., 1991] [Kikteva et al., 2000].

In order to quantify the contribution of both components, it can be derived from equation 2.24, an expression of their ratio free of any tilt angle and relying on the experimental χ_{zzz}, χ_{zxx} and χ_{xxz} data:

$$\frac{\beta_{x'x'z'}}{\beta_{z'x'x'}} = \frac{2\chi_{xxz} + \chi_{zzz}}{2\chi_{zxx} + \chi_{zzz}}. \tag{4.3}$$

From this relation, the measured macroscopic susceptibilities lead to a value of $(\beta_{z'x'x'}/\beta_{x'x'z'}) > 15$ for all experimental configurations. This high experimental ratio value, verified for all SHG curves, means that the $\beta_{x'x'z'}$ component is not significant in comparison to $\beta_{z'x'x'}$. This is also verified by an experimental agreement of the following expression as shown by Dick: χ_{zzz} = - $2\chi_{xxz}$ [Dick et al., 1985] [Simpson and Rowlen, 2000a] (experimental curve trends included between the C and D case in figure 2.2. Note however that the Fresnel factors were set to unity in chapter 2).

Consequently, only the $\beta_{z'x'x'}$ component of the molecular nonlinear polarizability tensor will be further considered. For the determination of the average molecular orientation angle, a second relation can be extracted from equation 2.24. This expression is based upon the three macroscopic susceptibility terms χ_{zzz}, χ_{zxx} and χ_{xxz} and is made free of $\beta_{z'x'x'}$ by the use of an appropriate ratio [Dick et al., 1985]:

$$\frac{< cos^3\theta >}{< cos\theta >} = \frac{2\chi_{zxx} - \chi_{zzz}}{2\chi_{zxx} + \chi_{zzz}}. \qquad (4.4)$$

To resume, to retrieve molecular orientation from the SHG polarization measurement, one (or two) dominance among the microscopic $\beta^{(2)}$ component has to be set (at least in this way to proceed where we are not evaluating the $\beta^{(2)}$ component values by analytical or other methods). The determination of the dominant $\beta^{(2)}$ component may be achieved from the macroscopic $\chi^{(2)}_{IJK}$ components, those latter being experimentally determined from polarization SHG measurements. Once the dominant $\beta^{(2)}$ component is identified, a dedicated molecular orientation formula is deduced from equation 2.24. This formula (equation 4.4) holds only for a specific case of $\beta^{(2)}$ dominance (β_{zxx} here), each different dominance leading to different simplifications in equation 2.24 and to distinct formulas.

4.6 Spectra of rhodamine at liquid-solid interface

The figure 4.5 shows the evolution of the interfacial second harmonic response consequently to the onset of the flow. The fluid is a mixture of pure water and glycerol, the viscosity is 20 mPa s and the flow speed is 20 cm/s. With the onset of the flow, a change in the SHG intensity trend is observed for both s and p polarizations. From this, a change in the susceptibility component values is deduced (equation 4.1 and 4.2) and a θ angle value for each couple of s and p polarization curves may be extracted (equation 4.4). Hence a curve relating the tilt angle modification of the dye consequently to the liquid flow may be plot in relation to time.

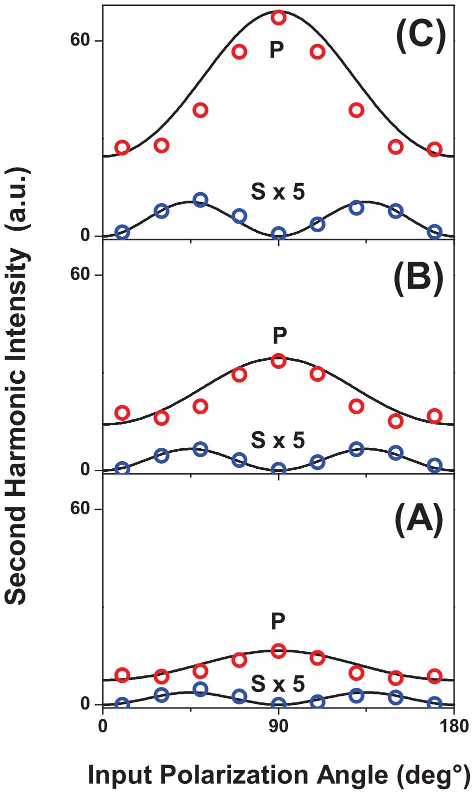

Figure 4.5: *Evolution of the SHG intensity in s and p polarizations resulting from the flow onset. The fit (plain line) results from equation 4.1 and 4.2. A first measurement is taken in static condition (A), then, after the onset of the flow, further measurements are recorded at regular time intervals and an evolution in the interfacial optical response is observed (B) and (C).*

Experimentally, when the rhodamine concentration has reached its equilibrium at the quartz flow cell surface, a first couple of measurment (S and P polarization) is taken in a static condition (panel A in figure 4.5). Thereafter, the liquid flow is turned on and an increase in the SHG signal intensity is gradually observed with time (panels B and C). A full set of measurements contains about ten curves taken at regular time intervals until the signal intensity comes to stabilisation. Notice that this augmentation of intensity is not equivalent for the s and the p polarization.

Although it is common that an increase of the second harmonic intensity is caused by a modification of the interfacial molecular concentration (that may be induced by the flow), a dissymmetry in the s and p intensity ratio emerging from the interface can not so easily be attributed to a surface coverage change. Actually, it has been shown in previous static studies that the modification of the rhodamine 6G molecular orientation as a function of the concentration, and then of the surface coverage, is very small for such rhodamine solution concentration ($5\,10^{-5}$ M). Moreover, in this concentration range, the surface coverage modification induces only slight second harmonic intensity changes [Simpson and Rowlen, 2000a] [Simpson and Rowlen, 2000b]. However in this study, the second harmonic intensity clearly multiplies itself a few times (between 4 and 7) with the fluid motion. While such increase cannot be attributed to an interfacial rhodamine concentration variation, the dissymmetry in the s and p signal intensity increase, leading to the θ tilt angle modification, cannot be either.

One possible explanation is the reorganization effect induced by the liquid flow stress acting on the molecular film. In this frame, the observed signal modification is specifically attributed to the dynamic effects induced by the liquid rather than to the change of interfacial coverage induced by the liquid movement. The so-produced force acting on the dye molecules leads therefore to slow structural modifications of the rhodamine layer. The averaged θ tilt angle variation being applied to an isotropic distribution of dye molecules, that means that the whole layer undergoes a flattening mechanism. This probably leads to a more structured film with narrow angular distribution.

The static tilt orientation value for the rhodamine 6G relative to the interface normal axis seems to be quite independent from the viscosity of the aqueous mixture. The common values measured during this study are included in the 51° - 58° range from the normal (see figure 4.3). From the dynamic part of this study, a θ tilt angle decrease included in the [5° - 15°] range is reported consequently to the onset of the flow. A typical reorientation curve is shown in figure 4.6 for which the liquid speed was of 20 cm/s and the viscosity of 20 mPa s. From the scheme in figure 4.3, this means that the rhodamine 6G molecule tends to lay down on the surface while under a flow shear.

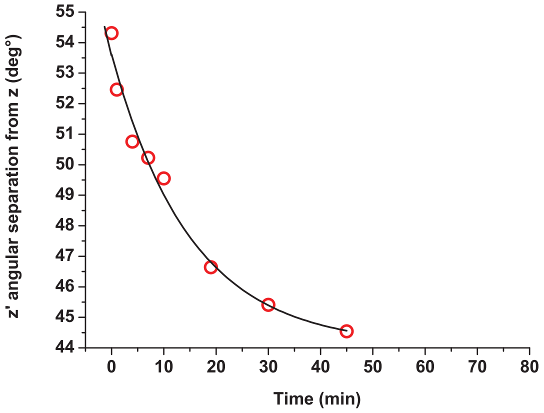

Figure 4.6: *Evolution of the angular separation between the rhodamine z' axis and the surface normal z with time. The fluid viscosity is* $\eta = 20$ *mPa s and the flow speed is 20 cm/s. The decay constant* λ *is 6,57* $10^{-2} s^{-1}$*, C = 44.1, and A0 = 9.55.*

In order to quantify this z' axis angular modification in response to the flow, a fit of the curve trend to an exponential decay function is realized (see figure 4.6). Indeed, assuming that directly after the onset of the flow, a new equilibrium state of the dye is defined, this latter is reached in an exponential decay dynamics as described by the following relation:

$$\theta(t) = C + A_0 e^{-\lambda t} \tag{4.5}$$

where the constant C represents the tilt angle value of the dye in its new equilibrium state, A_0 is the amplitude of the decay and λ is the decay constant.

The decay constant is an important factor for consistency as it reflects the efficiency of the fluid to act through its shear rate and viscosity on the rhodamine orientation, to reach the new equilibrium state ($C+A_0 \rightarrow C$). Therefore, all future stresses resulting from fluid effects will be plotted versus the decay constant. A small value of λ involves a very smooth modification of the dye orientation and thus tiny dynamic effects acting on the R6G to reach a new equilibrium state. In contrast, a high value of λ means sharp dynamic effects acting on the dye, underlining therefore the ability of the fluidic constraint to act at the interface.

4.7 Shear rate and shear stress effects on the interface

Experimentally, two set of measurements are realized. The first one varies the shear rate (flow speeds of 20, 30, 40 cm/s) and keeps a constant viscosity of the fluid (η = 10 mPa s). The second one keeps a constant shear rate (20 cm/s) for three different fluid viscosities (η = 10, 20, 50 mPa s). A decay constant is established for each curve (the results are not shown here since it is mostly the same time evolution trend as the one shown in figure 4.6 for η = 20 mPa s and v = 20 cm/s).

In the first set of measurements, the shear rate is quantified. The shear rate, defined as the velocity gradient within the flowing material, is determined from the flow cell dimensions. The channel thickness (x) is of 100 μm and its width (y) is 8 mm. Therefore, we can assume the shear rate to be relative to the x axis only, the one on the y axis being two orders of magnitude smaller. The expression of the shear rate along x is given by:

$$\gamma_x = \frac{\delta v}{\delta x}. \tag{4.6}$$

The flow speed being maximal at the midpoint of the channel, a distance of 50 μm should be considered as δx in the calculation of the mean shear rate.

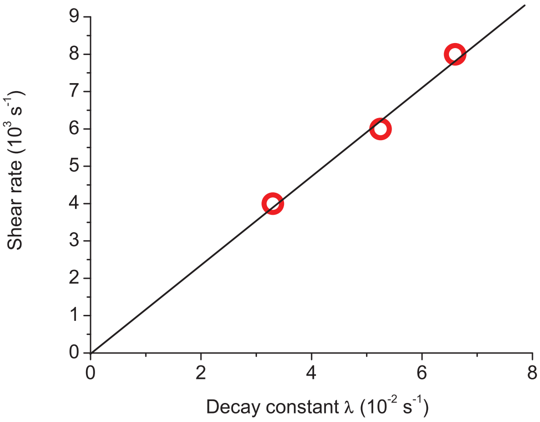

Figure 4.7: *Shear rate in function of the decay constant λ. A linear fit passes through the origin, as it should be for all Newtonian fluids.*

The figure 4.7 represents the relation between the shear rates and the decay constants resulting from the first set of measurements. The relationship between the flow strain and the shear rate is linear and passes through the origin. The decay constant being a quantitative tool to measure the efficiency of the fluid to act on the rhodamine, the reaction of the dye in terms of orientation modification dynamics is proportional to the flow strain. Consequently, if the fluid speed is multiplied by x, the dynamics response of the rhodamine will be likewise multiplied by a factor proportional to x.

The second set of measurements is dedicated to provide information relative to the wall shear stress through the viscosity of the liquid:

$$\tau_x = \eta \left. \frac{\delta v}{\delta x} \right|_{x=0} . \tag{4.7}$$

A viscous fluid moving along a solid boundary will produce a shear stress on it. The no slip condition states that the speed of the fluid at the interface is zero. But there is unavoidably a gradient of speed in the liquid in order to reach the speed of the fluid in the central region of the channel. The region between these two points is named the boundary layer. The shear stress is applied onto the boundary as a result of this loss of velocity. The unit is a force divided by an area (the Pascal (Pa)).

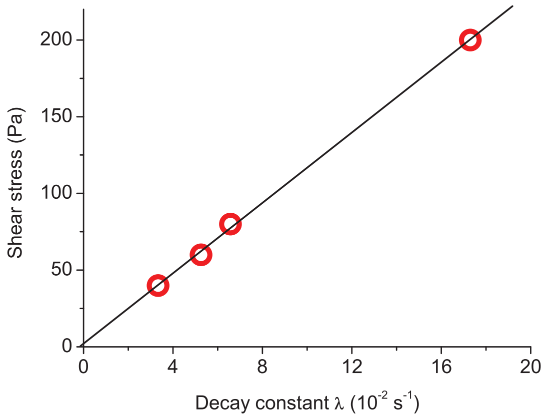

Figure 4.8: *Wall shear stress in function of the decay constant λ. A linear fit passes through the origin, as it should be for all Newtonian fluids.*

The figure 4.8 shows the results from the second set of measurements. Again, a linear relation passing through the origin between the stress and the decay constant is observed, which is characteristic of a Newtonian fluid. This linear relation involves that the modification in the dynamic of the rhodamine orientation caused by the flow is proportional to the force upon the area resisting the shear. If the force is reduced to zero, the variation of the rhodamine dipole angle with time vanishes.

From these two curves (fig. 4.7 and 4.8), a direct correlation between flow speed and fluid viscosity from one side and the dynamical response of the dye from the other side is established. However, this dynamic motion of the dye is set up on the decay constant itself based on timescale motion only and does not take into account the amplitude value A_0 of the fit.

Independently of a time factor, the amplitude of the tilt angle variation has also been studied in function of the surface shear stress. Indeed, if we assume that for each flow parameter, a new equilibrium state in the rhodamine dye orientation is determined, it is possible to extract informations about the evolution of this state value with the stress undergone by the molecule. The figure 4.9 plots this relation.

A linear relation between the amplitude variation of the molecular tilt angle and the surface stress is observed for moderated shear stress values. For higher values, it appears that the amplitude of the angular modification slows down (the measurement having been done twice). If a definitive explanation can not be emitted, we can put forward that, when in its equilibrium position, the dye is set in its more stable energetic positioning relatively to its environment. To move the molecule away from this position, the energy that should be brought follows the shape of an interaction potential. We may expect that, to induce an important modification of the dye orientation, the interaction potential is no more linear and that more and more energy have to be employed. This could be in charge of the nonlinearity observed between the stress and the reorientation amplitude for large values of this latter. Besides, we have to assume that the duration of the dynamic process to go from the initial state to the final one is not modified since the figure 4.8 shows a linear relation even for high surface stress conditions. In consequence, the decay constant λ does not fall aside the linear relation but the absolute variation of the tilt does it. Conceptually, this seems right since the modification of the rhodamine orientation has to remain lower than $\sim 55^\circ$. In this extreme case, the dye would lay absolutely flat on the substrate. A fit of the curve depicted in figure 4.9 to an exponential growth would show that a shear stress of 100.000 Pa is necessary to do so.

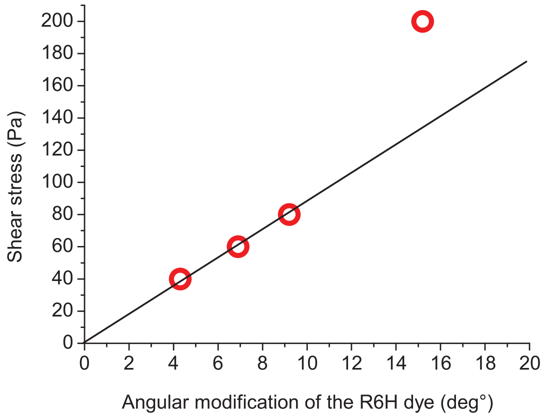

Figure 4.9: *Amplitude of the rhodamine angular modification in function of the surface stress.*

To resume, shear stresses induced by liquid flow induce a modification in the equilibrium tilt angle of the dye molecule. The dynamics of the movement is linear with the stress through the λ decay constant while the absolute value of the angle modification seems to slow down from linear relation with the stress. If our hypotheses are right, that would mean that for very high stress conditions, the tilt angle modification would reach a maximum "constant" value, but the time to go from one state to the other would be smaller and smaller with the shear stress. This appears quite reasonable actually.

What can we conclude from this set of measurements? We have observed that whatever the flow speed and the flow viscosity, the dynamics of the dye reorientation is proportional to them. However, in this model, the reorientation of the dye has to be treated as a flattening of the rhodamine film because of the layer isotropy, and not as a direct directional flow effect. Through Poiseuille's law, the pressure variation in the flow cell is proportional to the liquid speed and viscosity. Therefore, all those effects could be interpreted in terms of fluidic pressure acting at the interface on the dye molecules.

Where is the place for liquid slip in there? We can mention that in case of slips against the surface, the fluid velocity should become higher in a layer close to the interface. The local pressure should decrease (from the Bernouilli's principle) and thus the dye flattening effect as well. However, from the figures 4.7 and 4.8, the relations remain linear. It is therefore difficult to state about an hypothetic effect of a liquid slip over the dye molecule in our experiment. A more complete description of the molecular dynamics has to be considered to fully take advantage of our measurements. We can however underline the interesting contribution of this nonlinear SHG spectroscopy to characterize interactions happening at interfaces under a stress resulting from a liquid flow.

4.8 Resume

A nonlinear second-order spectroscopy such as the second harmonic generation, well known to be able to probe very selectively surfaces and interfaces, has been performed in dynamic evolutionary conditions (i.e. very unusual conditions). The intrinsic properties of SHG have forced the confinement of a dynamic phenomenon to be studied in a molecular thickness layer of few nanometers at the solid surface. Even at this scale, a Newtonian behaviour of the fluid was observed, and a clear fluid effect through surface stress was underlined. We demonstrate the structural impact produced by a moving fluid on a molecular layer physisorbed at the interface. This latter layer undergoes a molecular re-orientation under a viscous fluid flow. The dynamics of this molecular flattening is linearly related to the shear rate but also to the shear stress through the fluid viscosity. Moreover, the amplitudes of the tilt variation, included in the 5° - 15° range in this experiment, seem to be linear with the stress excepted for high stress conditions for which the angle modification tends to slow down. All these observations point out an effective ability of the liquid to act on the rhodamine layer. However, a more complete model of the interfacial system has to be considered to underline a possible slip effect.

This SHG study shows that nonlinear optical techniques could be a complementary tools to surface force apparatus and nanoparticles image velocimetry (npiv) in the liquid-solid interaction investigations.

4.9 Bibliography

[Bae et al.,] Bae, S., Wong, J., and Granick, S. Under publication.

[Barrat and Bocquet, 1999] Barrat, J. L. and Bocquet, L. (1999). Influence of wetting properties on hydrodynamic boundary conditions at a fluid/solid interface. Faraday Discussions, (112):119–127.

[Campbell et al., 1990] Campbell, D. J., Higgins, D. A., and Corn, R. M. (1990). Molecular 2nd harmonic-generation studies of methylene-blue chemisorbed onto a sulfur-modified polycrystalline platinum-electrode. Journal of Physical Chemistry, 94(9):3681–3689.

[Corn and Higgins, 1994] Corn, R. M. and Higgins, D. A. (1994). Optical 2nd-harmonic generation as s probe of surface-chemistry. Chemical Reviews, 94(1):107–125.

[Dick et al., 1985] Dick, B., Gierulski, A., and Marowsky, G. (1985). Determination of the nonlinear optical susceptibility x(2) of surface-layers by sum and difference frequency generation in reflection and transmission. Applied Physics B-Photophysics and Laser Chemistry, 38:107–116.

[Dilazzaro et al., 1985] Dilazzaro, P., Mataloni, P., and Demartini, F. (1985). Orientation of xanthene adsorbate molecules at dielectric interfaces. Chem. Phys. Lett., 114(1):103–108.

[Dorsey, 1940] Dorsey, N. (1940). Properties of ordinary water-substance. New York, page 184.

[Franken et al., 1961] Franken, P. A., Hill, A. E., Peters, C. W., and Weinreich, G. (1961). Generation of optical harmonics. Physical Review Letters, 7(4):118.

[Giordano and Cheng, 2001] Giordano, N. and Cheng, J. T. (2001). Microfluid mechanics: progress and opportunities. Journal of Physics-Condensed Matter, 13(15):R271–R295.

[Granick et al., 2003] Granick, S., Zhu, Y. X., and Lee, H. (2003). Slippery questions about complex fluids flowing past solids. Nature Materials, 2(4):221–227.

[Granick-Group, 2007] Granick-Group (2007). http://groups.mrl.uiuc.edu/granick/.

[Higgins et al., 1992] Higgins, D. A., Abrams, M. B., Byerly, S. K., and Corn, R. M. (1992). Resonant 2nd harmonic-generation studies of p-nitrophenol adsorption at condensed-phase interfaces. Langmuir, 8(8):1994–2000.

[Higgins et al., 1991] Higgins, D. A., Byerly, S. K., Abrams, M. B., and Corn, R. M. (1991). 2nd harmonic-generation studies of methylene-blue orientation at silica surfaces. Journal of Physical Chemistry, 95(18):6984–6990.

[Jin et al., 2004] Jin, S., Huang, P., Park, J., Yoo, J. Y., and Breuer, K. S. (2004). Near-surface velocimetry using evanescent wave illumination. Experiments in Fluids, 37(6):825–833.

[Joseph et al., 2006] Joseph, P., Cottin-Bizonne, C., Benoit, J. M., Ybert, C., Journet, C., Tabeling, P., and Bocquet, L. (2006). Slippage of water past superhydrophobic carbon nanotube forests in microchannels. Physical Review Letters, 97(15):–.

[Kikteva et al., 2000] Kikteva, T., Star, D., and Leach, G. W. (2000). Optical second harmonic generation study of malachite green orientation and order at the fused-silica/air interface. Journal of Physical Chemistry B, 104(13):2860–2867.

[Kikteva et al., 1999] Kikteva, T., Star, D., Zhao, Z. H., Baisley, T. L., and Leach, G. W. (1999). Molecular orientation, aggregation, and order in rhodamine films at the fused silica/air interface. Journal of Physical Chemistry B, 103(7):1124–1133.

[Massey, 1989] Massey, B. (1989). Mechanics of fluids, 6th edition, section 5.6. pages Chapman and Hall, London.

[Migler et al., 1993] Migler, K. B., Hervet, H., and Leger, L. (1993). Slip transition of a polymer melt under shear-stress. Physical Review Letters, 70(3):287–290.

[Peterson and Harris, 1989] Peterson, E. S. and Harris, C. B. (1989). A new technique for the determination of surface adsorbate geometries utilizing 2nd harmonic-generation and absorption-band shifts. Journal of Chemical Physics, 91(4):2683–2688.

[Pit et al., 2000] Pit, R., Hervet, H., and Leger, L. (2000). Direct experimental evidence of slip in hexadecane: Solid interfaces. Physical Review Letters, 85(5):980–983.

[Pouya et al., 2005] Pouya, S., Koochesfahani, M., Snee, P., Bawendi, M., and Nocera, D. (2005). Single quantum dot (qd) imaging of fluid flow near surfaces. Experiments in Fluids, 39(4):784–786.

[Reiter et al., 1994] Reiter, G., Demirel, A. L., Peanasky, J., Cai, L. L., and Granick, S. (1994). Stick to slip transition and adhesion of lubricated surfaces in moving contact. Journal of Chemical Physics, 101(3):2606–2615.

[Schmatko et al., 2005] Schmatko, T., Hervet, H., and Leger, L. (2005). Friction and slip at simple fluid-solid interfaces: The roles of the molecular shape and the solid-liquid interaction. Physical Review Letters, 94(24).

[Simpson and Rowlen, 2000a] Simpson, G. J. and Rowlen, K. L. (2000a). Orientation-insensitive methodology for second harmonic generation. 1. theory. Analytical Chemistry, 72(15):3399–3406.

[Simpson and Rowlen, 2000b] Simpson, G. J. and Rowlen, K. L. (2000b). Orientation-insensitive methodology for second harmonic generation. 2. application to adsorption isotherm and kinetics measurements. Analytical Chemistry, 72(15):3407–3411.

[Slyadneva et al., 1999] Slyadneva, O. N., Slyadnev, M. N., Tsukanova, V. M., Inoue, T., Harata, A., and Ogawa, T. (1999). Orientation and aggregation behavior of rhodamine dye in insoluble film at the air-water interface under compression. second harmonic generation and spectroscopic studies. Langmuir, 15(25):8651–8658.

[Zhu and Granick, 2001] Zhu, Y. X. and Granick, S. (2001). Rate-dependent slip of newtonian liquid at smooth surfaces. Physical Review Letters, 8709(9):096105.

Chapter 5

Sum-frequency generation spectroscopy

5.1 Introduction

The sum-frequency generation spectroscopy may be qualified as a young and novel technique since it is only 20 years old. Indeed, it has been demonstrated by Zhu and Shen in 1987 [Zhu et al., 1987] for the first time, after what, its application has been broadened to many domains in surface studies. Well distinct from the SHG, the SFG mechanism is based upon vibrational activity of specific chemical groups. Therefore, while the SHG probes electronic molecular dipoles at fixed wavelengths, the SFG probes a whole set of vibrational dipolar transitions by tuning the infrared beam frequency. It is interesting to notice that from the vibrational origin of the SFG, the nonlinear signal may be correlated to specific molecular locations relatively to the chemical architecture, and this by an appropriate choice of the wavelength. This chapter is dedicated to the illustration of the SFG spectroscopy principles, how to perform it, how to obtain conformational informations from the studied molecular system, how to retrieve molecular orientations? Along with spectra analysis, the experimental set up will be detailed.

5.2 SFG : a vibrational spectroscopy

As mentioned in the section 3.3, the vibrational sum-frequency generation mechanism is based upon both infrared and Raman activities. Those two linear spectroscopies are initiated from the same physical origin: a molecular inter-atomic bond absorbed an energy amount matching some allowed transitions between different vibrational energy states. However, from their own nature, certain vibrations are only IR or Raman active, while others possess both activities. In a centrosymmetric molecular environment, a "mutual exclusion rule" takes place, stating that a vibration may not be simultanously IR and Raman active. This is another way to show that SFG is inactive in media with inversion center since it requires both processes to be active at the same time. Therefore, if building a molecular vibrational fingerprint requires the two techniques (IR & Raman), coupling them within the same nonlinear process turns the SFG into a more selective vibrational spectroscopy regarding the active modes.

Let us rewrite synthetically the major equations taking part in the SFG intensity description:

$$I_{SFG} \propto |\chi^{(2)}_{eff}|^2 \; I_{Vis} \; I_{IR} \, . \tag{5.1}$$

The effective surface nonlinear susceptibility $\chi^{(2)}_{eff}$ is defined as:

$$\chi^{(2)}_{IJK,eff} = [F_{II} \, e_I]_{(\omega_{SFG})} \; \chi^{(2)}_{IJK} \; : \; [F_{JJ} \, e_J]_{(\omega_{Vis})} \, [F_{KK} \, e_K]_{(\omega_{IR})} \, , \tag{5.2}$$

with $\overrightarrow{e}_{(\omega)}$ a unit polarization vector, and $\overleftrightarrow{F}_{(\omega)}$ the Fresnel factor tensor, both for a electric field of ω angular frequency (see chapter 1). $\chi^{(2)}_{IJK}$ is the sum of one resonant and one non-resonant term:

$$\chi^{(2)}_{IJK} = \chi^{(2)}_{IJK\,(NR)} + \chi^{(2)}_{IJK\,(R)} \, , \tag{5.3}$$

with the resonant part defined as follows:

$$\chi^{(2)}_{IJK\,(R)} = N_s \sum_{ijk} \langle \, T^{ijk}_{IJK} \, (\theta, \phi, \xi) \, \rangle \beta_{ijk\,(R)} \, , \tag{5.4}$$

where N_S is the surface density of the molecules, (I, J, K) refer to the laboratory coordinates (x, y, z), while (i, j, k) refer to the coordinates attached to each molecule, and the angle bracket denotes an average over a molecular orientational distribution. Near the resonance, the molecular hyperpolarizability can be written as:

$$\beta_{ijk\,(R)} = \sum_{q} \frac{\beta_{q,\,ijk}}{\omega_q - \omega_{IR} - i\Gamma_q} \quad , \tag{5.5}$$

where $\beta_{q,\,ijk}$, ω_q, and Γ_q denote the strength, the resonant frequency, and the damping of the q^{th} vibrational mode, respectively. The $\beta_{q,\,ijk}$ components may be written in terms of the product of the infrared dipole derivative and the Raman polarization tensor derivative, with respect to the normal coordinate Q_q of the q^{th} vibrational mode:

$$B_{q,\,ijk} \propto \left(\frac{\partial \alpha_{ij}}{\partial Q_q}\right)\left(\frac{\partial \mu_k}{\partial Q_q}\right), \tag{5.6}$$

Those last two steps were generalized in chapter 3. One can see from equation 5.5 and 5.6 that each time the scanned IR frequency matches the one of a particular vibrational mode being both Raman and IR active, the SFG intensity is enhanced. The reader should notice that the regular SFG spectroscopy is performed by tuning the IR frequency while keeping a fixed visible wavelength. This involves a vibrational resonance only (simply resonant SR-SFG), while the slowly variable SFG frequencies are far from any resonance of the atomic system. To go further, it is possible to turn the SFG into a doubly resonant spectroscopy process (DR-SFG). For this purpose, the SFG frequency has to match a particular energy state of the system as well as the IR. This step requires a tuneable visible source as well as an IR one. Notice that for this doubly resonant mechanism, the expression of the β_{ijk} (see chapter 3) should include one supplementary resonant part for the SFG beam.

Finally, it is interesting to point out that those nonlinear susceptibilities and polarizabilities are complex numbers that behave in terms of amplitudes and phases. This may be highlighted by rewriting equation 5.3 as:

$$\chi^{(2)}_{IJK} = |A_{(NR)}|\, e^{i\,(\psi_{NR})} + \sum_{q} \frac{|A_{(R),\,q}|\, e^{i\,(\psi_{R,\,q})}}{\omega_q - \omega_{IR} - i\Gamma_q}\,, \tag{5.7}$$

with ψ_{NR} the non resonant phase and $\psi_{R,q}$ the phase of the q^{th} vibrational mode. The phase difference between a vibrational mode and the non resonant, but also between the different vibrational modes themselves, can fully modify the aspect of an experimental spectra depending upon the constructive or destructive phase interference nature.

5.3 Laser sources set up

The goal of this section is to present a quick review of the required optical tools to perform sum-frequency generation nonlinear spectroscopy. Since laser applications represent one of the main activities in our laboratory, the different experimental set up and the associated underlying theories have been widely detailed in one particular thesis and various publications [Mani, 2004] [Mani et al., 2001] [Mani et al., 2002]. Consequently, we will not go too deep into the details.

Basically, the SFG process relies on the one hand on a tuneable IR source to probe vibrational modes, and in the other hand on a visible (fixed for SR-SFG or tuneable for DR-SFG) source. Of course, the broader the IR frequency range is, the broader the probed vibrational window will be. We therefore need to extend the tunability of the IR laser source as far as it is technically possible. However, before describing the new frequency generation mechanisms that enable to achieve tunable sources, we have to discuss the nature of the laser pump employed as well as its temporal profile.

The temporal structure of the laser emission is very important. Indeed, to induce nonlinear effects, pulsed laser sources are required (as mentioned in section 1.3). However, what is the most appropriate pulse duration regarding sum-frequency generation spectroscopy? The typical pulse duration in regular laser applications is included within the nanosecond - femtosecond range. However, the longer the laser pulses, the lower the peak power (bad to exalt nonlinear effects), but in the same time, the better becomes the spectral resolution through Fourier transform relation (good for vibrational resolution). In order to fairly fulfil both the peak power value and the spectral resolution, we will choose the intermediate picosecond pulsed regime. Nevertheless, femtosecond pulses may be used for broadband applications in which the wavelength is no longer tuned since one single pulse covers all the desired spectral window.

The picosecond pulsed laser source is a home made all-solid state device (shown in the figure 5.1). Although commercial sources are available, the home made solution has undeniable advantages since it is easy to customize, cheaper, and finally, it turns us self-sufficient. The all-solid laser cavity is based on a Nd:YAG rod optically pumped by krypton flash lamps. This particular configuration is quite regular because of the Nd:YAG advantageous qualities: it is highly compatible with optical pumping method since its absorption energy bands match the krypton flash lamps emission ones, it has a good thermal conductivity (to evacuate the accumulated non-radiated energy), and finally is a "cheap" material because widely commercialized.

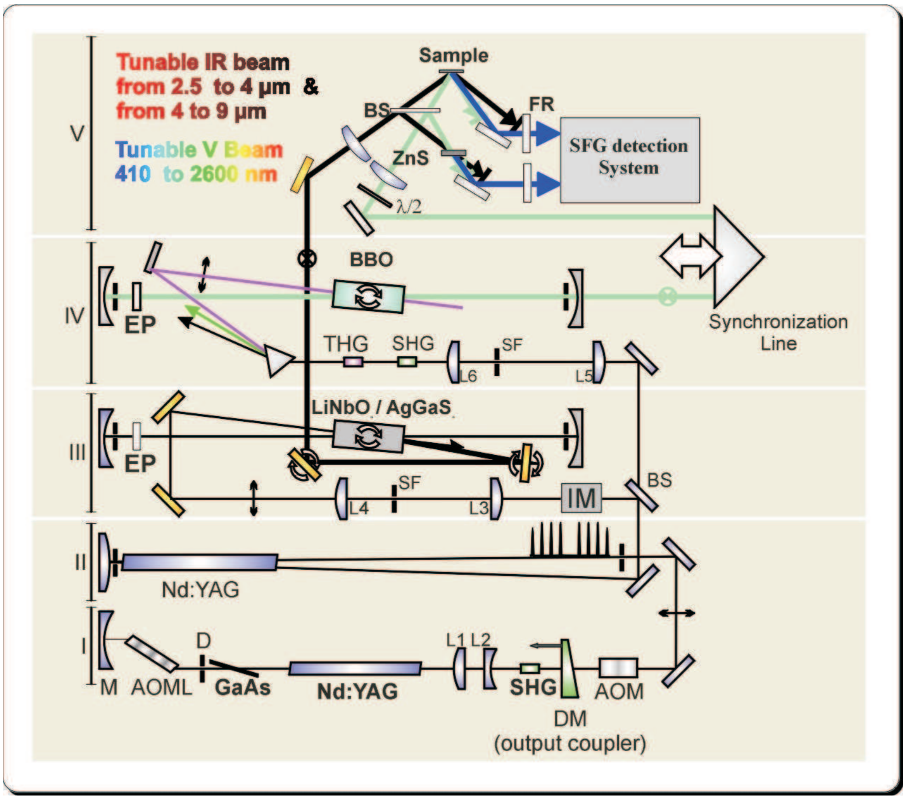

Figure 5.1: *Scheme of the SFG setup. Stage I is the all-solid state oscillator, stage II is the amplifier, stages III and IV are the IR and Vis OPO, and stage V is the SFG generation from the sample and the signal detection.*

When placed into a mirror cavity, this set up (Nd:YAG rod + flash lamps) emits laser radiation at 1064 nm. This near IR source is designated thereafter as the pump beam. The temporal profile of the laser emission is controlled by different electro/optic devices. In our set up, this allows to generate a single bunch of 100 pulses every 40 ms (25 Hz), each of those pulses lasting around 20 ps. This pump beam is then amplified through a second Nd:YAG rod, again optically pumped, to reach a power of 1,5 W (60 mJ per bunch, 600 μJ per 20 ps pulse, 30 MW peak power). This power is then shared between two different laser paths intended to synchronously pump two distinct optical parametric oscillators (OPO) as depicted in figure 5.1. Those OPOs allow the generation of new frequencies from the pump beam. This phenomenon is based itself on a second-order nonlinear process occurring in the bulk of non-centrosymmetric crystals (birefringent).

A brief description of the OPO processes based on the figure 5.1 is provided here after. The basic concept of an OPO is first to generate new frequencies (optical parametric generation - OPG) and second to amplify them (optical parametric amplification - OPA).

5.3.1 OPG - Optical Parametric Generation

The new frequency generation or optical parametric generation, is a nonlinear phenomenon based on the parametric mixing process or DFG (section 1.5). Experimentally, we observe that a higher energy photon gives rise to two new photons of lower energies (within the energy conservation rule). What is the trigger of this mechanism? Actually, a DFG process occurring between a pump photon and one from the quantum noise (called the "signal" photon) is the very cause of the phenomenon (as shown in the figure 5.2).

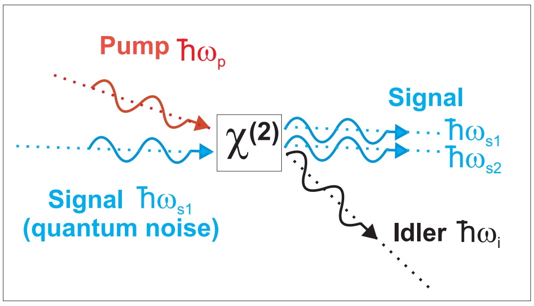

Figure 5.2: *Scheme of the DFG process between the pump beam and a signal photon from the quantum noise fluctuation. It results two coherent signal photons and an idler one at the crystal output, characterizing the new frequency generation (OPG process).*

Indeed, let us assume that along with the pump beam (energy $\hbar\omega_p$), a "signal" photon of $\hbar\omega_{s1}$ energy originating from the quantum noise fluctuation is also incident on the nonlinear crystal. Through a second-order DFG mechanism, this first $\hbar\omega_{s1}$ photon triggers the emission of a second "signal" photon having the same energy $\hbar\omega_{s2}$. This stimulated $\hbar\omega_{s2}$ photon has the same properties as the first one ($\hbar\omega_{s1}$) such as the phase, direction, wavelength. From the energy conservation law, an "idler" photon of $\hbar\omega_i$ energy is also emitted with $\hbar\omega_p - \hbar\omega_{s2} = \hbar\omega_i$. Therefore, from the pump beam photon, we obtain a pair of new photons having angular frequencies ω_s and ω_i.

However, some rules have to be obeyed concerning the allowed signal and idler photon frequencies and propagation directions. Indeed, every "signal" photon is not able to trigger the DFG process, the condition being the respect of the phase-matching between the involved photons. A matching of the respective photon phase is indeed required to obtain an optimal energy transfer between the different electric fields. The only way to satisfy this condition is through the use of nonlinear birefringent crystals. This kind of material has different refractive indices depending upon the polarization of the incident light. More specifically, for one polarization (let us say the s one), the refractive index is unique (isotropic sphere of index - ordinary index), while the other polarization (thus the p one) leads to a different refractive index depending on the photon propagation direction (anisotropic ellipsoid of index - extraordinary index). In this frame, let us assume that the pump photon is extraordinary polarized and that both signal and idler photons are ordinary polarized (e→oo - type I interaction). Any change in the pump beam incidence angle relatively to the crystal (θ) leads therefore to a change of the refractive index for this photon, and so in a change of wave vector:

$$|\overrightarrow{K_p}| = \frac{n_e(\omega_p, \theta)\,\omega_p}{c} . \tag{5.8}$$

To respect the phase-matching condition ($|\Delta K|=0$), we have:

$$|\overrightarrow{K}_p| = |\overrightarrow{K}_s + \overrightarrow{K}_i| \propto n_0(\omega_s)\,\omega_s + n_0(\omega_i)\,\omega_i . \tag{5.9}$$

The only way to satisfy this relationship is through a unique couple of ω_s and ω_i values. The energy/wavelength repartition between the signal and idler photons relies consequently exclusively upon the angle of propagation (θ) of the pump beam through the nonlinear crystal. The vectorial conservation of $\overrightarrow{K}_p = \overrightarrow{K}_s + \overrightarrow{K}_i$ has also to be respected, leading to defined directions of emission of both the idler and the signal photons. Finally, for each different θ angle of incidence of the pump beam relatively to the nonlinear crystal, a unique couple of idler and signal photon energies are allowed, both of them being emitted in a distinct and defined direction.

This reasoning is still valid for an other combination of polarization (e→oe - type II interaction). By convention, among the two new photons, the signal has the highest frequency, and the idler has the lowest one.

Experimentally speaking, the pump beam remains fixed while the crystal is mounted on a rotary plate. Through an appropriated calibration, an equivalence is obtained between angular rotary plate values and new photon wavelength emission. Notice that from the desired frequency range, crystal parameters such as the cut angle have to be determined beforehand in order to optimize the spectral emission window. A typical tuning curve is shown in figure 5.3. The θ angle is defined relatively to the optical axis (axis passing through both focus points of the index ellipsoid).

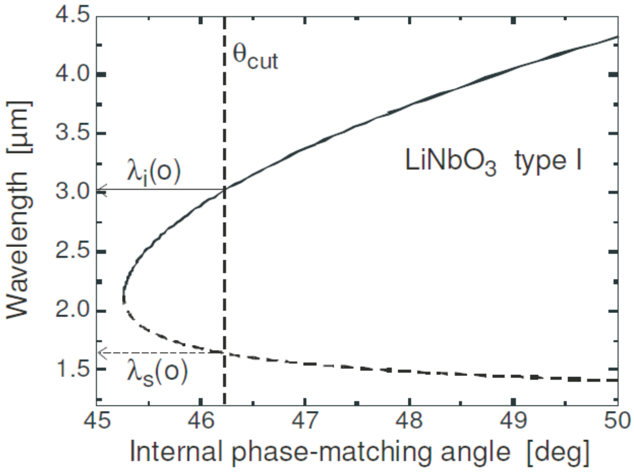

Figure 5.3: *Phase-matching curve for a LiNbO$_3$ crystal. Depending on the angular propagation of the incident beam relatively to the crystal optical axis, the repartition of energy (and thus of wavelength) between the idler and the signal changes.*

In order to extend the frequency range as wide as possible, two different crystals are used in the IR OPG/OPO. The first one is a LiNbO$_3$ crystal emitting in the 2.5-4 μm spectral window. The second one is a AgGaS$_2$ crystal generating 5-10 μm wavelengths (type II phase matching) or 3-10 μm (type I phase matching - less power). In the other hand, the visible OPG/OPO is based on a BBO crystal that generates wavelengths from 410 to 700 nm.

5.3.2 OPA - Optical Parametric Amplifier

The amplification step is easily fulfilled through the parametric mixing process (DFG, section 1.5). Let us start with the IR OPO. After the OPG process, the signal (highest frequency) is forced to oscillate inside a mirror cavity (see fig 5.1). Since the set up is in a synchronously pump configuration, the forced oscillating bunch of signal photons passes every time through the nonlinear crystal exactly at the same time as the next pump laser pulse (see figure 5.4, pump at 1 μm in the scheme).

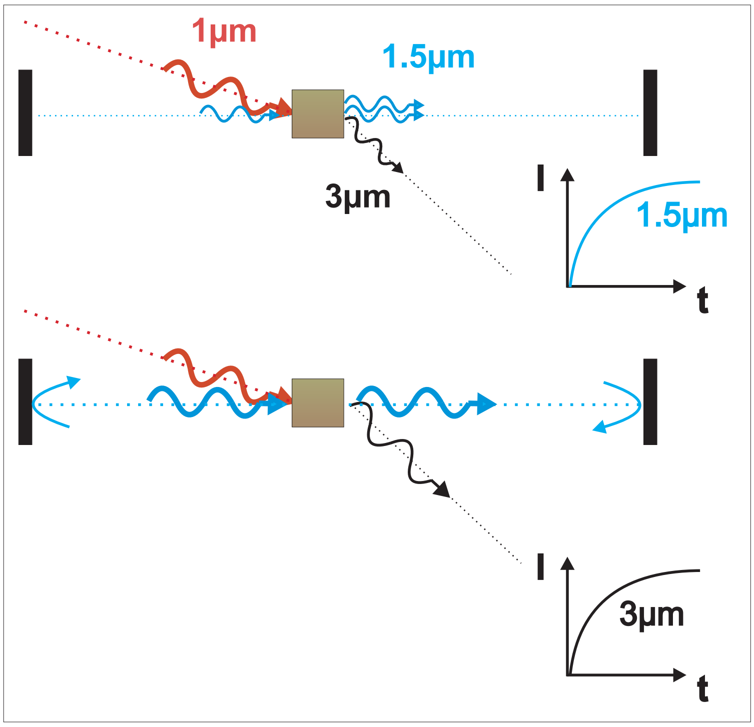

Figure 5.4: *Description scheme of the IR OPO functioning.*

The intensity of the signal increases therefore after each pump pulse pass through the crystal since more and more signal photons are duplicated (upper part in the scheme - the signal is shown at 1.5 μm). Along with this signal amplification mechanism (OPA), the DFG occurring within the crystal produces an increase of the idler beam power as well (lower part in the scheme - idler at 3 μm). Indeed, since both pump and signal beam powers are now important, a DFG operation between them leads to a massive generation of idler photons. Notice that this two step explanation is a pictorial description since the signal and idler power gains are fairly simultaneous.

The whole procedure is duplicated for the visible OPO. For this latter however, the used tuneable frequency beam is the inner cavity oscillating one. Concerning that point, the particular choice of which beam (signal or idler) is forced to oscillate, is based on the OPO performances. The oscillating photons having to realize a large number of round trips into the cavity, considerations about optical absorptions in the air and in the crystal as well as the mirror reflexion coefficient for the implicated frequency range, become critical in our case. The desired frequency window being the inner cavity one for the visible OPO case, a semi reflecting cavity mirror is used to extract a fraction of this oscillating signal power. In this configuration, the idler beam is not used.

The combination of those two OPOs leads to an IR and a visible frequency-tuneable laser. The mean powers of the emitted beams are around 20 to 30 mW.

5.3.3 Collecting the SFG signal from samples

As shown in the figure 5.1, both IR and visible beams are then focused on the sample interface with incident angles of 65° and 55° from the surface normal, respectively. While the IR beam frequency is scanned over the required spectral window, the visible beam wavelength is kept fixed (532 nm - SR-SFG). The IR, visible, and generated SFG polarizations may be chosen either s or p (or intermediate if needed by the use of appropriated optics). Finally, after spectral filtering by a home-made double monochromator, the SFG signal originating from the sample surface is monitored by an oscilloscope after a photomultiplier amplification. The required motors involved in all the frequency tunability sequence (crystals, mirrors...etc) as well as the monochromator frequency position, are all controled by a home-made Labview program in each step of the SFG spectrum acquisition. This spectrum plots the SFG intensity in function of the IR frequency (since a spectrum analysis relies on infrared vibrational mode expression through the nonlinear SFG intensity yield).

5.4 Probing the molecular organization/conformation → the alkyl chain example

Since second-order spectroscopies are surface sensitive for a wide number of experimental environments, they are mainly used to study and probe interfacial layers (either exposed or buried ones). In those interfacial locations, the presence of directional constraints may lead, through physico-chemical interactions, to a structured configuration of the involve molecules. This includes, for instance, self-assembling processes, Langmuir-Blodgett methods, and still others.

Therefore, besides the strict vibrational informations, a whole set of additional data, based on the increase or loss of structural order that may be undergone during a wide range of phenomena (such as molecular interactions and recognitions) are available. In this context, from its non centrosymmetry requirement to become active, the SFG turns to be a key technique to take advantage of those hidden structural informations.

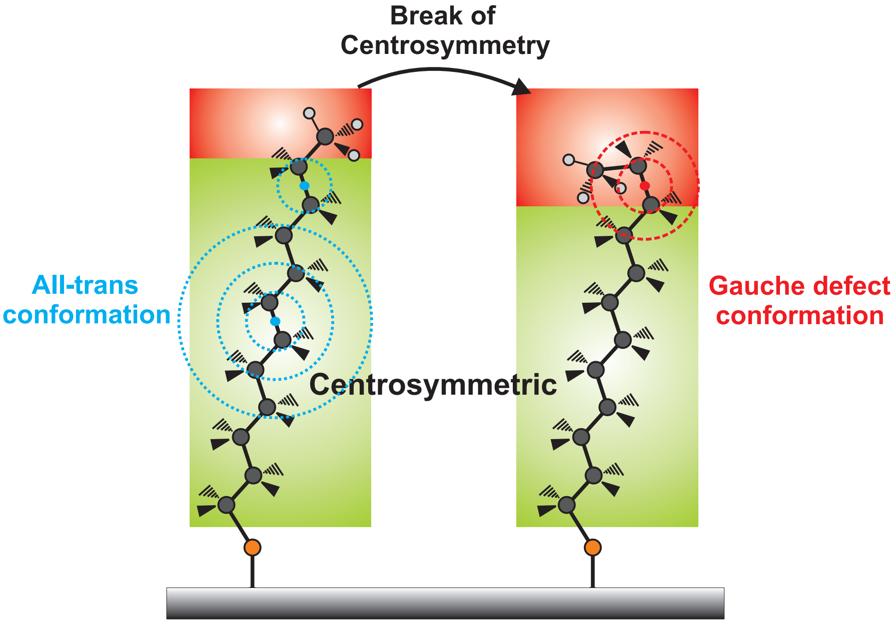

Figure 5.5: *Dodecanethiol molecule chemisorbed on a metal lattice through a thiol group. The presence of gauche defects into the methylene chain turns the molecule into a non centrosymmetric system. The more gauche defects there are, the more the methylene modes become SFG active.*

Indeed, certain chemical species such as methylene chains may be qualified as conformal sensors among more complex structures. The detail that makes them useful for such purposes is their centrosymmetry when they are perfectly organized in an all-trans conformation as shown in figure 5.5. In the right part of the figure, the green part displays a centrosymmetric methylene structure in its all-trans conformation, while the red part depicted a intrinsic non centrosymetric area owing to the methyl group. When a structural modification occurs, such as a gauche defect that could be localized anywhere within the alkyl chain (depicted here as the red additional part in the left side of the figure), the local centrosymmetry properties are broken. It results that, in case of such structural defects, those latter let appear a SFG vibrational component at the methylene frequencies. Notice however that for both structured or non strucured chain, the intrinsic methyl vibration is present because being always in a non centrosymmetric conformation. Finally, from the methylene mode intensities, a relative conformational quality of the chain structure may be deduced. Those considerations about order are important since the dynamics of interaction between different molecular species strongly relies on their structural configurations.

Now, let us see the interpretation of those effects in terms of SFG spectra. The figure 5.6 presents three spectra of alkyl chains linked to a metal substrate (platinum) through a thiol group (Dodecanethiol - DDT) and forming a self-assembled monolayer (SAM) on the surface. This well-known process leads to spontaneous molecular self-assembling on surfaces through van der Waals interactions within the covalently bounded alkyl chains.

The 3 different spectra (A, B and C) of the figure 5.6 are those of 3 different samples of DDT SAMs on Pt. Note that their are not attributed to particular experimental conditions, their are just presented to illustate the underlying conformational idea. Five distinct vibrational modes are observed. The two main ones around 2880 and 2966 cm^{-1} are attributed to the symmetric (v^+CH_3) and antisymmetric (v^-CH_3) stretching vibrations of the terminal methyl group of the chain, respectively. The peak located at 2940 cm^{-1} corresponds to the methyl Fermi resonance (Fr CH_3), while the last two modes around 2860 and 2915 cm^{-1} are attributed to the symmetric (v^+CH_2) and antisymmetric (v^-CH_2) stretching vibrations of the methylene groups. The noticeable point is the growth of both methylene vibrational components from spectrum A to C (left panel, open circles are experimental values; red curves are theoretical fits).

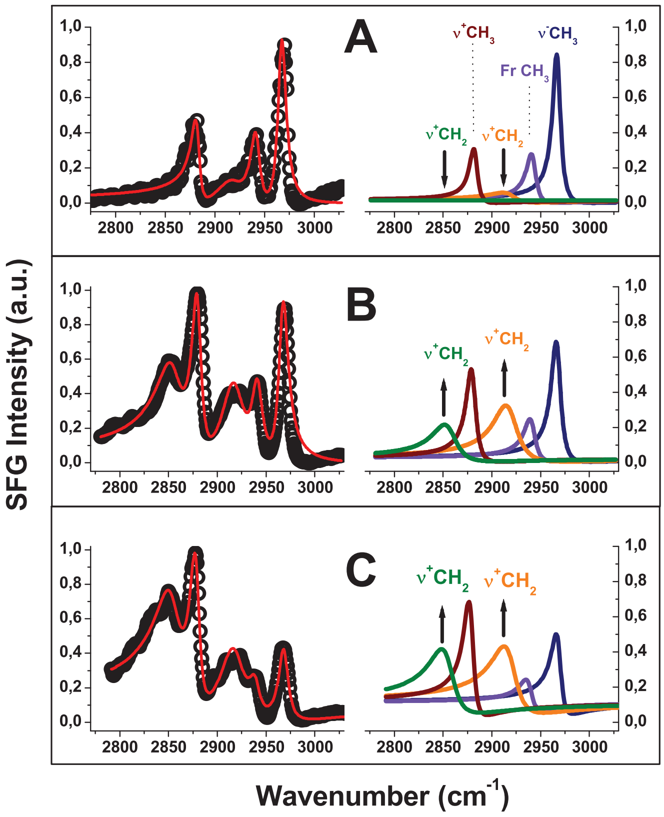

Figure 5.6: *SFG spectra of DDT SAMs on metal (Platinum) recorded in ppp polarization within the methyl-methylene stretching vibrational window.*

A deconvolution of each spectrum has been performed into a sum of individual lorentzian (shown on the right side; the sum of the 5 represented modes equals to the full fit shown as the red solid curve on the left side). This step may actually be subject to controversies. Indeed, from the complex nature of the electrical susceptibility, described in equation 5.7, many different combination of lorentzian curves can reproduce a given SFG spectrum, all of them having different parameters. It appears therefore to be nearly impossible to reliably attribute accurate mode intensities from this procedure. However, in order to simplify this brain teaser, we will adopt a unique phase $\psi_{R,q}$ for all q vibrational modes. Thus only a single phase remains $\psi = \psi_{NR} - \psi_R$, limiting drastically the allowed combinations. Experimentally, a Labview program has been developed to easily perform the fit (Fitomatic ®, Sartenaer Yannick). We observed that when taking only one phase and the same width for the different modes of a given chemical group, the accuracy on the spectrum deconvolution into individual lorentzian is acceptable. All further deconvolutions in this work are realized in this way.

From the figure 5.6, it appears obvious that both methylene (orange and green) modes undergo a significant intensity increase while considering the different samples. This is attributed to a break in the centrosymmetry owing to gauche defect appearance, and consequently to an increased disorder. This behaviour may be observed in case of alkyl chain molecules, any SAM structures being alkyl chain based molecules and for all other centrosymmetric molecular structures. Experimentally speaking, the methylene mode activities are used all along this thesis to qualify the organization of model molecular layers.

Notice that besides highly organized films, a fully disordered layer such as randomly packed proteins on a surface will be centrosymmetric in average, thus SFG silent. However, if a specific recognition process occurs, for example between the in solution proteins (the targets) and a particular surface-linked molecules (the probes, it is the general concept of a biosensor devices such as DNA chips), directional interactions may be induced, leading to an organization of the target molecules but also to a possible reorganization of the probes. The molecules that are no longer disordered, are no longer either centrosymmetric, and thus become SFG active. This symmetry sensitivity turns the SFG into a more complex tool than classical FT-IR spectroscopy (for which the distinction between surface packed proteins and selectively recognized ones are less obvious) for biosensor applications.

5.5 Probing the molecular orientation → the alkyl chain example

This section is dedicated to the absolute molecular orientation retrieval from SFG spectra. This step brings together many concepts introduced in chapters 1, 2 and 3.

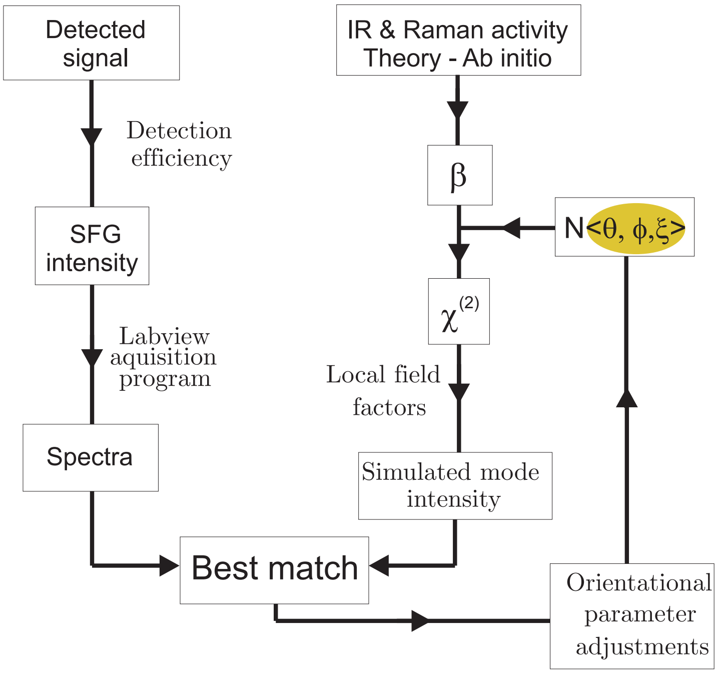

Figure 5.7: *Organization chart describing the procedure of orientational retrievals. The orientation determination requires measuring the SFG signature, computing both IR and Raman activity derivatives, and calculating local field factors (such as Fresnel ones, as well as beam and polarization projection considerations). Finally, through a best theoretical simulation of experimental curves, molecular orientations* (θ, ϕ, ξ) *can be deduced.*

Figure 5.7 shows a scheme of the general principle. Notice that we do not consider any further assumption over a potential β_{ijk} "dominant" term as done earlier for SHG spectroscopy in chapter 4.

The underlying idea is that the SFG spectrum carries the $\chi^{(2)}$ tensor properties straight through the macroscopic polarization response of the surface. Each time a molecular vibrational mode is resonant with the IR source, the $\chi^{(2)}$ is enhanced (but only if this mode is both IR and Raman active). Besides some parameters that have to be accurately considered (Fresnel factors, dielectric constants, propagation angles, beam polarizations, see chapters 1 & 2), the link between the measured quantity, which is a macroscopic response of the interface, and the single molecular hyperpolarizability, relies on a referential change and on one average over a large number of individual molecule. To perform this switch from the molecular to the laboratory frame, three successive rotations are needed (Euler angles, θ,

ϕ, ξ). Consequently, for any defined molecular vibration, a modification of orientation (through θ, ϕ, ξ) leads to a different macroscopic measurement of $\chi^{(2)}$. However, since the β_{ijk} components may be obtained from theoretical calculations of both IR and Raman activities, only defined (θ, ϕ, ξ) angles allows to match the experimentally measured $\chi^{(2)}$ through SFG spectra. As a matter of course, the more different components of the $\chi^{(2)}$ tensors are probed (4 max) through experiment, the more unvocal become the angular parameters, the goal being well to obtain one sole set of (θ, ϕ, ξ) valid angle. In order to multiply the cross angular determination, different polarization sets are used, knowing that we get the following combinations of probes: ppp → zzz, zxx, xxz and xzx ; ssp → xxz ; sps → xzx ; pss → zxx. Besides polarizations, it is also successful to simulate different mode symmetry (i.e symmetric and antisymmetric) since it allows relying on different Raman tensor and infrared vector derivatives. Finally, coupling both approaches, that is simulating different mode activities for multiple polarization sets, constitutes the more reliable method. This is even more relevant to do so for metallic surface since only the ppp and ssp combinations lead to experimental results (because of the IR screening effect due to the metal electron in s polarization). In that case, the ppp polarization alone is not sufficient to univocally define angles, but both the ppp and ssp sets turn out to be enough.

In the simulations, the IR dipole moment and Raman polarizability derivatives were obtained at the density functional theory (DFT) level of approximation using the GAUSSIAN 03 program [Gaussian and co authors, 2004]. The B3LYP exchange-correlation functional and the 6-311++ G(d,p) basis set were employed on the basis of their good performance [Guthmuller et al., 2009]. The ground state geometry of the molecule was optimized under the condition that the residual forces are smaller than 10^{-5} a.u. Then, the harmonic vibrational frequencies and normal coordinates were determined analytically at the same level of theory. The derivatives of the dipole moment vector with respect to the normal coordinates were evaluated at the ground state geometry from the first-order nuclear coordinate derivatives of the Kohn-Sham orbitals. The Raman tensors were computed using a two-point numerical differentiation procedure, where the dynamic polarizability tensor at 532 nm was calculated for distorted structures, resulting from the addition or subtraction of a finite displacement of the normal coordinate to the equilibrium geometry. Though recent progresses have been achieved [Quinet et al., 2004], Fermi resonance signatures were not modelized since they are associated with anharmonicity effects, requiring much heavier computational treatments.

The calculations of the IR and Raman activities have been performed on different alkane molecules with carbon chain lengths included between 2 and 12 units. The carbon chains, except one terminal methyl group, have been considered as "frozen", which means that only the "unfrozen" methyl group was allowed to vibrate. This was achieved by allocating a very high mass to every single atom excluding the free methyl group. Practicaly, no or only very small changes in the activities was observed when considering longer chains than octane. The value of tensor used in this work were the one of the octane molecule and are assumed to be valid for both dodecane and hexadecane molecule. To verify the validity of this model for real situations where the alkyl chain is allowed to vibrate, calculations have been performed on alkane molecules with only one last methyl "frozen". Not many differences were observed in the activities. However, gauche defect impacts have not been investigated.

Similar *ab initio* and DFT procedures and levels of approximations were used recently and have demonstrated a good reliability for predicting a broad range of molecular vibrational signatures, including vibrational SFG [Guthmuller and Champagne, 2007] [Mani et al., 2004] [Lamparska et al., 2006] [Rappoport and Furche, 2007] [Halls and Schlegel, 1998] [Halls and Schlegel, 1999]. Note however that simulation schemes based on molecular mechanics [Morita and Ishiyama, 2008] and discrete dipole lattice sums [Zheng et al., 2008] have recently been developed and have also turned out to be very useful to investigate the SFG signatures of various interfaces, including liquid/air ones.

A simulation program (developped in our laboratory), allows to reproduce SFG spectra from IR and Raman activities. For each mode predicted by theoretical calculations, an arbitrary unit intensity is established under the form of a Lorentzian curve. This intensity depends upon the width of the vibration, the dielectric constants of the involved media (usually a three layer configuration: substrate, film, air-water), and Fresnel factors as well as incident angles (all being fixed amounts for a given spectrum), but above everything else, it relies on the orientational parameters of the molecule. Therefore, by changing the values of θ, ϕ and ξ, it becomes possible to adjust the simulation to the experiment.

However, since we handle arbitrary unit (a.u.) intensities, a ratio between two Lorentzian is required (at least). The usual way is to compare two different molecular modes within the same spectrum, both of their intensities relying on the same and unique molecular orientation (through $\chi^{(2)}$). To go further and to avoid multi-angle solutions, this can be done for different polarization configurations of the beams. Finally, it is also possible to compare the relative SFG intensities of one single mode between different polarization configurations. This last step is however fussy when performed onto metals because of the important screening effect in s-polarization. The Fresnel factors are indeed highly different between the s and p polarizations (especially for the IR beam) as well as the SFG intensity. In those case where the experimental intensities are strongly different between two spectra, the intensity comparison leads to a large factor, which leads to less negligible error bar, involving a wider panel of orientations.

In this section, we used the ratio between two vibrational modes (methyl) included in the same spectrum, this for two polarization combinations (ppp and ssp), as shown in the figure 5.8.

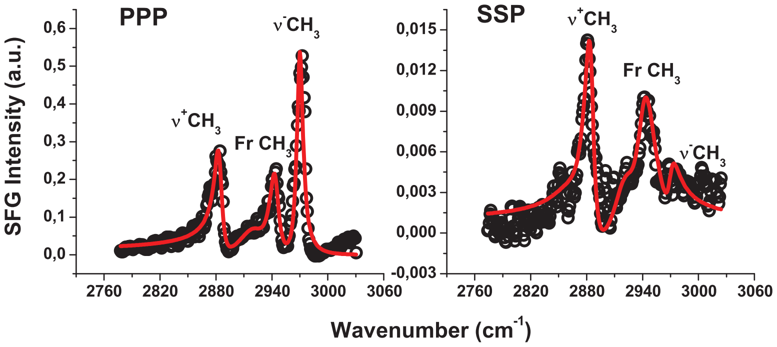

Figure 5.8: ppp and ssp polarized SFG spectra of a DDT SAM on Pt substrate in the methyl-methylene spectral window. Both spectra are fitted by a sum of 5 Lorentzian (red curves).

The spectra are the ones of a DDT SAM on Pt substrate in the methyl-methylene spectral range. Remember that only 4 polarization sets are allowed from the azimuthal isotropy (see chapter 2), and practically, only two on metal (ppp and ssp) as performed here. In the table 5.1 are shown the different parameters used to obtain a best Lorentzian fit to the spectra of the figure 5.8 (red curves).

		ppp polarization fit		ssp polarization fit	
Modes	Γ_q(cm^{-1})	ν (cm^{-1})	$\lvert A_q\rvert/\lvert A_{NR}\rvert$	ν (cm^{-1})	$\lvert A_q\rvert/\lvert A_{NR}\rvert$
$\nu^- CH_3$	5.0	2969.9	29.0	2970.0	6.0
$Fr\ CH_3$	7.0	2943.5	23.5	2941.5	37.0
$\nu^- CH_2$	15.0	2922.0	20.3	2922.0	28.0
$\nu^+ CH_3$	5.0	2884.0	22.1	2885.0	23.0
$\nu^+ CH_2$	15.0	2861.5	0.0	2861.6	5.0
$\lvert A_{NR}\rvert$	-	0.30		0.05	
ϕ (deg)	-	220°		90°	

***Table 5.1:** Parameters used to get a best fit to both the SFG spectra in ssp and ppp polarization configurations. The parameters are those of the Lorentzian modes. The mode intensities are normalized to the NR one*

The calculation of both IR and Raman activities has been realized (up to now) on the more stable conformational configuration of the molecule (energy minimization). Consequently, the octane chain considered in the theoretical procedure is in its all-trans configuration, and only the free methyl group is SFG active. All the simulations are therefore run over the methyl symmetric and asymmetric modes only. As aforementioned, the Fermi resonance is not taken into account, what could lead to an error on the orientational determination. Indeed, this latter vibration is originating from a resonance between the methyl symmetric stretching mode and an overtone (second harmonic) of a methyl vibrational mode located around 1465 cm^{-1}. To happen, the process need to take some energy from the ($\nu^+ CH_3$). Therefore, ignoring the Fermi resonance lead to an underestimation of the ($\nu^+ CH_3$) vibrational mode [Kondratyuk, 2005]. The resulting error is estimated to few degrees in the molecular orientation. Finally, the parameters needed to run the simulations as the peak frequencies, widths, and the non-resonant contribution, are all extracted from the Lorentzian fit presented in the figure 5.8 (red curves) and listed in the table 5.1. Actually, the orientation is the only parameter that remains to be adjusted, all other variables being fixed through the best Lorentzian fit procedure to the experimental curves.

Since the surface isotropy is assumed, the ξ angle is averaged from 0 to 2π. This is justified since the macroscopic probed area over the Pt(111) single crystal surface integrates a large number of microscopic domains, each of them having a distinct azimuthal angle resulting from the self-assembling process. Hence, only the tilt θ and twist ϕ angles have still to be adjusted in order to match the experimental curves (performed directly on the full spectrum). The simulations run over the DDT spectra are shown in figure 5.9. The optimal theoretical adjustments are presented in the upper two main panels of the figure (solid lines) for both ppp and ssp polarizations. The orientational values obtained are 48° for the tilt angle θ and 0° for the twist angle ϕ. These values lead to a methylene chain orientation of 13° with respect to the surface normal, in keeping with values reported in previous studies for HDT SAMs on Pt and ranging from 5° to 20° [Petrovykh et al., 2006] [Noguchi et al., 2005] [Li et al., 2003] [Lee et al., 2006] [Alexiadis et al., 2007].

To perform this deduction, we firstly have to notice that reasonably, the twist angle ϕ has to be 0° (as well as multiples of 120° since the methyl group is of C_{3V} symmetry) in order to reach the energetically most stable conformation and to keep the all-trans conformation. Thus, all intermediate values of twist angle (such as 60°) should not be appropriate. We therefore plot simulated curves for a few values of θ (20°, 40°, 60° and 80°, between 0 and 90° to keep the right physical meaning) for both 0° and 60° ϕ twist angle. Those 8 simulated curves are presented in the middle part of the figure 5.9. The NR phase and intensity effects are taken into account, even if this latter (intensity) has been adjusted from one simulation to another to keep a same NR amplitude relatively to the methyl mode one.

In the ppp polarization set, for $\phi = 60°$, no θ value allows to match the experimental SFG spectrum. On the other hand, while $\phi = 0°$, the angle value $\theta = 48°$ enables to match the same spectrum. Furthermore, this couple of angles appears to be suitable as well for the ssp configuration (although the curves matching is less obvious because of the smaller intensity and larger noise to signal ratio). Beside the methyl group orientation, the simulation may take into account the non resonant intensity and phase as mentioned in equation 5.3. The resulting $\chi^{(2)}_{NR}$ contains the molecular non resonant terms (mentioned in chapter 3) as well as the substrate ones. It may be considered as a constant over the probed spectral range (since the transitions corresponding to the NR elements are assumed to be far from the used frequencies, hence the "non-resonant" expression).

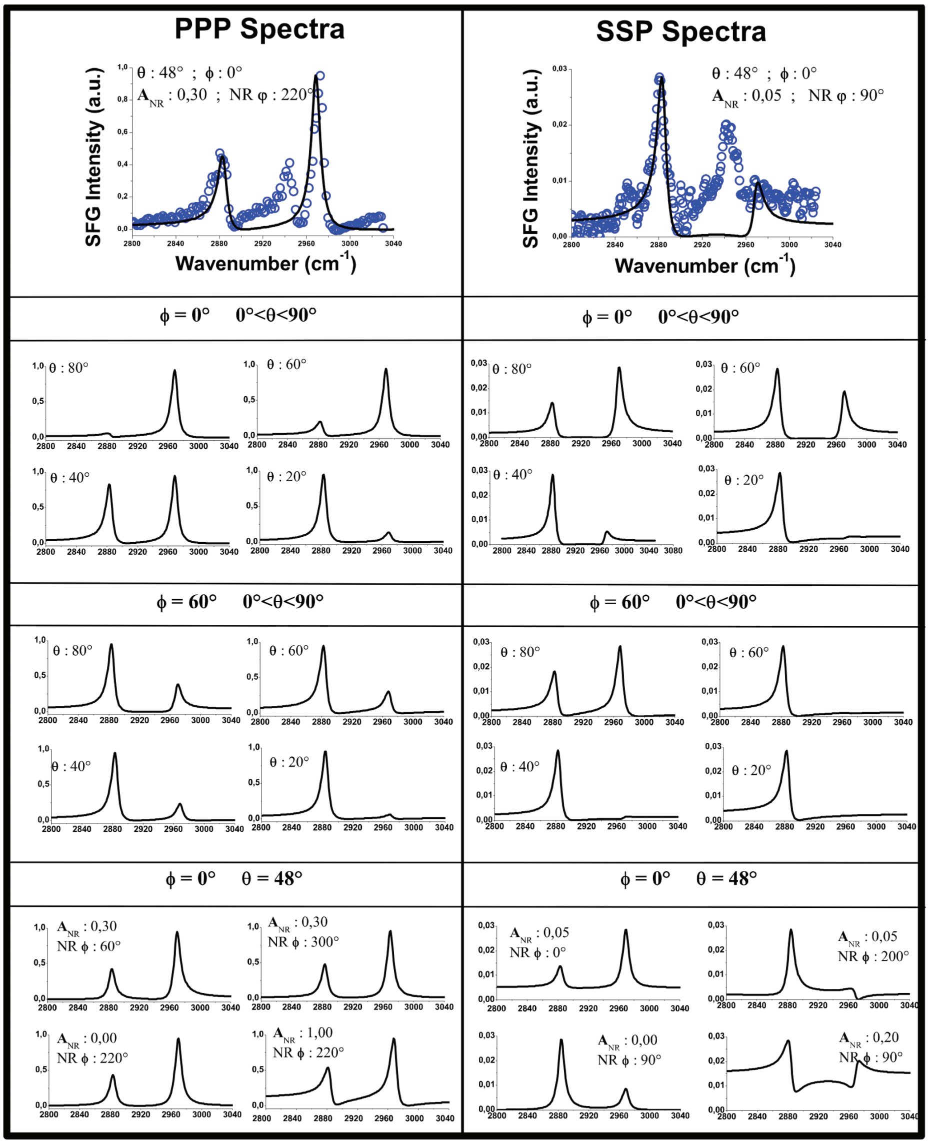

__Figure 5.9:__ Theoretical simulations (solid lines) of the methyl SFG modes (open circles) from DDT SAMs. Optimal parameters have been found (upper two main panels) for ppp and ssp polarizations, whereas both θ and ϕ angles have been tuned one by one independently (lower panels) to show the sensitivity of the procedure. In the first two stages, θ takes different values (20° - 80°) for two values of ϕ (energetically stable - 0° ; or unstable - 60°). Finally, in the lowest stage, the NR background phase and amplitude effects are shown. The methyl tilt angle is 48° corresponding to an alkane chain tilt angle of 13°.

The lowest part of the figure 5.9 is dedicated to show those NR phase and amplitude effects, the chosen NR parameters being those extracted from the best fit by a Lorentzian and presented in table 5.1.

Note that since the global NR amplitude is low, both the platinum NR contribution and the molecular one are weak (see the NR terms in chapter 3). It is important to underline that strong NR phase effects may entirely change the aspect of a spectrum, or even make disappear a peak. The platinum is however a suitable material in SFG since its NR effect is weak.

Finally, the absolute error that could be made on the orientational retrieval method is estimated to be included in the 5°-10° range. It originates from parameters such as the interfacial dielectric constant (1.4) [Zhuang et al., 1999] [Wang et al., 2001], the *ab initio* determination of IR and Raman activities, the methylene activity in experimental spectrum, the neglecting of Fermi resonance, or/and the non-negligible signal-to-noise ratio in the ssp spectrum, as well as the mode width . . ..

5.6 Resume

This chapter has been dedicated to overview the working principles and the potentialities of the sum-frequency generation spectroscopy. Besides the surface sensitivity properties, conditions on the SFG have been detailled through laser source requirements. Those latter have been introduced from nonlinear bulk phenomena occurring in OPO devices. The new frequency generation is realized in the OPG process after what an amplification of those new photons is achieved by an OPA mechanism. The SFG generation and detection from the sample have been briefly described. Spectra analysis based on specific centrosymmetric chemical groups (methylene chains, alkanethiol) have been performed to provide typical SAMs conformational informations. Additionally, the method to retrieve the molecular orientation has been presented and applied to those alkyl chains, leading to a complete parametrization of the film conformation and disposition. The alkyl chains own a 13° tilt angle and a 0° twist angle while chemisorbed on Pt through SAM process.

5.7 Bibliography

[Alexiadis et al., 2007] Alexiadis, O., Harmandaris, V. A., Mavrantzas, V. G., and Delle Site, L. (2007). Atomistic simulation of alkanethiol self-assembled monolayers on different metal surfaces via a quantum, first-principles parametrization of the sulfur-metal interaction. J. Phys. Chem. C, 111(17):6380–6391.

[Gaussian and co authors, 2004] Gaussian, J. A. and co authors (2004.). Gaussian 03, revision c.02. Inc., Wallingford CT.

[Guthmuller et al., 2009] Guthmuller, J., Cecchet, F., Lis, D., Caudano, Y., Mani, A. A., Thiry, P. A., Peremans, A., and Champagne, B. (2009). Theoretical simulation of vibrational sum-frequency generation spectra from density functional theory: Application to p-nitrothiophenol and 2,4-dinitroaniline. Chemphyschem, 10(12):2132–2142.

[Guthmuller and Champagne, 2007] Guthmuller, J. and Champagne, B. (2007). Time dependent density functional theory investigation of the resonance raman properties of the julolidinemalononitrile push-pull chromophore in various solvents. J. Chem. Phys., 127(16):164507.

[Halls and Schlegel, 1999] Halls, M. and Schlegel, H. (1999). Comparison study of the prediction of raman intensities using electronic structure methods. J. Chem. Phys., 111:8819–8824.

[Halls and Schlegel, 1998] Halls, M. D. and Schlegel, H. (1998). Comparison of the performance of local, gradient-corrected, and hybrid density functional models in predicting infrared intensities. J. Chem. Phys., 109:10587–10593.

[Kondratyuk, 2005] Kondratyuk, P. (2005). Analytical formulas for fermi resonance interactions in continuous distributions of states. Spectrochimica Acta Part a-Molecular and Biomolecular Spectroscopy, 61(4):589–593.

[Lamparska et al., 2006] Lamparska, E., Liegeois, V., Quinet, O., and Champagne, B. (2006). Theoretical determination of the vibrational raman optical activity signatures of helical polypropylene chains. Chem. Phys. Chem, 7:2366–2376.

[Lee et al., 2006] Lee, S., Park, J., Ragan, R., Kim, S., Lee, Z., Lim, D. K., Ohlberg, D. A. A., and Williams, R. S. (2006). Self-assembled monolayers on pt(111): Molecular packing structure and strain effects observed by scanning tunneling microscopy. J. Am. Chem. Soc., 128(17):5745–5750.

[Li et al., 2003] Li, Z. Y., Chang, S. C., and Williams, R. S. (2003). Self-assembly of alkanethiol molecules onto platinum and platinum oxide surfaces. Langmuir, 19(17):6744–6749.

[Mani, 2004] Mani, A. (2004). Development of a sum-frequency generation spectrometer. Thesis.

[Mani et al., 2001] Mani, A. A., Dreesen, L., Hollander, P., Humbert, C., Caudano, Y., Thiry, P. A., and Peremans, A. (2001). Pumping picosecond optical parametric oscillators by a pulsed nd : Yag laser mode locked using a nonlinear mirror. Applied Physics Letters, 79(13):1945–1947.

[Mani et al., 2002] Mani, A. A., Dreesen, L., Humbert, C., Hollander, P., Caudano, Y., Thiry, P. A., and Peremans, A. (2002). Development of a two-color picosecond optical parametric oscillator, pumped by a nd : Yag laser mode locked using a nonlinear mirror, for doubly-resonant sum frequency generation spectroscopy. Surface Science, 502:261–267.

[Mani et al., 2004] Mani, A. A., Schultz, Z. D., Champagne, B., Humbert, C., Dreesen, L., Gewirth, A. A., White, J. O., Thiry, P. A., Peremans, A., and Caudano, Y. (2004). Molecule orientation in self-assembled monolayers determined by infrared-visible sum-frequency generation spectroscopy. Appl. Surf. Sci., 237:444–449.

[Morita and Ishiyama, 2008] Morita, A. and Ishiyama, T. (2008). Recent progress in theoretical analysis of vibrational sum frequency generation spectroscopy. Phys. Chem. Chem. Phys., 10:5801.

[Noguchi et al., 2005] Noguchi, H., Ito, M., and Uosaki, K. (2005). Molecular orientation of self-assembled monolayer of octadecanethiol on platinum surface studied by femtosecond broad-bandwidth sum frequency generation spectroscopy. Chem. Lett., 34(7):950–951.

[Petrovykh et al., 2006] Petrovykh, D. Y., Kimura-Suda, H., Opdahl, A., Richter, L. J., Tarlov, M. J., and Whitman, L. J. (2006). Alkanethiols on platinum: Multicomponent self-assembled monolayers. Langmuir, 22(6):2578–2587.

[Quinet et al., 2004] Quinet, O., Champagne, B., and Rodriguez, V. (2004). Polarization effects on the hyper-raman spectra of carbon tetrachloride: A joint experimental-theoretical study. J. Chem. Phys., 121:4705–4710.

[Rappoport and Furche, 2007] Rappoport, D. and Furche, F. (2007). Lagrangian approach to molecular vibrational raman intensities using time-dependent hybrid density functional theory. J. Chem. Phys., 126:201104.

[Zheng et al., 2008] Zheng, D. S., Wang, Y., Liu, A. A., and Wang, H. F. (2008). Microscopic molecular optics theory of surface second harmonic generation and sum-frequency generation spectroscopy based on the discrete dipole lattice model. Int. Rev. Phys. Chem., 27(4):629–664.

[Zhu et al., 1987] Zhu, X. D., Suhr, H., and Shen, Y. R. (1987). Surface vibrational spectroscopy by infrared-visible sum frequency generation. Physical Review B, 35(6):3047–3050.

Chapter 6

The micro-contact printing method

6.1 Introduction

Thin layer depositions onto surfaces are widely required for numerous applications in various domains, from industrial (electronic devices, optical layers, protecting layers, decoration purposes...) to biomedical (biochemical layers for compatibility, sensoring...), passing through material sciences (wetting, etching, self-cleaning properties). Among all of them, specific fields related to highly packed and organized monolayers are strongly used in biochemical science engineering. The production of such molecular films on surfaces is commonly achieved by several methods such as self-assembled monolayer, vapour deposition, Langmuir-Blodgett, or micro-contact printing (μcp). This chapter is dedicated to the study of this latter technique because of its multi abilities. It is indeed a cost less technique able to form a self-assembled molecular structure within very short time and owning simultaneously micrometric patterns. After a brief review on how to perform microcontact printing, the importance of the involved parameters is described. Among them, the print duration is more deeply investigated to find the limitation of the methods to form organized layer within very brief time. To do so, the surface specific SFG spectroscopy and its ability to track conformational defects and to deduce the molecular orientation is used. Layers produced by the micro-contact printing method over various print durations are compared with those obtained by the classical immersion SAM process. This enables to identify a minimal print duration to obtain a well organized monolayer onto solid substrates. Finally, the compatibility of the micro-contact printing method with different molecular species is discussed.

6.2 The micro-contact printing

A graphical flowchart of the method is depicted in the figure 6.1. The micro-contact printing method relies on the use of a silicone stamp to transfer the molecule from the liquid solution to the solid substrate. The stamp is made up of Sylgard-184 poly(dimethyl-siloxane) (PDMS - Dow Corning). This silicone polymer could have more than 1000 silicon atoms by chain, each of them being linked to apolar methyl groups responsible for the silicone poor reactivity. The liquid polymer mixture is allowed to degas in a vacuum desiccator (in order to remove trapped air bubbles), after what it is baked in the oven for 4h at 70°C. The curing step defining the solid shape of the stamp, the liquid silicone is beforehand spread either on a flat or a patterned solid wafer. Note that to turn the solid stamp fully antisticking, one drop of fluorosilane ((tridecafluoro-1,1,2,2-tetrahydrooctyl)trichlorosilane, 97%, ABCR) is added to the liquid silicone before the curing process.

The flat master is a regular silicon wafer (Si(100)), while the patterned one is made by electron beam lithography (Mapper Lithography, Delft, the Netherlands). The patterns are 10 μm and 100 μm large stripes and squares as shown in panels A & B of the figure 6.1. Those images, realized by scanning electron microscopy (SEM), show with a good resolution the high accuracy of the lithography step (the squares in the panel A are 10 μm in size). Next while baked, the solid stamp is carefully separated from the wafer to which it does not stick, thanks to the fluorosilane, and cut in 5×5 mm^2 squares. The stamp pieces are then cleaned with hexane ($\geq$ 99%, Sigma-Aldrich) and absolute ethanol ($\geq$ 99,8%, Sigma-Aldrich). Prior usage, each stamp is again shortly rinsed under pure water (bidistilled water, resistivity $\geq$ 18,4 MΩ cm) and dried under a stream of nitrogen (N_2). The panels C & D show the as produced stamps imaged by optical microscopy.

Once the stamps are obtained, the formation of molecular layers on solid substrates may be initiated. As depicted in the panel E of the figure 6.1, a few drops of the "ink" solution are poured onto the stamp. After one minute of inking, the stamp surface is dried under a nitrogen flow. Strictly speaking, the printing process consists of pressing the stamp on the substrate.

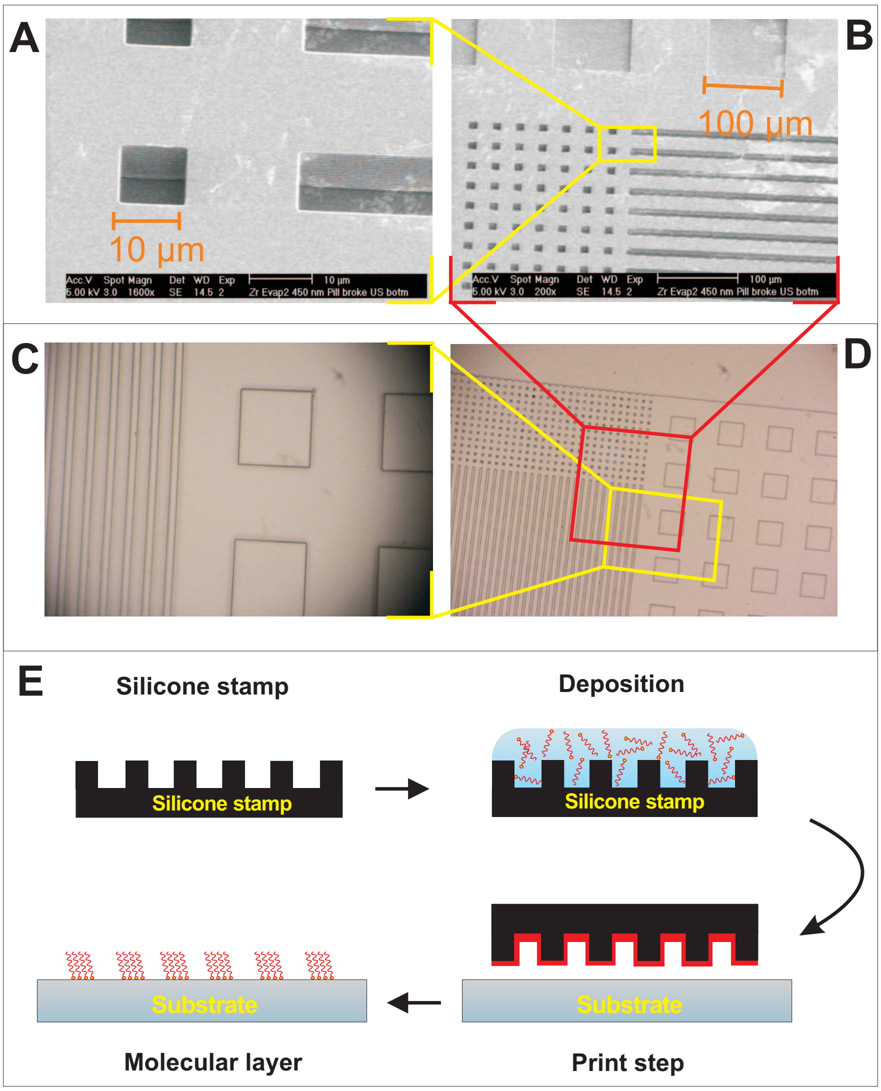

Figure 6.1: *Representation of the different μcp steps involved in the realization of a molecular monolayer. A and B, SEM images of the silicon wafer; C and D, optical microscopy images of the used silicone stamp; E, molecular film production steps.*

It is performed with a homemade mechanical press based on a tubular solenoid piston mechanism. The print duration, usually shorter than a minute, is controlled by a millisecond resolution timer (if such accuracy is needed) and verified by an electrical signal recorded at an oscilloscope, while the pressure is determined by the applied weight on the stamp (2.5 kg/cm^2 in this experiment). Once the printing step is achieved, the substrate is gently rinsed in a solvent and dried with N_2 before being immediately analyzed by SFG spectroscopy. From the experiments, it results that the formed molecular monolayer is well organized, with conformation quality comparable to self-assembling mechanism, even for as short time duration as seconds while the classical self-assembling method realized by immersion require hours. Furthermore, by patterning the stamp, the μcp technique enables the direct formation of shaped molecular monolayers with micrometre resolution, what is not directly achievable with the conventional immersion SAM process.

Since μcp is simultaneously dealing with several state-of-the-art properties, that is firstly the formation of highly organized monolayers, secondly, very fast dynamics of film formation, and thirdly, the high spatial resolution of the patterning ability, it is critical to define their mutual influences and find the best parameter set allowing to optimize each of them. In this context, the SFG spectroscopy is used to characterize the layer conformation quality while varying the two remaining properties (time and patterns).

6.3 The classical self-assembled monolayer

Let us remind the reader how to form a layer by self-assembly process. Once the substrate is cleaned, this latter is immersed into the molecular solution (usually of 1 mM concentration, based on regular solvent such as ethanol) for a duration of 24h [Petrovykh et al., 2006]. The construction of the monolayer is initiated by a chemical group which forms a covalent bond with the substarte (such as thiol for metallic sample). Along with the chemical binding, van der Waals interactions take place between the densely packed molecules and induce them to organize respectively to each other.

Once the immersion time is elapsed, the substrate is removed from the solution, thoroughly rinsed with the solvent and then dried under a N_2 flow. The molecular film quality achieved by this method is very high for little investment (cost, material) excepted for the duration (24h) [Ulman, 1996].

6.4 Substrates and molecules

In order to provide a strict comparison between the SAM prepared by immersion and by μcp method, the same molecule and substrate are used. The layers resulting from both methods are constructed on metallic substrates through thiol functional groups, forming covalent bonds. Metallic interfaces are indeed interesting in bio-device fields for associated applied-potential applications.

The substrate used for this experiment is a Pt(111) single crystal. Although gold represents a more regular substrate in the SAM domain, other metals such as platinum have recently been studied with various techniques [Sartenaer et al., 2007] [Petrovykh et al., 2006] [Dreesen et al., 2002] [Lee et al., 2006] [Li et al., 2003]. This preference for Au owes to the fact that Pt is subject to air contamination through oxidation while Au remains rather unchanged [Lang et al., 1998] [Lee et al., 2006] [Li et al., 2003]. This high initial amount of oxygen leads irremediably to a smaller density of thiols on the surface and has been proved to slow down the rate of thiol binding to the metal lattice [Lang et al., 1998]. Nevertheless, it is known that thiols clean up oxygen from the surface [Laiho and Leiro, 2006] and allow long alkyl chains to organize through van der Waals interactions into self-assembled structures. The use of Pt to evaluate the ability of the μcp technique to form well ordered molecular layers represent therefore the least favourable conditions regarding other substrates such as Au or Ag. The μcp method applied to Pt single crystal provides thus the minimal expected layer conformational quality regarding other substrates.

Besides this, Pt is very convenient for SFG spectroscopy owing to its lack of optical non resonant background activity. Regarding its preparation, the substrate is first manually polished (DP-paste 1-1/4 μm, Struers), then chemically etched in a piranha solution, and finally flame annealed for crystalline atomic reconstruction according to Clavilier's procedure [Clavilier et al., 1980].

The molecule solutions used in this work are typical alkyl chains with a thiol end group, namely dodecanethiol (DDT, $\geq$ 98%, Fluka) and hexadecanethiol (HDT, $\geq$ 95%, Sigma-Aldrich). The usual solution concentration, although having to be adjusted for specific purposes, is generally higher for μcp applications than for immersion SAM processes. The most suitable concentration to use for μcp is determined here after, based on SFG spectroscopy results.

6.5 μcp concentration, pressure and duration

6.5.1 Solution concentration

This parameter is with no doubt important in the layer formation mechanism during the printing step. Its effects are depicted through SFG spectra presented in the figure 6.2, for which the concentration is varied over nearly three orders of magnitude (0.1 to 50 mM) while keeping a constant print duration (60 s) and applied pressure (25 N/cm^2).

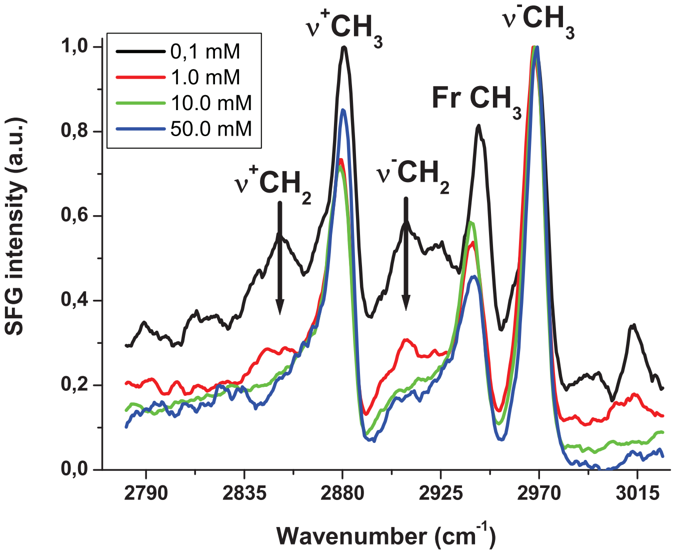

Figure 6.2: *SFG spectra of DDT on Pt with variable solution concentrations. The applied pressure is 25 N/cm^2, while the printing duration is 60 s.*

An effective improvement in the molecular organization regarding the solution concentration is observed through a decrease of both methylene modes. This is attributed to the fact that a lower molecular concentration of the solution leads to a lower amount of molecules remaining on the stamp after its drying under N_2. Consequently, for the same print duration, applied pressure, and laser conditions, a lower amount of molecules is transferred to the Pt substrate. Under a certain concentration threshold, this results in a non saturated surface of bounded molecules, which leads to weaker van der Waals interactions among the alkyl chains and thus to a less ordered molecular film. Within our experimental conditions (mechanical properties of the stamp, nature of the solvent, molar mass of the used molecule, print duration and applied pressure), this minimum concentration threshold is located around 10 mM as suggested in the SFG spectra of the figure 6.2.

For concentrations higher the 10 mM, only very little differences are observed in the SFG spectra (actually, pure liquid DDT ink can even be used but the stamp becomes much strongly swollen than with the ethanol based solution). A concentration of 50 mM for alkanethiol solutions is adopted in this work, and turns out to be appropriate for a wide range of print durations.

6.5.2 Pressure

The applied pressure to the stamp during the printing step does not appear to be a critical factor. Indeed, even if an increase of the signal intensity is observed, this latter is applies to every vibrational modes independently. However, because a weak mode such as the methylene will improve a higher relative intensity increase than a strong mode such as the methyl, a too large value of pressure turns out to degrade the layer conformation since the methylene activity becomes more and more imporant proportionally to the methyl one [Bohm et al., 1999]. During this work, a pressure of 25 N/cm^2 is chosen.

6.5.3 Duration

This factor appears to be the most interesting and challenging for us, as mentioned previously. Indeed, besides the fact that the μcp method is able to produce SAMs much faster than the immersion method, the literature does not provide any concrete informations about the related layer conformation for short print durations. However, as mentioned before, the molecular order is an important factor on which relies a lot of biochemical processes. Along with this conformational concern, μcp technique represents a powerful tool to produce molecular patterns onto substrates. However, because of the molecular ink diffusion on surfaces, the shorter the print duration is, the better the resolution turns out to be. Indeed, Helmuth et al. showed in their works that such diffusion effects can be nearly avoided by very fast printing processes (ms duration) and high ink concentrations [Helmuth et al., 2006] [Sharpe et al., 2004]. In order to correlate both the advantages of high resolution patterning (through free diffusion fast printing) and highly organized monolayers, we carried out this measurement campaign with the goal to characterize the relation between the layer conformation-orientation and the print duration [Lis et al., 2009]. The final aim is well to find out the minimum duration required to obtain a fairly ordered layer, but also that will optimize the pattern resolution because of less ink diffusion. To provide objective results, the organization and the orientation of micro-contact printed layers are compared with SAMs prepared by immersion, those latter being known to present very high conformal quality.

6.6 Fast micro-contact printing

This section, devoted to investigate the ability of μcp to form monolayers within brief durations, is divided into several steps. Firstly, the layer conformation properties are characterized regarding print durations by both SFG and contact angle measurements (1). Secondly, the orientation evolution of the associated alkyl chains is given from SFG spectroscopy (2). This first set of analyses is performed for unpatterned flat stamps. In order to validate the optimal conditions, the conformation (3) and orientation (4) of the alkyl chains have been compared with those of SAMs obtained by immersion. This enables to identify a minimal μcp duration leading to a monolayer quality level comparable with the immersion method one. Finally, a last step focusses on the patterning consequences in terms of molecular conformation/orientation (5). Note that the whole study has been performed for both HDT and DDT. We will however present the results relative to HDT only since no observable difference shows off for DDT.

6.6.1 Flat micro-contact printing - molecular conformation

SFG spectra of printed HDT SAMs on Pt recorded in ppp polarization within the CH stretching vibration window are presented in figure 6.3 for different printing durations ranging from 100 milliseconds to 60 seconds (while keeping a constant concentration of 50 mM and a print pressure of 25 N/cm^2). From a global spectra overview, five modes are observed (as before), namely the methyl symmetric

(ν^+CH_3 - 2880 cm^{-1}) and antisymmetric (ν^-CH_3 - 2965 cm^{-1}) stretching modes, the methyl Fermi resonance (Fr CH_3 - 2940 cm^{-1}), and the methylene symmetric (ν^+CH_2 - 2860 cm^{-1}) and antisymmetric (ν^-CH_2 - 2915 cm^{-1}) stretching vibrations [Noguchi et al., 2005] [Nishi et al., 2003] [Lu et al., 2004].

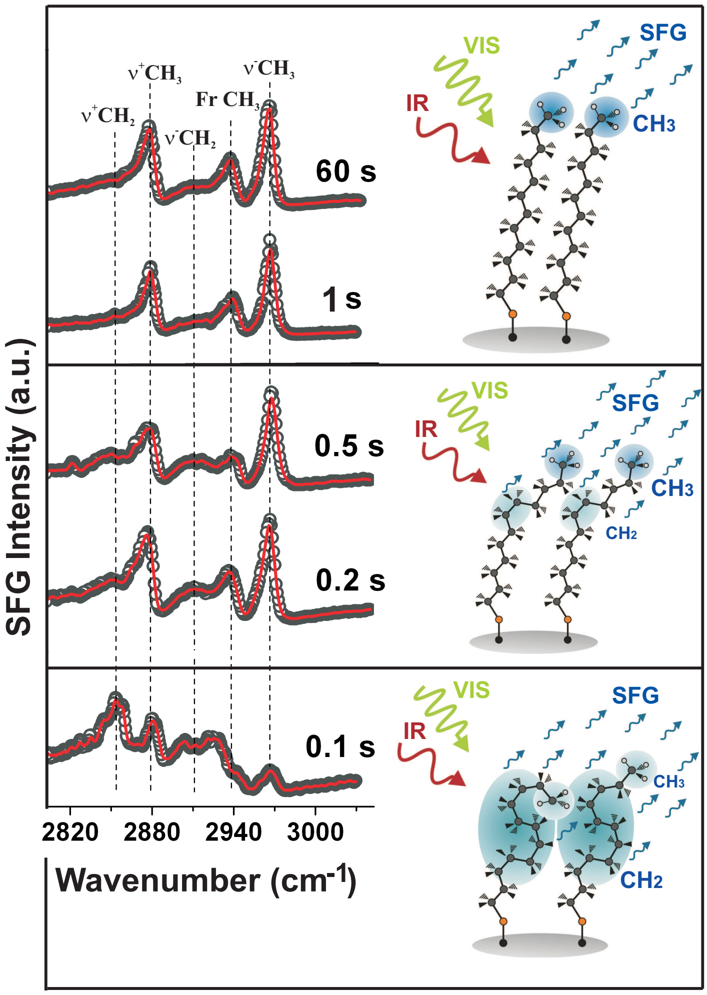

Figure 6.3: ppp polarized SFG spectra of microcontact printed HDT SAMs realized with printing durations ranging from 1 min to 100 ms and recorded in the methyl-methylene vibrational window. One can observe that over one second, defect free crystal like structures can be obtained. Between 1s and 200 ms, a few gauche defects in the methylene chain structures are present as suggested by the small CH_2 vibrational activity. Under 200 ms, important modifications in the methylene chain conformations take place and lead to a SFG spectrum dominated by the CH_2 signature. Blue areas mimic the SFG emission zone originating either from the methyl groups or from methylene chain gauche defects.

The small methylene SFG intensities observed for duration over 200 ms suggest a chain structure close to a crystal-like centrosymmetric configuration. However, degradations and disorder in the alkyl chain conformation occur for a printing duration smaller than 200 ms. In that case, the methylene vibrational components take a clear upper hand over the methyl terminal groups, what implies the film to be highly disordered with an increased amount of gauche defects [Guyotsionnest et al., 1987] [Himmelhaus et al., 2000] [Dreesen et al., 2006]. This clear tendency to go towards well-ordered structures from 100 ms to 200 ms print duration is however difficult to analyze since giving an accurate estimation of the gauche defect number is hardly achievable in SFG.

In order to corroborate the SFG data, wettability contact angle measurements of pure water have been performed on non-patterned μcp layers. The figure 6.4 plots the angle values corresponding to measurements run over the μcp HDT monolayers on Pt(111) with printing durations ranging from 100 ms to 60 s.

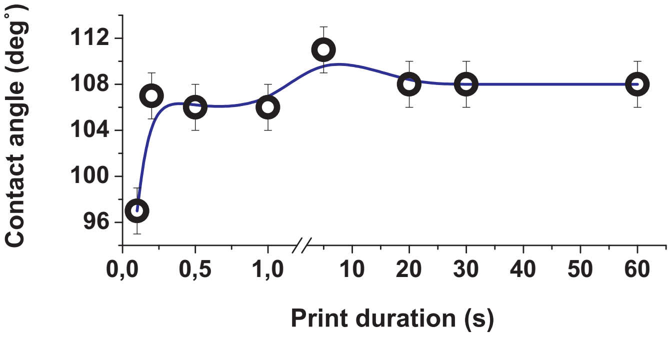

Figure 6.4: *Pure water contact angle values of HDT SAMs printed on platinum as a function of the printing duration. For long durations, the contact angle is close to the methyl one while for durations under 200 ms, a sharp drop of the angle value is observed, corresponding to the presence of methylene groups on top of the film, and thus to an effective layer disorder.*

Since the methyl and methylene groups carry distinct wetting properties, their surface water contact angles are not identical. They differ by about 10° and amount respectively to 110°- 112° and 102° [Lestelius et al., 1999] [Bain and Whitesides, 1989]. The curve depicted in figure 6.4 shows a pretty constant angle value of 107° for printing durations of 200 ms and more, while a sharp drop (10°) to 97°

is observed for a 100 ms printed film. This behaviour agrees well with the spectroscopic results and attests to clear structural degradations of the aliphatic chains within the film for printing durations shorter than 200 ms. Notice that the experimental contact angle measured for HDT SAMs realized by immersion is of about 110°.

6.6.2 Flat micro-contact printing - molecular orientation

Along with ppp polarized SFG spectra, the ssp configuration may provide precious informations on the molecular orientation. Spectra resulting from both polarization configurations are illustrated in the figure 6.5.

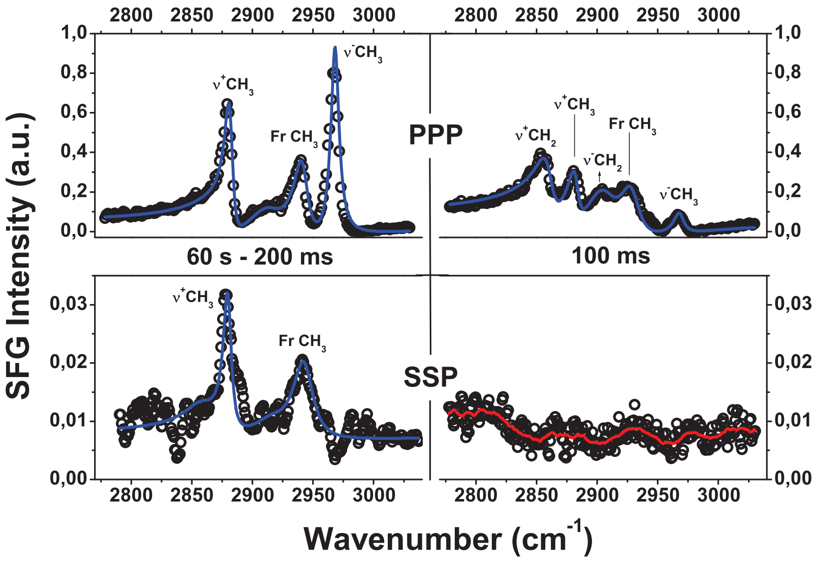

Figure 6.5: *SFG spectra of printed HDT films recorded in ppp (upper panels) and ssp (lower panels) polarization for 60 s - 0,2 s (left) and 100 ms (right) printing durations. Below 200 ms, methyl vibrational activities are reduced by the methylene chain disorder.*

Only two spectra for each polarization set are shown since they remain nearly unchanged over the 60 s to 0.2 s duration range (as shown in figure 6.3 for the ppp configuration). The ssp spectrum belonging to the film realized in 100 ms (right part) does not present a significant SFG signal. This is attributed to the global disorder within the layer together with a wider methyl orientational distribution, turning the layer close to a bulk-like environment. For such brief duration, only the ppp combinaiton enables to record a SFG activity, however mainly dominated by the methylene modes, as discussed previously (see stage C of the figure 5.6).

Note that the same spectral assignment as the ones performed on the figure 6.3 is applied. All spectra have undergone a Lorentzian least-squares fit over the five distinct vibrational modes as represented by the blue curves in the figure 6.5, excepted for the 100 ms in ssp configuration, for which the red curve is an average over the nearest neighbours. This allows to provide the required parameters for the orientation determination, as widely explained in the section 5.5. The NR phase parameters are the same as those in table [**?**], as well as mode widths and frequencies.

After the introduction of those parameters into the simulation program, namely both damping factors and frequencies of the methyl modes, along with both calculated IR and Raman activity tensors, an adjustment of the simulated peak intensities to the experimental spectrum for the ssp and ppp polarization, provides an angle of 45° for θ and 0° for ϕ, which defines the orientation of the terminal methyl group. Assuming an ideal all-trans conformation of the methylenes, an orientation of 10° for the alkyl chain is deduced. These results hold for printing durations between 60 s and 200 ms. No simulation is run for 100 ms since the molecular signature is dominated by the methylene groups, attesting to an important conformational disorder. The methyl groups and the alkyl chain are expected to be no longer organized in average, turning the simulation program ineffective to provide any significant information. Note that those results are easily reproducible.

6.6.3 Immersion self-assembling - molecular conformation

The SFG spectra of an HDT SAM on Pt realized by immersion, recorded for both ppp and ssp polarizations, are presented in the figure 6.6 (there are those used in section 5.5 to introduce the orientational retrieval method).

They are nearly identical to those realized by μcp for durations above 1 s (section 6.6.1 and 6.6.2). The same absence of gauche defect could be inferred from the small methylene vibrational activity, what attests to a high conformational level in the film structure. Comparisons with spectra shown in figure 6.3 reveal that one equivalent quality may be achieved between SAMs realized by μcp or by immersion processes, and this even for short print durations.

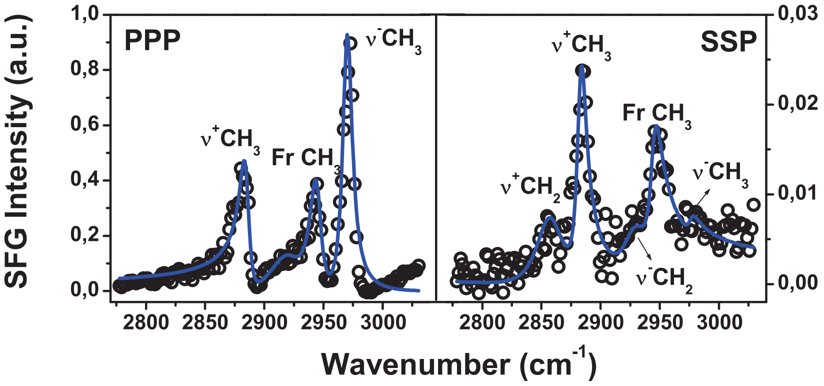

Figure 6.6: *SFG spectra (ppp and ssp polarizations) of a HDT SAM realized by the immersion of a Pt(111) in the solution. Both curves are fitted to a sum of Lorentzian modes (see section 5.5).*

6.6.4 Immersion self-assembling - molecular orientation

Theoretical simulations run for immersion SAMs provide orientational parameters very close to those assigned to μcp films, namely a tilt angle $\theta = 48^\circ$ and a twist angle $\phi = 0^\circ$, leading to a methylene chain orientation of 13° relative to the surface normal (as done in section 5.5). Those results are very reproducible from one sample to another and appear to be very homogeneous on the same sample. The difference of 3° between the SAMs produced by immersion or μcp method should not be considered as significant.

6.6.5 Patterned micro-contact printing - molecular conformation & orientation

The quality of patterned μcp SAMs of HDT is evaluated and compared to flat prints. First, we focused on the consequences that patterns may bring onto the global monolayer order and orientation. Second, we studied the effect of the print duration on the pattern formations. The question is whether or not a patterned monolayer owing a high structural conformation may be formed in a few hundreds of milliseconds as it is the case for flat printing. The patterns, which are HDT squares and stripes, both of 100 μm and 10 μm size, are printed onto a Pt(111) substrate.

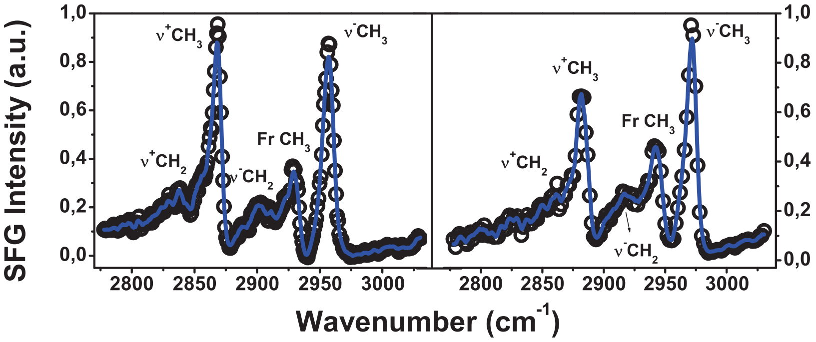

Figure 6.7: SFG spectra recorded in ppp polarization at two distinct spots on the sample. Both spots cover mixed HDT square and stripe of monolayers printed in 2 s, both sizing 100 μm and 10 μm. The same results are obtained for print durations included between 1s and 60 s (and longer).

Two SFG spectra recorded in ppp polarization are shown in figure 6.7 (the ssp ones are not shown because they are very similar to those of figures 6.6 and 6.5). They are assigned to two different spots on the sample, both of them including on purpose the different pattern sizes and shapes. This was achieved through beams of large diameters (1 mm). A small difference is observed in the tilt angle θ of the methyl for these two locations since the ratio between the symmetric and asymmetric methyl modes is slightly different. Simulations provide a tilt angle value close to 38° (0° twist angle) for the left spectrum of figure 6.7, while the right one shows off a $\theta = 46^\circ$. Therefore, from one spot to another, the tilt angle of the whole alkyl chain varies between 3° to 11° with respect to the surface normal. This behaviour suggests that the pattern geometry plays a role on the overall monolayer structure and thus on the methyl orientation distribution. This probably goes through local perturbations occurring at the pattern boundaries but also from the lack of molecular mechanical support undergone at those border locations.

Despite this small non-uniformity in the methyl group orientations, one can infer from the spectra that both methylene mode intensities do not undergo an important growth, although pattern edges should bring some disorder. Thus we can conclude that a large proportion of the patterns keeps the same high conformational quality as it is the case for a flat print. The print duration is tuned from 60 s to down 1 s as for flat printing. The SFG spectra show good monolayer organizations for durations of 1 s and above. Below this limit, degradations in the alkyl chain order are observed as demonstrated by the presence of strong methylene vibrational activity (data not shown). Consequently, patterned monolayers realized by the μcp process in less than a second do not present an as good molecular organization quality as the one achieved by flat printing.

Notice that the whole set of experiments presented in this chapter has been carried out with HDT molecule as μcp ink and immersion solution, but also with dodecanethiol (DDT). The orientational values found for the tilt and twist angles are undistinguishable between those two molecules. Moreover, the same dynamic of monolayer formations with respect to print durations has been observed, either for patterned or non patterned processes.

6.7 Printing of other molecules

The generalization of the effectiveness of μcp technique to form SAMs of alkanethiol molecules onto metal should not be inferred as an achievement when considering other molecules and substrates. Indeed, the very process taking place during the print is not understood yet. Only ex-situ studies have been carried out so far, and no one has developed a full model to explain the involved molecular dynamics. Many phenomena occurring at a microscopic scale between the stamp and the surface are still unknown. For instance, the effective molecular concentration reached in a micrometer solution layer between the stamp and the surface, during the print, is difficult to estimate because of the solvent and molecular diffusions into the stamp [Balmer et al., 2005]. This parameter alone is function of many factors, such as the solvent nature able to swell the stamp in variable degrees (retaining therefore a variable amount of liquid even after drying the stamp with N_2), the reticulation and mechanical properties of the stamp (function of the used ratio during the silicone mixture preparation), and the baking parameters (T°, time,...). Along with this, the local pressure applied to this thin micrometric solution film, and over all else, the physico-chemical properties of the molecule as well as those of the substrate, are all playing important roles on the final result.

The first remark concerns the wetting compatibility of the stamp. In our experiment, this latter is made up of a regular mixture proportion (10:1 base - curing agent) and is baked under the standard conditions of temperature and duration. The as produced stamp is by nature hydrophobic (from the apolar methyl groups). The fluorosilane used to obtain antisticking properties turns it even more hydrophobic. Since alkyl chains are non polar molecules, they are compatible with hydrophobic environment such as silicone stamp. Even if alkanethiol molecules own a thiol group, this latter is poorly polar and the major part of the molecule remains hydrophobic. But, what is it going to be with charged molecules repelled by hydrophobic surfaces? Actually, the literature gives example of hydrophilic molecular layer depositions through μcp technique, such as those of polymers (DNA) or lipid chains [Lange et al., 2004]. We have ourselves printed DNA molecules onto metallic substrates through thiol binding during the many studies carried out over DNA in our laboratory [Sartenaer, 2009]. We will not debate much about this molecule except to tell that comparable SFG spectra of DNA monolayers may be obtained either by immersion or print methods, meaning therefore that an effective amount of DNA is well transferred to the surface during the printing step. This means that the hydrophobicity of the stamp does not seem to constitute a obstacle for charged molecules to be printed. For any further informations about DNA SAM formation by immersion, we refer to the following works [Sartenaer, 2009] [Sartenaer et al., 2007].

A second remark concerns the substrate physico-chemical properties. Indeed, while a thiol group is highly reactive with metal and forms strong covalent bounds through chemisorption, is it necessary to perform an effective molecular printing? May a simple physisorption work out? The first necessary condition to perform an efficient physisorption is to care about the matching of the substrate and molecule wettability properties. A specific functionalization of the surface may therefore be required. While this step is fulfilled, it appears possible to produce organized layers from a micro-contact printed physisorption. Polar lipids have been successfully printed on hydrophilic metal surfaces in our lab and show up well organized structures through SFG spectroscopy (see chapter 7).

6.8 Resume

After having introduced the working of the μcp method, and reminded how to form SAMs by immersion, a brief description of the molecules and substrates used in our study is given. The different parameters involved in the μcp technique are then discussed, and more particularly the print duration. This latter turns out to be of key importance since the shorter it is, the better the resolution of the μcp patterns can be (no ink diffusion). From SFG spectroscopy and contact angle measurements, a print duration of 200 ms is identified as a minimal requirement to obtain a μcp SAM of hexadecanethiol on Pt owing a molecular conformation comparable to the one shown off by an immersion SAM. The orientation of the methyl terminal group (θ = 45°- 48° / ϕ = 0°) and thus of the alkyl chain (θ = 10° - 13°) is roughly the same for films obtained either by μcp or immersion assembly process. Next, surfaces patterned by μcp (10 μm and 100 μm HDT/DDT squares and bands) showed a high molecular organization for print durations over 1 s. However, the average methyl/alkyl chain tilt angle appears to be less uniform than the one obtained on unpatterned μcp monolayers. Indeed, from one location to another, a variation of about 10° in the methyl orientation may be observed.

Since we expect the Pt surface to be oxidized before thiol coverage, the binding and assembling dynamics of alkanethiols is estimated to occur slower than on gold and silver. We can therefore anticipate an even shorter required print duration for these two metals. This fact leads to a smaller molecular diffusion and consequently to the possibility of printing molecular patterns of higher spatial resolution.

Besides the chemisorption of apolar alkanethiol molecules, the potentialities of micro-contact printing to be used with charged molecules, or with the physisorption process is discussed. This technique appears to be quite versatile and compatible with much systems.

To conclude, the micro-contact printing method allows to generate monolayers presenting a conformational quality comparable to those of regular SAMs produced by immersion, with the exception that it requires seconds instead of hours to do so, and futhermore, it could lead to micrometric patterns with nearly no more effort.

6.9 Bibliography

[Bain and Whitesides, 1989] Bain, C. D. and Whitesides, G. M. (1989). Formation of monolayers by the coadsorption of thiols on gold - variation in the length of the alkyl chain. J. Am. Chem. Soc., 111(18):7164–7175.

[Balmer et al., 2005] Balmer, T. E., Schmid, H., Stutz, R., Delamarche, E., Michel, B., Spencer, N. D., and Wolf, H. (2005). Diffusion of alkanethiols in pdms and its implications on microcontact printing (mu cp). Langmuir, 21(2):622–632.

[Bohm et al., 1999] Bohm, I., Lampert, A., Buck, M., Eisert, F., and Grunze, M. (1999). A spectroscopic study of thiol layers prepared by contact printing. Applied Surface Science, 141(3-4):237–243.

[Clavilier et al., 1980] Clavilier, J., Faure, R., Guinet, G., and Durand, R. (1980). J. Electroanal. Chem., 107:205.

[Dreesen et al., 2002] Dreesen, L., Humbert, C., Celebi, M., Lemaire, J. J., Mani, A. A., Thiry, P. A., and Peremans, A. (2002). Influence of the metal electronic properties on the sum-frequency generation spectra of dodecanethiol self-assembled monolayers on pt(111), ag(111) au(111) single crystals. Appl. Phys. B - Lasers O, 74(7-8):621–625.

[Dreesen et al., 2006] Dreesen, L., Volcke, C., Sartenaer, Y., Peremans, A., Thiry, P. A., Humbert, C., Grugier, J., and Marchand-Brynaert, J. (2006). Comparative study of decyl thiocyanate and decanethiol self-assembled monolayers on gold substrates. Surf. Sci., 600(18):4052–4057.

[Guyotsionnest et al., 1987] Guyotsionnest, P., Hunt, J. H., and Shen, Y. R. (1987). Sum-frequency vibrational spectroscopy of a langmuir film - study of molecular-orientation of a two-dimensional system. Physical Review Letters, 59(14):1597–1600.

[Helmuth et al., 2006] Helmuth, J. A., Schmid, H., Stutz, R., Stemmer, A., and Wolf, H. (2006). High-speed microcontact printing. J. Am. Chem. Soc., 128(29):9296–9297.

[Himmelhaus et al., 2000] Himmelhaus, M., Eisert, F., Buck, M., and Grunze, M. (2000). Self-assembly of n-alkanethiol monolayers. a study by ir-visible sum frequency spectroscopy (sfg). J. Phys. Chem. B, 104(3):576–584.

[Laiho and Leiro, 2006] Laiho, T. and Leiro, J. A. (2006). Influence of initial oxygen on the formation of thiol layers. Appl. Surf. Sci., 252(18):6304–6312.

[Lang et al., 1998] Lang, P., Mekhalif, Z., Rat, B., and Garnier, F. (1998). Self-assembled alkylthiols monolayers onto platinum; influence of the adsorbed oxygen. J. Electroanal. Chem., 441(1-2):83–93.

[Lange et al., 2004] Lange, S. A., Benes, V., Kern, D. P., Horber, J. K. H., and Bernard, A. (2004). Microcontact printing of dna molecules. Analytical Chemistry, 76(6):1641–1647.

[Lee et al., 2006] Lee, S., Park, J., Ragan, R., Kim, S., Lee, Z., Lim, D. K., Ohlberg, D. A. A., and Williams, R. S. (2006). Self-assembled monolayers on pt(111): Molecular packing structure and strain effects observed by scanning tunneling microscopy. J. Am. Chem. Soc., 128(17):5745–5750.

[Lestelius et al., 1999] Lestelius, M., Engquist, I., Tengvall, P., Chaudhury, M. K., and Liedberg, B. (1999). Order/disorder gradients of n-alkanethiols on gold. Colloid. Surface. B, 15(1):57–70.

[Li et al., 2003] Li, Z. Y., Chang, S. C., and Williams, R. S. (2003). Self-assembly of alkanethiol molecules onto platinum and platinum oxide surfaces. Langmuir, 19(17):6744–6749.

[Lis et al., 2009] Lis, D., Peremans, A., Sartenaer, Y., Caudano, Y., Mani, A. A., Dreesen, L., Thiry, P. A., Guthmuller, J., Champagne, B., and Cecchet, F. (2009). Self-assembled film organization in fast microcontact printing investigated by sum frequency generation spectroscopy. Journal of Physical Chemistry C, 113(22):9857–9864.

[Lu et al., 2004] Lu, R., Gan, W., Wu, B. H., Chen, H., and Wang, H. F. (2004). Vibrational polarization spectroscopy of ch stretching modes of the methylene goup at the vapor/liquid interfaces with sum frequency generation. J. Phys. Chem. B, 108(22):7297–7306.

[Nishi et al., 2003] Nishi, N., Hobara, D., Yamamoto, M., and Kakiuchi, T. (2003). Chain-length-dependent change in the structure of self-assembled monolayers of n-alkanethiols on au(111) probed by broad-bandwidth sum frequency generation spectroscopy. J. Chem. Phys., 118(4):1904–1911.

[Noguchi et al., 2005] Noguchi, H., Ito, M., and Uosaki, K. (2005). Molecular orientation of self-assembled monolayer of octadecanethiol on platinum surface studied by femtosecond broad-bandwidth sum frequency generation spectroscopy. Chem. Lett., 34(7):950–951.

[Petrovykh et al., 2006] Petrovykh, D. Y., Kimura-Suda, H., Opdahl, A., Richter, L. J., Tarlov, M. J., and Whitman, L. J. (2006). Alkanethiols on platinum: Multicomponent self-assembled monolayers. Langmuir, 22(6):2578–2587.

[Sartenaer, 2009] Sartenaer, Y. (2009). Etude des biocapteurs par spectroscopies optiques non lineaires. PhD Thesis, FUNDP.

[Sartenaer et al., 2007] Sartenaer, Y., Dreesen, L., Humbert, C., Volcke, C., Tourillon, G., Louette, P., Thiry, P. A., and Peremas, A. (2007). Adsorption properties of decyl thiocyanate and decanethiol on platinum substrates studied by sum-frequency generation spectroscopy. Surf. Sci., 601(5):1259–1264.

[Sharpe et al., 2004] Sharpe, R. B. A., Burdinski, D., Huskens, J., Zandvliet, H. J. W., Reinhoudt, D. N., and Poelsema, B. (2004). Spreading of 16-mercaptohexadecanoic acid in microcontact printing. Langmuir, 20(20):8646–8651.

[Ulman, 1996] Ulman, A. (1996). Formation and structure of self-assembled monolayers. Chemical Reviews, 96(4):1533–1554.

[Wang et al., 2001] Wang, J., Chen, C. Y., Buck, S. M., and Chen, Z. (2001). Molecular chemical structure on poly(methyl methacrylate) (pmma) surface studied by sum frequency generation (sfg) vibrational spectroscopy. J. Phys. Chem. B, 105(48):12118–12125.

[Zhuang et al., 1999] Zhuang, X., Miranda, P. B., Kim, D., and Shen, Y. R. (1999). Mapping molecular orientation and conformation at interfaces by surface nonlinear optics. Phys. Rev. B, 59(19):12632–12640.

Chapter 7

Solid supported lipid film formation and patterning

7.1 Introduction

This chapter is dedicated to the study of biological films constitude with amphiphilic molecules. Those particular classes of components, including lipid species, hold both hydrophilic and hydrophobic groups. The fact that cell membranes in every single living body are build with such amphiphilic molecules turns them to be highly interesting for many research fields [Sackmann, 1996] [Parikh and Groves, 2006] [Castellana and Cremer, 2006]. It is thus critical to model such membrane organisms as close to the reality as possible. To do so, it is either possible to study vesicles in the liquid phase, or to produce solid supported flat films. This latter process is commonly achieved by a physisorption of singles or bi(multi)-layers performed through adapted techniques, one of those being the Langmuir-Blodgett method (LB). The conformational qualities of the as produced layers along with the best experimental LB parameters involved in the lipid film formation, are evaluated by SFG spectroscopy. Different molecules will be employed for this evaluation of film constructions by vibrational non-linear techniques. Finally, we will introduce a way to pattern the supported lipid layers by combining Langmuir-Blodgett methods with micro-contact printing (μcp). Once the supported model membranes are produced, typical biological interactions occurring between cells and inner/outer cell environments will be accessible for further investigations.

7.2 Methods to build solid supported lipid films

7.2.1 Langmuir-Blodgett

Among few ways to generate supported membranes-like lipid films on solid interfaces [Parikh and Groves, 2006] [Castellana and Cremer, 2006], the Langmuir-Blodgett method, besides being the more regular, is the one that allows the best control of the layer properties [Ulman, 1991]. To describe the method, a 3-dimensional scheme of the Langmuir apparatus is shown in Figure 7.1.

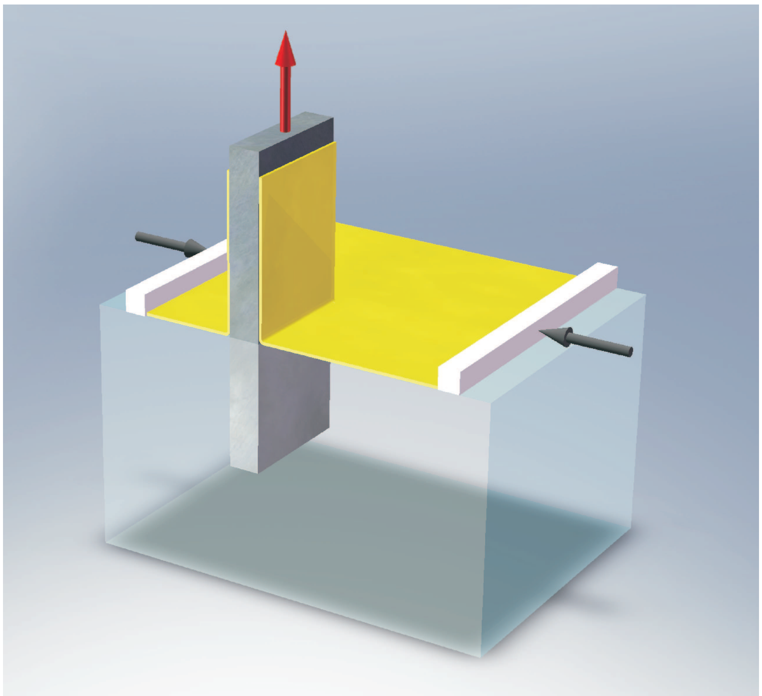

Figure 7.1: *Principle of the Langmuir-Blodgett method able to produce solid supported membrane-like films.*

In few words, an amphiphilic molecular film (such as a lipid one) is first formed at the liquid-air interface (yellow sheet over the water on figure). The strain-less freedom of the film while being at the liquid-air interface, makes its density and conformation to be easily controlled. When stabilized in an densely packed structure, the molecular film is transferred onto a solid substrate (gray piece on figure 7.1) by a vertical pull back of the sample.

The liquid solution contains usually 1 mg of lipid for each ml of solvent (a 1 mg/mg concentration). This latter is highly volatile and non-miscible in water (typically chloroform, but depending upon the solvability properties of the amphiphilic molecule) so as to remains over the water phase and to quickly evaporate. This solution is gently spread by the use of a micro litre syringe over the surface of the water contained in the Langmuir-Blodgett trough. When the solvent is fully evaporated, only the lipid molecules remain at the water-air interface, their hydrophilic heads immersed into the water. Notice that the injected volume of solution is intended to obtain a low density lipid film spread over all the trough area, and presenting therefore a rather disordered structure at the water interface. To increase the interfacial molecular density of lipid and to achieve a highly packed and structured layer, the film is compressed by means of movable barriers (white piece in the figure) themselves half immersed into the water. While the lipid film has reached the desired density (below the maximal density value, otherwise it will collapse), the sample is slowly pulled out from the trough (as shown in figure 7.1 and 7.2).

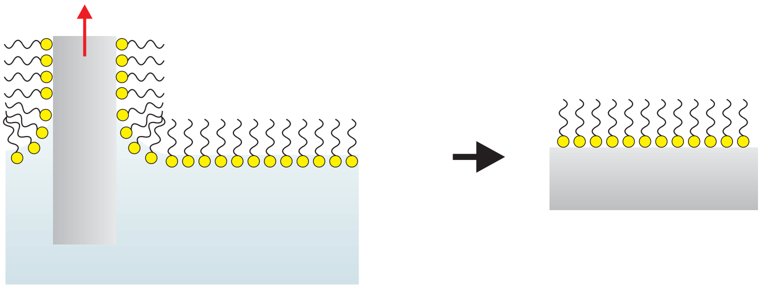

Figure 7.2: *Scheme of the Langmuir-Blodgett method to build-up solid supported amphiphilic layers on a hydrophilic sample. The polar heads are physisorbed onto the sample while the apolar tails point-out in the air.*

Notice first that the sample was dipped into the water before spreading the lipid solution, and second that, the barriers move closer from each other during the sample pull out step to maintain a constant molecular surface density. Moreover, the lipid layer can be efficiently transferred onto the substrate only if this latter holds an appropriate hydrophilicity matching the polar head wetting properties. This is a key factor to turn the sample into an adequate layer support and to perform a strong physisorption. The platinum single crystal substrate is thus beforehand cleaned in a piranha solution and then exposed for 20 min. to a UV-ozone treatment.

To go further, it is possible to perform the reverse process, by using a hydrophobic solid substrate and dipping it into the water after the interfacial lipid layer formation (panel A of figure 7.3). The supported lipid layer will thus present its polar heads at the surface instead of the apolar tails like before. Finally, it is possible to combine both deposition ways, to produce multilayer lipid deposition (panel b of figure 7.3) by cycling one method after the other.

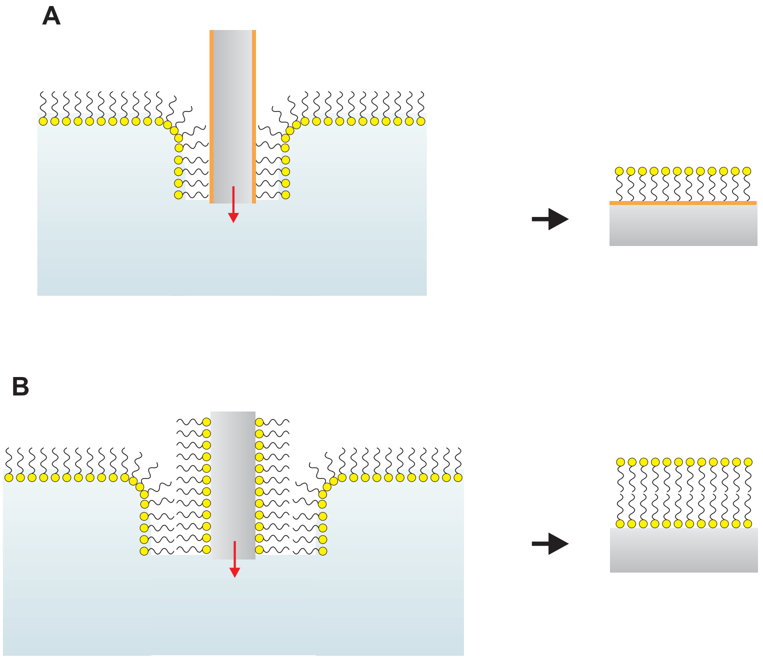

Figure 7.3: *Scheme of the Langmuir-Blodgett method to form solid supported amphiphilic layer (lipid) on a hydrophobic substrate (A, hydrophobic properties coloured in orange). In this case, the sample is dipped into the LB trough and a lipid monolayer is formed owning polar heads at the outside. The B part describes the multilayer supported lipid formation by successive LB dip and pull out steps.*

Notice however that for those methods to be efficient, the cleanliness of all Langmuir-Blodgett apparatus and solutions is crucial. The major part of microscopic impurities (organic or ionic) will locate themselves at the water interface and thus inside the lipid layer. Consequently, any amount of dirt, as small as it might be, will disturb the interfacial lipid layer structure. For this reason, the water is bidistilled 18,4 MΩ cm purity and the chloroform solvent is of ultra pure spectroscopic grade (Sigma Aldrich, $>$ 99,8 %). The LB apparatus components (trough and barriers) are made-up of Teflon because of its anti-sticking hydrophobic properties, limiting the amount of impurities that will stick between the cleaning steps, but also during the experiment itself. The high purity amphiphilic molecules are purchased from specialized manufacturers (Avanti Polar Lipids, Inc.).

7.2.2 Langmuir-Schaefer

The Langmuir-Schaefer (LS) technique is a variant of the LB one [Ulman, 1991]. The whole apparatus and mechanical devices are the same (trough, barriers, Wilhelmy plate, balance, dipper arm, etc...) as well as samples and solutions. The difference takes place in the way of transferring the amphiphilic layer onto the solid sample. In the LS method, while the film of amphiphilic molecules is formed at the water interface with the targetted molecular density, the sample (which owns hydrophobic surface properties) is moved downward with its entire surface plane parallel to the water interface (as depicted in figure 7.4).

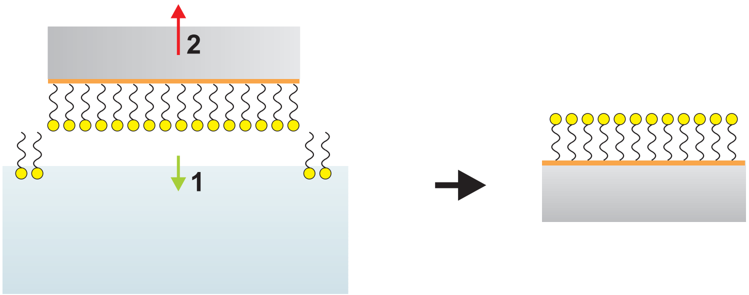

Figure 7.4: Scheme of the Langmuir-Schaefer method to build amphiphilic layers on solid substrates.

Once against the water, and so in contact with the lipid film, the sample is carefully lifted up. The physisorption between the apolar tails and the hydrophobic sample surface leads to a complete transfer of the film onto the solid sample at once. When a single lipid layer with the polar heads up configuration is wanted, this process is easier to perform than the LB one (panel a of figure 7.3).

7.3 Control of the film properties: the LB isotherm

For both LB or LS methods, the whole sample construction procedure is based on 3 distinct steps, namely the solution injection, the interfacial film compression, and finally, the film transfer onto the solid substrate. To quantify, to qualify and to manage each step, a Wilhelmy plate is used to provide the liquid-air surface pressure within the trough. The device consists of a platinum plate (~ 10 x 20 x 1 mm), vertically suspended to an accurate electrobalance, the plate being partially immersed in the water trough, its own weight being measured in real time. Since amphiphilic species are surfactants, they lower the interfacial tension of the water after their injection in the trough. Consequently, the more compressed the amphiphilic layer, the weaker the repulsive strength acting on the plate by the interfacial tension, what finally increases the measured weight of the plate. From this variation of plate weight, one might deduce the variation of the surface tension. Let us define the surface pressure (positive amount) as being the pure water surface tension (72.8 mN/m) minus the water-lipid surface tension (≤ 72.8 mN/m).

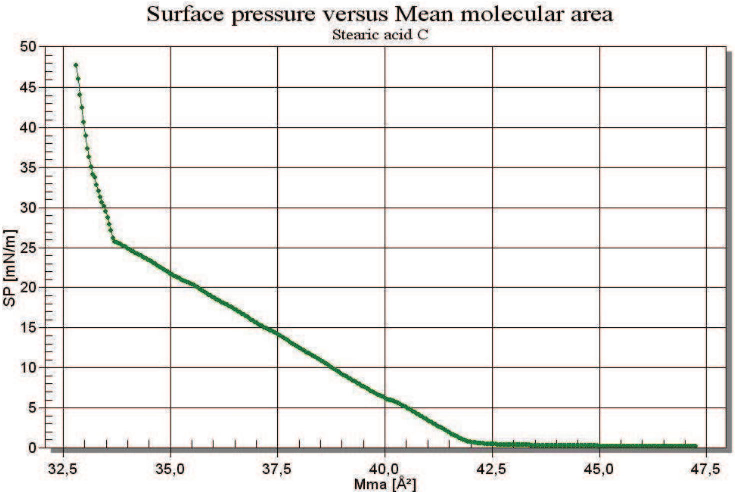

Figure 7.5: *LB isotherm of stearic acid.*

The evolution of this surface pressure value with the barrier compression is called the LB isotherm. The measure of compression is often expressed in terms of the Mean molecular area (Mma Å^2), quantity easily calculable since the total amount of lipid is known as well as the trough surface. The isotherm curve of stearic acid (CH_3-$(CH_2)_{16}$-COOH) is presented in figure 7.5.

During the solution injection, the surface pressure has to remain as close to zero as possible (nearly as pure water since the layer is not compressed yet). Once the solution is well spread on the surface (10 min after the injection, a stability of the surface pressure to a value lower than 5 mN/m is usually reached), the compression of the layer may begin. The compression rate is very small (5 mm/min) and the surface pressure increase is monitored in function of the Mma. One may observe that the evolution of the curve presented in the figure 7.5 is not linear and is futhermore function of the molecular species (see difference between figure 7.5 & 7.10). A typical isotherm shows off three regimes of surface pressure increases. The flat one in the right part of the curve is associated to the gas-like phase, for which the lipid molecules are disordered and spaced from each other at the water surface. The middle of the curve shows a smooth slope associated to the liquid-like phase, for which the molecules are slowly coming closer and begin to self-organize. Finally the solid-like phase at the top left shows a much sharper surface pressure increase for a constant compression rate. This behaviour underlines a step by step reorganization of the lipid layer during the compression until reaching a dense and uniform film presenting organized apolar tails up to the air. Notice that if the layer is further compressed, the surface pressure will reach a maximum (theoretically lower than 72.8 mN/m, typically around 60 mN/m) before collapsing. Indeed, once the Mma is smaller than the physical dimension of the molecule, the film breaks down and sinks (vesicles formation) into the water along with a sharp surface tension drop.

Experimentally, once a defined value of surface pressure is achieved (let us say 50 mN/m), the barriers slow down and keep gently moving in order to maintain this targeted value. While the film is dynamically stabilized (a few minutes), the sample is slowly uplifted (or dipped) whereas the barriers restart compressing the layer to keep a constant surface pressure and thus a uniform layer density over the entire sample surface. The same procedure is applied for the LS method, except that no further compression is requested during the one shot horizontal molecular transfer onto the sample.

Note that from the surface pressure measurement, a bad cleaning of the trough is clearly noticed by a compression of the sole water interface. Impurities are indeed sufficient by themselves to lower the surface tension of the water and be detected by the highly accurate electrobalance connected to the Wilhelmy plate.

7.4 SFG measurements on Langmuir films

This section is devoted to present SFG measurements carried out on stearic acid films (molecule shown in figure 7.6) realized by Langmuir-Blodgett/Schaefer methods.

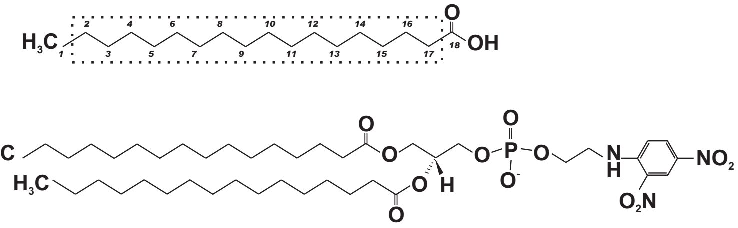

Figure 7.6: Chemical structures of stearic acid (top) and "DNP" (bottom, full name: 1,2-Dipalmitoyl-sn-Glycero-3-Phosphoethanolamine-N-(2,4-dinitrophenyl)).

Basically, the stearic acid is an alkyl chain with a carboxyl end group (saturated fatty acid). The capacity of such molecule to form an organized and structured film from LB methods is evaluated by SFG spectroscopy through the analysis of the alkyl chain symmetry properties [Ye et al., 2003]. The Langmuir-Blodgett isotherm of this molecule was presented in figure 7.5.

The SFG spectrum of a stearic acid film supported on a platinum (111) single crystal is shown in figure 7.7. The SFG measurement is performed in ppp polarization within the CH_3-CH_2 stretching spectral window. One can see from the lack of methylene vibrational activity that the Langmuir-Blodgett method allows the construction of supported amphiphilic layers of great quality regarding the crystalline organization of the alkyl chain. This molecule (as well as lauric acid, result not shown here) was considered as a first test to acquire a good handling of the Langmuir-Blodgett apparatus. Note that the solid phase slope in the stearic acid isotherm is very sharp. Great cautions have thus to be taken during the final step of the compression so as not reaching the collapse phase prematurely (some kind of compression inertia effect shows-up).

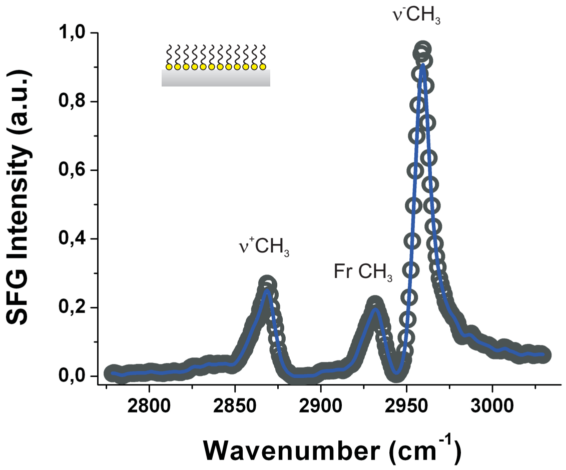

Figure 7.7: *SFG spectrum of stearic acid film realized by Langmuir-Blodgett (polar heads down) on a platinum single crystal in ppp polarization set within the methyl vibrational region. No methylene vibration is detected attesting to a well ordered alkyl chain strucutre.*

7.5 Langmuir and μcp to pattern supported lipid layers

Langmuir methods have been proved to be able to produce high quality amphiphilic films, and more particularly lipid mono/bi-layer [Ulman, 1991] [Castellana and Cremer, 2006]. Those models of solid supported membranes are very important in the bio-science field [Sackmann, 1996] [Parikh and Groves, 2006] [Meuse et al., 1998]. The flat and hard surface nature of supported membranes enables a wider panel of structural analysis that are more difficult in, or not compatible with, aqueous conditions (X-ray photoelectron microscopy, IRAS, ellipsometry, SFG, SPR, etc...), even mechanical ones (AFM, STM) [Meuse et al., 1998] [Chen et al., 2007] [Chen and Chen, 2006] [Moran-Mirabal et al., 2005]. This enables a deeper understanding of all the interaction processes occurring between cells and outer bodies such as proteins, sugars, lipids, drugs... [Parikh and Groves, 2006]. Besides, as it is often requested in sensoring application domains, molecular patterns on the samples turn out to be more profitable because allowing to run multiple parallel experiments at the same time. Supported lipid patterning is actually little developed and only few works do mention such achievements [Groves et al., 1997] [Okazaki et al., 2006]. In this framework, we have tried to associate the micro-contact printing technique to Langmuir-Blodgett methods with the goal to realize patterned samples of supported amphiphilic layers [Park et al., 2005].

The concept is depicted by the following scheme (figure 7.8).

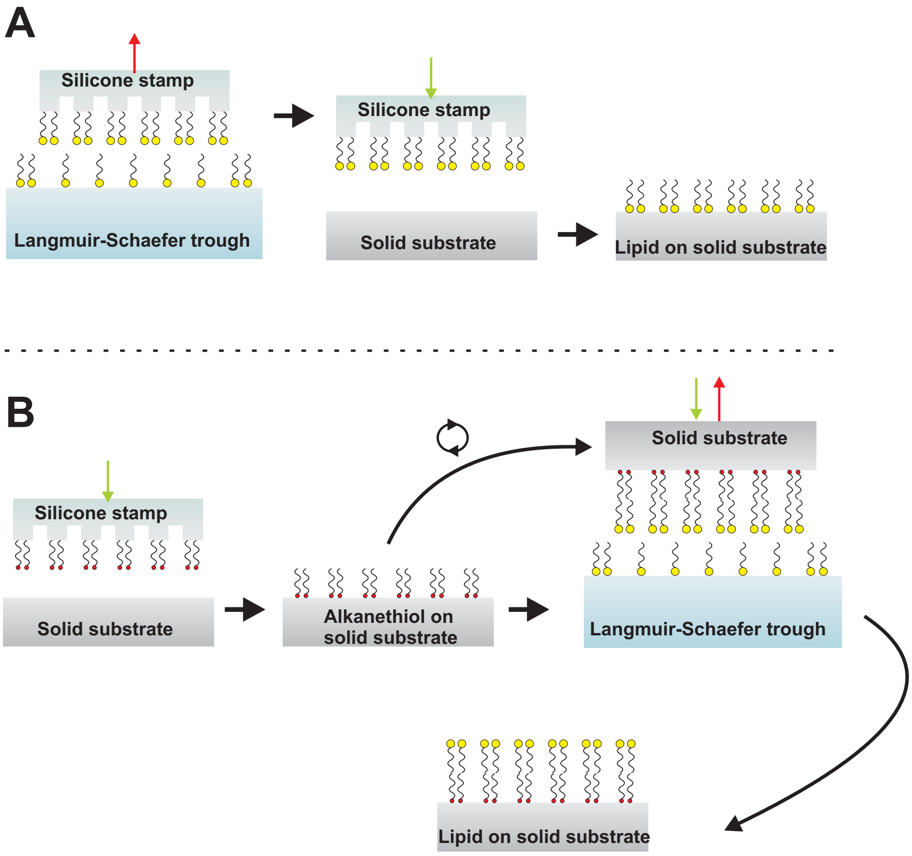

Figure 7.8: *Scheme depicting two distinct processes for solid supported lipid patterning. The first one (A) applies the LS method straight to the silicone stamp prior to print onto the solid sample. A polar head down patterned film is obtained. The second (B) requires a pattern of alkyl molecule (DDT for example) achieved through μcp on the solid substrate; this latter undergoes thereafter a LS step in order to obtain polar heads up patterned solid supported film.*

The "A" method consists of a deposition of a pre-organized lipid film onto a patterned silicone stamp by means of Langmuir-Schaefer process. The stamp is then micro-contact printed onto the sample, leading to a patterned solid supported lipid layer. This first method allows simulating the inner part of the membrane that presents the apolar tails at the outside (polar heads are down on the sample). In the "B" method, a hydrophobic molecular pattern is first printed onto the sample, as for example alkane thiol molecule (alkyl chains pointing out with strong hydrophobicity properties). After that the patterned DDT layer has been built on the sample, the LS step is applied to it, allowing the apolar tails to physisorb on the top of the DDT pattern areas. This method allows simulating the outer part of the membrane with polar heads up on the sample

7.5.1 Stearic acid

In order to validate the methods described in the figure 7.8, non patterned stamps have first been used.

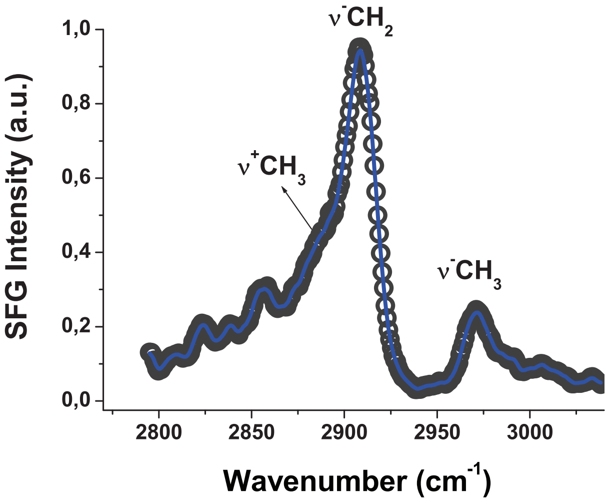

Figure 7.9: *SFG spectrum of a stearic acid film realized by method "A" (figure 7.8). Since the methylene vibrational activities are much more important that the methyl ones, the film is expected to be in poor structural condition, disqualifying therefore the working of method "A" with stearic acid.*

The patterning ability will easily be achieved later if the working principle of "A" or/and "B" method(s) is confirmed. We have first carried out the test with stearic acid (as well as with lauric acid). The figure 7.9 shows a SFG spectrum of a stearic acid film formed by the "A" method onto a platinum single crystal substrate. One can see that the main peak at 2920 cm^{-1} allocated to the asymmetric methylene stretching dominates the spectrum and is far more important than both methyl vibrational components (2970 and 2885 cm^{-1}), attesting of a disordered layer and disqualifying therefore the validity of method "A" to generate high quality films. Moreover, the same result is observed when using the method "B". The whole set of experiments have been repeated with lauric acid as well with no more sucess. However, this observation is not valid for all amphiphilic species, as shown here after. Some hypothesis to explain the failure of this patterning method with saturated fatty acids are given later.

7.5.2 DNP lipid

Both methods have been repeated with a more complex amphiphilic molecule, namely the DNP phospholipid (shown in figure 7.6). This particular classe of molecules is the major component of all membrane cells. Their structure is constituted of a polar head group containing one or several phosphate groups. What makes this DNP molecule highly interesting is its antigenic properties. Antigens are macromolecules able to produce an immune response (through antibodies) in living organisms. Those substances may be bacterias, virus or micro-organisms (allergens, poisons...), that, when in contact with living organisms, bind to specific antibodies to produce an adapted immunogenic response. The DNP polar head is representative of a synthetic chemical agent acting as a cellular metabolic poison. It is widely used to simulate much more complex antigen molecules in many researches about immunology [Parikh and Groves, 2006] [Uemura and Kinsky, 1972].

Both "A" and "B" methods have been applied to the DNP molecule to obtain (flat but potentially patterned) solid supported lipid films. However, before describing results associated to both patterning methods (illustrated in figure 7.8), the isotherm of the DNP film compression in the Langmuir trough along with the SFG spectrum of its supported film realized by LB (the LS one is very identical) on a platinum single crystal substrate are presented in figure 7.10.

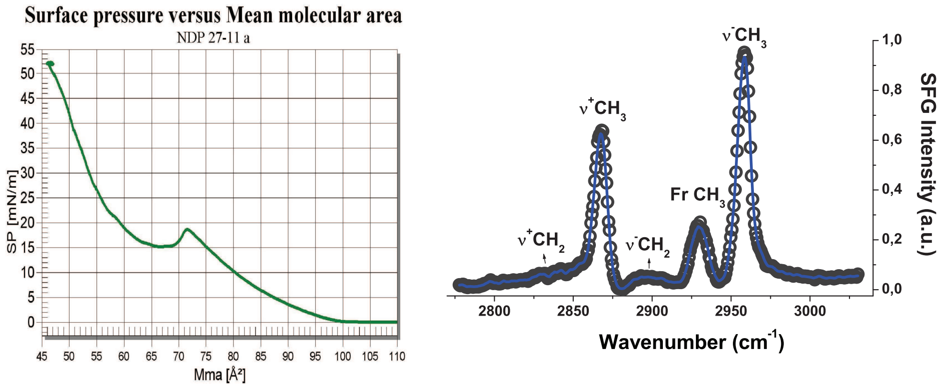

Figure 7.10: *DNP compression isotherm (left), and SFG spectrum of DNP film supported on platinum single crystal recorded in the methyl-methylene vibrational window (right). This sample was built by using the classical Langmuir-Blodgett method.*

The spectrum is acquired in ppp polarization configuration within the 2800 - 3000 cm^{-1} range. Since only weak methylene activity is observed (as shown on the spectrum), both DNP alkyl chains should be quite straight and fairly aligned on the platinum sample surface. One may notice the overshoot-hump in the surface pressure - Mma curve located around 70 Å^2. This is attributed to a change in the dinitrophenyl moiety conformation at the air-water interface occurring during the compression [Makino et al., 1997]. The transfer surface pressure value was experimentally set to 52 mN/m. Both single LB and LS methods provide DNP supported layer with a high level of structural conformation.

Method "A" - unpatterned

The figure 7.11 presented the SFG spectrum of the supported lipid layer constructed by method "A". The film is obtained with a flat stamp. The overall result reveals very few methylene vibrational activity, validating therefore the method. This involves that silicone stamps are fully able to transfer a pre-organized lipid layer from the liquid-air interface to the solid substrate without disturbing its conformation.

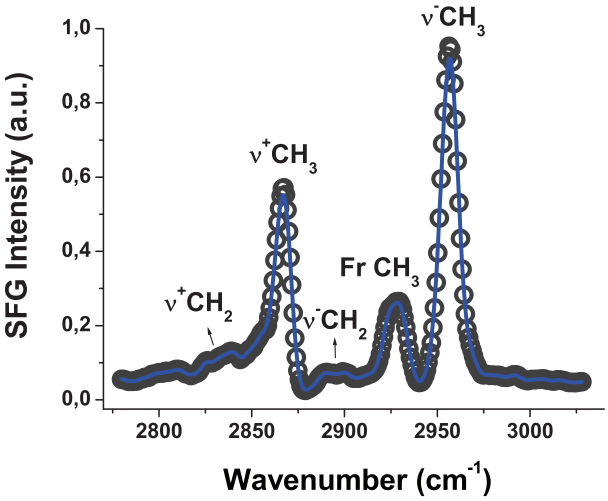

Figure 7.11: *SFG spectrum of supported DNP lipid layer. The sample is realized by transferring the film from the trough (Langmuir-Schaefer) to the solid substrate by means of a stamp (by μcp). The lipid polar heads lie down on the sample (platinum) surface. From the absence of methylene vibrational activity, the film is assumed to be organized and thus method "A" to be successful.*

Method "B" - unpatterned

The "B" method (depicted in figure 7.8) was also applied fruitfully. The SFG analysis is carried out in two steps. First, we record the vibrational signature of the printed hydrophobic alkyl chain (DDT) to ensure a perfect organization of this support layer, as discussed in chapter 5. The second step involves the analysis of the lipid layer physisorbed over the DDT SAM through Langmuir-Schaefer process. The lone methyl-methylene signature is however not sufficient to make the distinction between the DDT and the DNP lipid since alkyl chain structures are present within both films.

To unequivocally detect the presence of the lipid layer, we have probed one other spectral region by SFG, and also measured the surface wettability properties by contact angle. This latter measurement provides an angle of around 45° after the adsorption of the DNP by LS. This is far from the 110° of the methyl group of the DDT, and tend to indicate the presence of hydrophilic groups, such as the NO_2

and the phosphate entities located in the DNP polar head.

Along with this wettability measurement, other vibrational fingerprints have been detected through SFG spectroscopy performed in the 1380 - 1260 cm^{-1} spectral range (as shown in figure 7.12). Two vibrations have been observed at 1344 cm^{-1} and 1305 cm^{-1}.

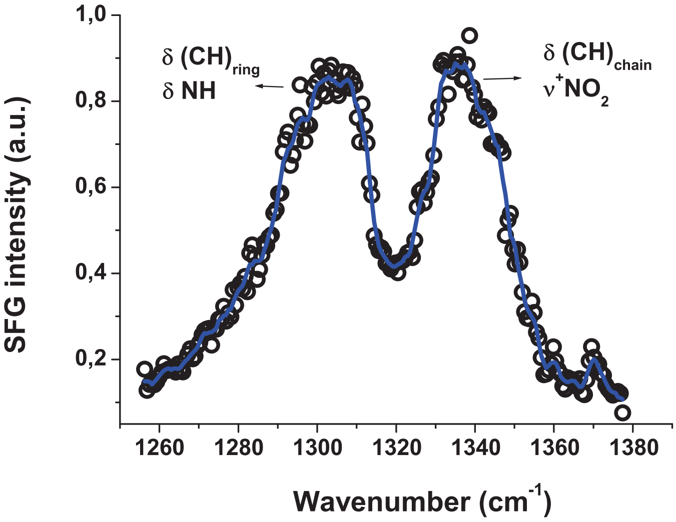

Figure 7.12: *SFG spectrum of DNP solid supported film on a Pt(111) sample (realized by method "B") in the 1300 cm^{-1} spectra frame. The spectrum was realized by means of a free electron laser at the CLIO facility, University of Paris-Sud.*

In order to reliably assign the observed SFG vibrational modes, DFT calculations have been performed (in collaboration with the CTA laboratory, FUNDP) to identify the vibrational modes and their frequencies, as well as to estimate both IR and Raman (and thus SFG) activities. For this purpose, a model molecule with an optimized geometry has been used. This latter is very similar to the DNP with the exception that both aliphatic chains pocess only two carbons instead of sixteen. There is thus no methylene included in the apolar tails. This procedure allows to assign the peak at 1344 cm^{-1} to the stretching of the para-NO$_2$ group superimposed to the CH bending, while the peak at 1305 cm^{-1} is allocated to the CH bending of the phenyl ring along with the NH bending. Those new vibrations fully prove the presence of the DNP lipid over the DDT layer.

Besides, the SFG spectra in the CH_3-CH_2 spectral windows are nearly unchanged between the lone DDT layer and the DDT-DNP mixed bilayer. This lack of default in the whole mixed alkyl chain structures proves that the DDT layer is not (or weakly) disorganized by the incoming of the DNP film over it, and that the DNP layer itself owns a high conformational level (at least in both apolar methylene chains).

The SFG measurements in the 1380 - 1260 cm^{-1} spectral region (figure 7.12) have been performed with a free electron laser infrared source (CLIO facility, University of Paris-Sud) instead of a regular OPO's based table-top laser. This SFG work is included in a wider measurement campaign around the DNP lipid supported films. It was meant to characterize those films over a broad spectral range, but also to give prominence to the antigen-antibody free label recognition as well in the air and in solution. Those results are still under investigation by Francesca Cecchet. The weak SFG vibrational activity of the lipid head group and the need for a spectrally broad vibrational investigation justify the use of a free electron laser, able to provide a widely IR tunable source (mid-far IR) with high power.

The previous results proved the efficiency of both "A" and "B" methods to deliver supported DNP lipid films by μcp.

Note that the exact reason why those methods work with the DNP and not with saturated fatty acids (such as lauric or stearic acid) is not clear, but we may mention some differences that may explain this behaviour: the DNP has a double alkyl chain, is a zwitterion (carries both a positive and a negative charge), and has a higher molar mass than small fatty acids. These factors could be in charge of different molecule-stamp and molecule-substrate interactions occurring in both LS and μcp processes involve in the "A" and "B" methods.

Patterned methods

The running of both methods has been demonstrated successfully with unpatterned stamp. The patterning ability in itself required only the use of a particular stamp presenting the desired 3 dimensional structures. However, while the method "A" leads to single lipid monolayers with apolar tails in the air, expected to be quite stable, the method "B" leads to mixed bilayers (DDT-DNP) with polar heads in the air (see figure 7.8). In this latter case, it would be suitable to increase the stability of the bilayer by one extra step. This would help to avoid the diffusion of the physisorbed DNP lipid molecules over the DDT, as well as its flip in the holes inbetween the DDT patterns.

To increase the stability of the mixed bilayer, a third molecular species with appropriate hydrophilicity is thus chemisorbed between the primary DDT patterns. This step is performed before the deposition of the lipid layer by LS. Practically, after having printed DDT patterns on the platinum sample, the chemisorption of mercapto-dodecanol (OH-$(CH_2)_n$-SH) is completed following a "backfilling" procedure described in the literature (one hour of chimisorption with a 1 mM solution concentration) [Baralia et al., 2005]. We have beforehand verified by SFG spectroscopy that a DNP film can not be transferred by LS onto a mercapto-dodecanol pre-layer. This is due to the fact that the strong hydrophilicity of the OH end groups does not enable apolar tails to physisorb onto them.

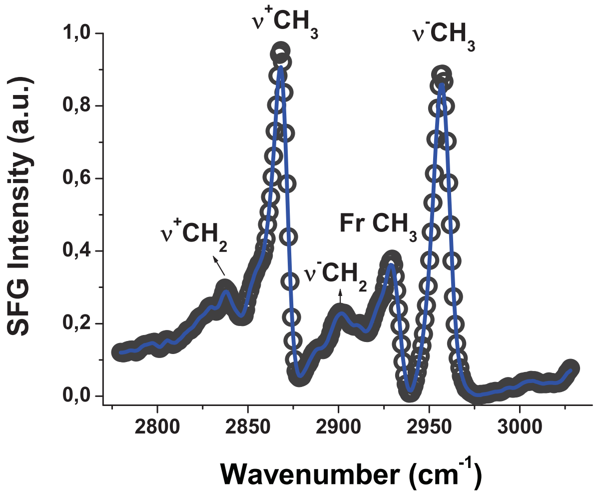

Figure 7.13: *SFG spectrum of 100 μm DDT stripes backfilled with mercapto-dodecanol. The resemblance with the one of the lone DDT printed stripes (chapter 6) attests that the backfilling step does not damage the printed DDT layer and leads simultanously to a fairly organized mercapto-dodecanol film since only weak methylene activity is detected.*

A last test is to verify the structural condition of the DDT layer after the OH backfilling. We have thus printed 100 μm stripes of DDT on a platinum sample, realized a backfilling of OH end-group molecules in between those stripes, and check the sample quality through SFG analysis. The spectrum (shown in figure 7.13) is not significantly different from the one presented for the DDT printed stripes only (see chapter 6). The OH backfilling process is thus assumed to be damage-less to the pre-printed alkanethiol layer and appears to lead to structured mercapto-dodecanol patterns.

This measurement proves that a Langmuir-Schaefer step with the DNP molecule perfomed on a sample owning mixed patterns of CH_3 and OH end groups will lead to an efficient physisorption of the lipid in the DDT areas only while no lipid at all will remain in the OH zones in between. The next step is now to study this kind of sample with SFG microscopy (see next chapter).

7.6 Resume

This chapter presents Langmuir-Blodgett methods and their possible combinations with micro-contact printing. We have reviewed the different methods enabling to build lipid films onto solid substrates. The SFG spectroscopy has highlighted the high structural quality of such solid supported amphiphilic layers, first for model molecules (stearic and lauric acid), and then for the DNP phospholipid molecule holding antigenic properties. We have introduced the necessity to generate patterned lipid layers and have designed two ways to achieve this goal by combining Langmuir and micro-contact printing methods. Even if both ways did not work for stearic/lauric acid, it works successfully for the DNP molecules. The combination of table-top OPOs laser and free electron laser infrared source have allowed us to fully characterize the adsorption of this DNP lipid film on solid substrates and have demonstrated the possibility to obtained molecular patterns.

7.7 Bibliography

[Baralia et al., 2005] Baralia, G. G., Duwez, A. S., Nysten, B., and Jonas, A. M. (2005). Kinetics of exchange of alkanethiol monolayers self-assembled on polycrystalline gold. Langmuir, 21(15):6825–6829.

[Castellana and Cremer, 2006] Castellana, E. T. and Cremer, P. S. (2006). Solid supported lipid bilayers: From biophysical studies to sensor design. Surface Science Reports, 61(10):429–444.

[Chen and Chen, 2006] Chen, X. Y. and Chen, Z. (2006). Sfg studies on interactions between antimicrobial peptides and supported lipid bilayers. Biochimica Et Biophysica Acta-Biomembranes, 1758(9):1257–1273.

[Chen et al., 2007] Chen, X. Y., Wang, J., Boughton, A. P., Kristalyn, C. B., and Chen, Z. (2007). Multiple orientation of melittin inside a single lipid bilayer determined by combined vibrational spectroscopic studies. Journal of the American Chemical Society, 129(5):1420–1427.

[Groves et al., 1997] Groves, J. T., Ulman, N., and Boxer, S. G. (1997). Micropatterning fluid lipid bilayers on solid supports. Science, 275(5300):651–653.

[Makino et al., 1997] Makino, M., Sasaki, C., Nakamura, K., Kamila, M., and Yoshikawa, K. (1997). An overshoot-hump in a pi-a curve and the cooperative aggregation among dinitrophenyl moieties in phospholipids at air/water interface. Progr. Cooloid. Polym. Sci., 106:215–218.

[Meuse et al., 1998] Meuse, C. W., Krueger, S., Majkrzak, C. F., Dura, J. A., Fu, J., Connor, J. T., and Plant, A. L. (1998). Hybrid bilayer membranes in air and water: Infrared spectroscopy and neutron reflectivity studies. Biophysical Journal, 74(3):1388–1398.

[Moran-Mirabal et al., 2005] Moran-Mirabal, J. M., Edel, J. B., Meyer, G. D., Throckmorton, D., Singh, A. K., and Craighead, H. G. (2005). Micrometer-sized supported lipid bilayer arrays for bacterial toxin binding studies through total internal reflection fluorescence microscopy. Biophysical Journal, 89(1):296–305.

[Okazaki et al., 2006] Okazaki, T., Morigaki, K., and Taguchi, T. (2006). Phospholipid vesicle fusion on micropatterned polymeric bilayer substrates. Biophysical Journal, 91(5):1757–1766.

[Parikh and Groves, 2006] Parikh, A. N. and Groves, J. T. (2006). Materials science of supported lipid membranes. Mrs Bulletin, 31(7):507–512.

[Park et al., 2005] Park, J. I., Lee, W. R., Bae, S. S., Kim, Y. J., Yoo, K. H., Cheon, J., and Kim, S. (2005). Langmuir monolayers of co nanoparticles and their patterning by microcontact printing. Journal of Physical Chemistry B, 109(27):13119–13123.

[Sackmann, 1996] Sackmann, E. (1996). Supported membranes: Scientific and practical applications. Science, 271(5245):43–48.

[Uemura and Kinsky, 1972] Uemura, K. and Kinsky, S. (1972). Active vs. passive sensitization of liposomes toward antibody and complement by dinitrophenylated derivatives of phosphatidylethanolamine. Biochemistry, 11(22):4085.

[Ulman, 1991] Ulman, A. (1991). An introductions to ultrathin organic films: From langmuir-blodgett to self-assembly. Book, Academic Press.

[Ye et al., 2003] Ye, S., Noda, H., Morita, S., Uosaki, K., and Osawa, M. (2003). Surface molecular structures of langmuir-blodgett films of stearic acid on solid substrates studied by sum frequency generation spectroscopy. Langmuir, 19(6):2238–2242.

Chapter 8

Sum-frequency generation microscopy

8.1 Introduction

This last chapter discusses about a nonlinear spectroscopic imaging method, the SFG microscopy. While SFG spectroscopy, like it was performed all along the previous chapters, collects the entire signal intensity coming from the sample through one global photomultiplier tube amplification, the imagery method allows to map the spectroscopic signal intensity over the surface with a micrometric spatial resolution. In spite of the weak SFG signal intensity, last generation CCD cameras enable such interfacial vibrational mapping. This specific technique of sample characterization is quite unique and deserves a particular attention. It however requires state of the art technologic tools to be performed, as well for the laser part as for the imagery one. One task in this thesis was to develop such a efficient laser set up and to establish an image acquisition procedure. Once done, a few samples have been analyzed at the very end of this thesis to demonstrate the working of our brand new SFG microscope. Perspectives are given about the many potential applications that this recent breakthrough in spectroscopy field may provide.

8.2 High power IR/Vis tunable laser sources

We have discussed in chapter 5, the way to collect the SFG signal originating from a sample interface, through a double monochromator spectral filter and a photomultiplier tube amplifier. This latter device turns the few emitted photons into a massive current of electrons which can be detected by an oscilloscope. The amplification efficiency is higher than a factor 1000. On the other hand, microscopy imaging requires the SFG signal to be spread over hundreds of thousands of pixels, each of them materializing an independent sensor that has to be individually efficiently processed.

The latest generation of amplified CCD cameras allows pixel by pixel amplification steps, but even if the gain is as efficient as 1000 times, the amount of photons hitting each CCD pixel is very low. A necessary approach is therefore to maximize the quantity of photons that hit the CCD surface and thus to maximize the nonlinear second-order output from the sample.

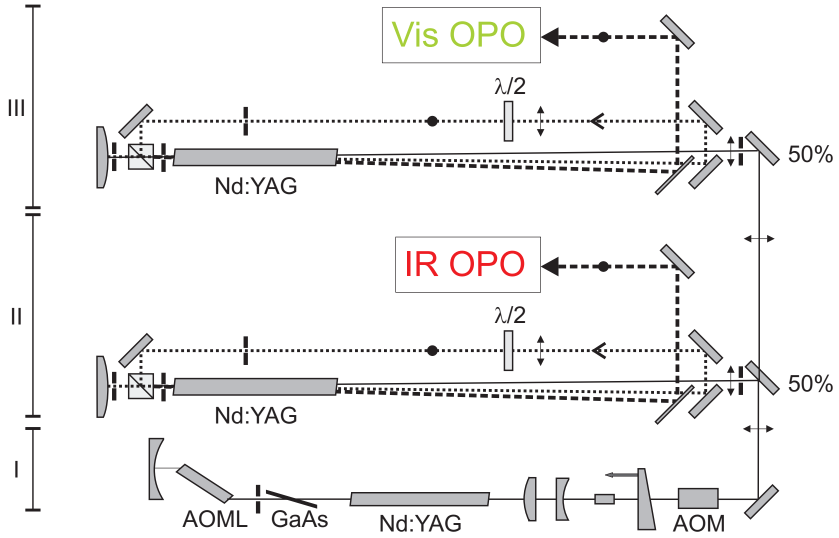

Figure 8.1: Scheme of the laser amplification stage (II and III) in the SFG microscopy set up. This amplification is performed by an individual Nd:YAG head for both OPOs, each of them being set up in a three pass configuration. The full line is the first pass; the dotted line is the second one, and the dashed line the third one.

The only way to do so is to increase the laser set up performances themselves.

The laser outputs have to present high power infrared and visible emissions, with good power homogeneity (spatial beam profile), as well as short pulse durations (to maximize the peak power).

In this quest for power, a brand new SFG laser set up has been designed and built in our laboratory those last two years. The main assets are that both the infrared and visible OPOs possess their own amplification Nd:YAG head instead of a shared one, like it is done in our primary SFG spectrometer describes in figure 5.1. Furthermore, three passes are realized by the pump through both heads while only two were performed on the other system (shown in figure 8.1). The three pass set up principle has been thoroughly described elsewhere in laboratory works [Lis and Peremans, 2005]. The resulting improvement is not negligible since the OPOs pump power (1064 nm) is five time higher (3 W) in comparison to our first spectrometer, and this for a lower applied voltage of the flash lamp. This voltage parameter has to be considered because the higher it is, the more important is the thermal strains in the Nd:YAG rod, what leads to a degradation of the beam profile quality at the output (depolarization and thermal lens effects). This beam profile quality is however critical since it is involved in the imaging process. The efficiency of the nonlinear generation being proportional to the incident power, we expect a Gaussian beam profile (TEM 00 mode) with no disturbed spatial power distribution.

The laser tunability is achieved by an infrared and a visible OPO similar to those described in the chapter 5. However, because of the higher intensities involved, larger beam diameters are required to avoid damages to optical components. As before, the infrared wavelength tunability extends from 2.7 to 10 μm by means of two distinct crystals ($LiNbO_3$: 2.7 to 4 μm; $AgGaS_2$ type II: 5 to 10 μm; $AgGaS_2$ type I: 2.7 to 10 μm), the latter one might be set either in type I or II interaction (see section 5.3).

The IR working powers are typically around 200 mW[1] in the 2.7 - 4 μm spectral range (30 mW on the primary SFG spectrometer) with a $LiNbO_3$ crystal, while it amounts to 15-20 mW in the 5-10 μm with a regular type II $AgGaS_2$ crystal. The respective wavelengths and powers that may be emited from those three configu-

---

[1] 8 mJ per pulse train at 25 Hz, 800 mJ/cm^2, the mean pulse intensity = 400 MW/cm^2.

ration are shown in figure 8.2.

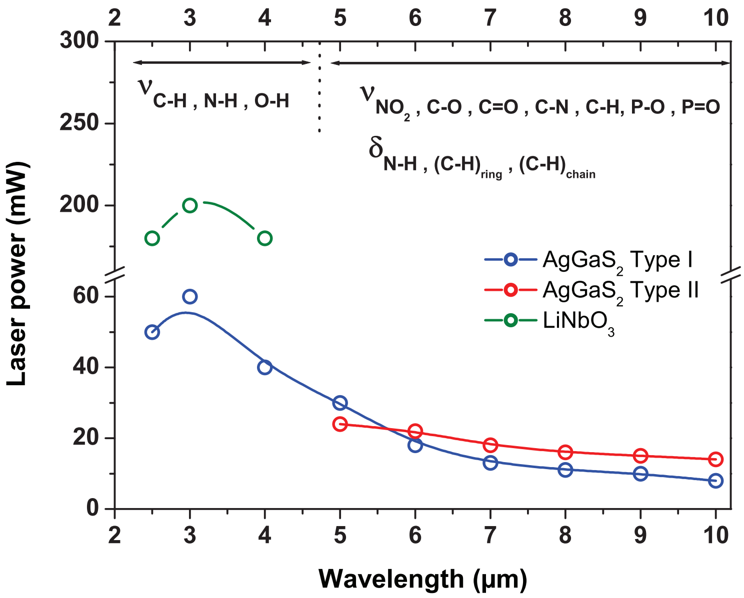

Figure 8.2: Infrared OPO output power as a function of the wavelength for three different crystal set up.

Another alternative lies in the use of a type I AgGaS$_2$ crystal, allowing to access the full spectral range (2.7 to 10 μm) but, in counterpart, with less power (the crystal owns a lower damage threshold). The choice of the adequate configuration relies mainly on the measurement that has to be performed. Indeed it is more coherent to carry out both 3 μm and 7 μm measurement successively on the same sample if required (type I AgGaS$_2$, but less power), while more power is preferred if only one wavelength measurement is needed (either LiNbO$_3$ or type II AgGaS$_2$) [Mani, 2004].

Along with the IR source, the visible OPO based on a BBO crystal allows to generate 420 to 700 nm wavelengths. Until now, we have used the second harmonic beam at 532 nm (we do not go through the OPO) with a power of 200 mW. This allows obtaining a wide (more than 5 mm) and very homogeneous beam spot with enough power to be at the damage threshold of any sample.

This state of the art picosecond Nd:YAG laser set up is one of the most efficient in the world for spectroscopic applications [Flörsheimer et al., 1999] [Ji et al., 2006] [Shen et al., 2000] [Cimatu and Baldelli, 2008] [Kuhnke et al., 2003] [Hedberg et al., 2007]. Indeed, tunable picosecond OPOs with such amount of power at the output are exceptionally uncommon.

8.3 SFG Imaging: the method

Along with the laser performance optimization, the latest generation of imaging devices is requested. The chosen camera model is a Hamamatsu C9100-13 EM-CCD (Electron Multiplying Charge-Coupled Device), with a very high quantum efficiency and a sensor chip cooled down to -90°C.

In order to obtain a high spatial resolution of the sample image, an enlargement of the SFG beam is necessary. However, beyond a maximal factor given by the diffraction limit (Rayleigh criterion), any further magnification will not provide more details. Since the best resolution imposed by the diffraction limit approximately amounts to the wavelength of the probing light (SFG is in the blue around 460 nm → 500 nm), it is close to half a micrometre in our case. Therefore, the maximal efficient magnification of the beam will be reached by imaging two sample points spaced by 500 nm on two pixels. Over the whole CCD array (512 x 512 pixels, each one sizing 16 μm), this maximal efficient enlargement means imaging a sample square zone being 256 μm wide. The CCD chip sizing 8 mm wide, a magnification of 32 times (8 mm → 250 μm) is already enough to reach the physical limit of the imaging process.

To perform the magnification, adapted optics has to be used. However, the more components involved, the more losses the beam will undergo. Actually one single lens is sufficient to enlarge the beam, while placing the CCD sensor in the optical image plane. For a given CCD distance (L) from the sample along with a given lens focus (f), we are able through the classical Descartes formula (1/l + 1/l' = 1/f) to provide the magnification (M) and the precise lens position (l and l') to get the image plane right on the CCD sensor position. The figure 8.3 and table 8.1 present the scheme and the data summarizing different possibilities.

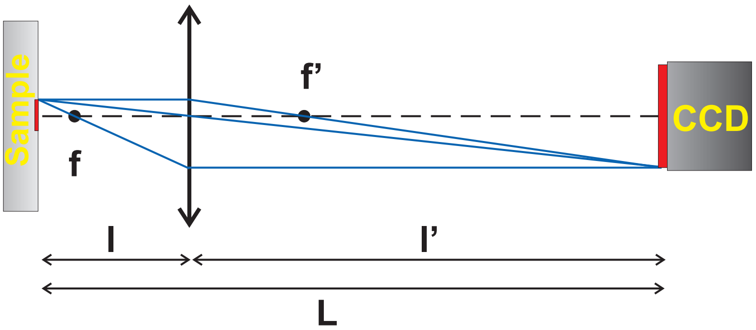

Figure 8.3: *Scheme of the SFG image enlargement process achieved with one single lens. The different involved parameters are defined. For given L and f, it is possible to find the magnification factor M as well as l and l' in order to obtain a sharp and well defined image on the CCD sensor.*

L (mm)	f (mm)	M	l (mm)	l' (mm)
500,0	**25,00**	17,9	26,39	473,6
	30,00	14,6	32,06	467,9
	35,00	12,2	37,87	462,1
	40,00	10,4	43,84	456,2
750,0	**25,00**	28,0	25,89	724,1
	30,00	23,0	31,31	718,7
	35,00	19,4	36,81	713,2
	40,00	16,7	42,40	707,6
1000,0	**25,00**	38,0	25,66	974,3
	30,00	31,3	30,96	969,0
	35,00	26,5	36,32	963,7
	40,00	23,0	41,74	958,3

Table 8.1: *Quantification of the M, l and l' parameters for a given L (fixed CCD position) and f value (a defined lens). We observed that for a lens of 30 mm of focal length, the magnification factor varies from 14,6 to 31,30 for a CCD distance included between 50 and 100 cm from the sample, leading to an imaged square area measuring from 548 to 256 μm length on the sample.*

From the table above, we see that a lens having a 30 mm focal length allows a magnification of 15 to 31 times for a CCD distance to the sample from 50 to 100 cm. However, different focal length values may be used to obtain lower magnification factor. Notice that the lens separation from the sample is critical (see the small variation of the l factor) and that it should be accurately positioned within a fraction of millimeter (micrometre screw) to obtain a proper sharpness of the image. In order to optimize the microscopy set up and all the distance parameters that go along with the measurement, we have firstly recorded the image of a GaAs sample plate, this latter substrate having a huge non resonant SFG background. To focalize on visual details, we have used a GaAs sample patterned with a polymer (here the polymer is intented to hide the substrate background, involving the polymer patterns to be negative, as shown in figure 8.4). The image is intense and contrasted, allowing therefore an accurate adjustment of the best experimental parameters, after what only small re-adjustments are required when replacing the GaAs plate with a other sample.

Even if it may appear common, this step is actually an absolute necessary. Indeed, with real samples, the intensity is so low that images have to be acquired for seconds or tens of seconds (thanks to our high power system while other SFG groups have to wait 5 minutes...) [Hedberg et al., 2007] [Hoffmann et al., 2002] [Cimatu and Baldelli, 2008]. Although the fact that this is a competitive system in itself, it is nearly impossible to adjust the image focusing with such long exposures. This would require hours of work, what would thus irrevocably go along with sample degradations. However, since GaAs plate provides an intense signal, real time adjustments may be realized at the best on the polymer patterns, leading to a system close to be ready for the samples of interest.

The figure 8.4 shows SFG images of such GaAs patterned plates used for the adjustment of the imagering chain. Those captions were recorded for fixed visible frequency (532 nm - 100 mW) as well as fixed infrared frequencies (3.3 μm - 150 mW), in the ppp configuration. The acquisition duration was 250 ms, the CCD was set at its maximal amplification value, no background substraction was performed. The image A displays 100 μm squares with a 8x magnification; the B presents 100 μm squares and stripes with M = 5x; the C shows 100 μm stripes with M = 14x; the D reveals stripes of 10 and 100 μm with M = 23x; the E and G expose 10 μm stripe with M = 20x and 16x respectively; and finally the F illustrates 10 μm squares and stripes with M = 20x. We may see that the spatial resolution is within the μm range on high magnification shots showing 10 μm features. The contrast on picture A, for which the focusing is optimal, is really high between two pixels; the image being 1 mm, each pixel sizes 2 μm. Besides, even if the focussing is not so sharp on picture D, each pixel represents 680 nm, what is close to the optical limitation of the SFG microscope. As expected, it appears experimentally that higher enlargements that M = 30x do not lead to more detailed captions.

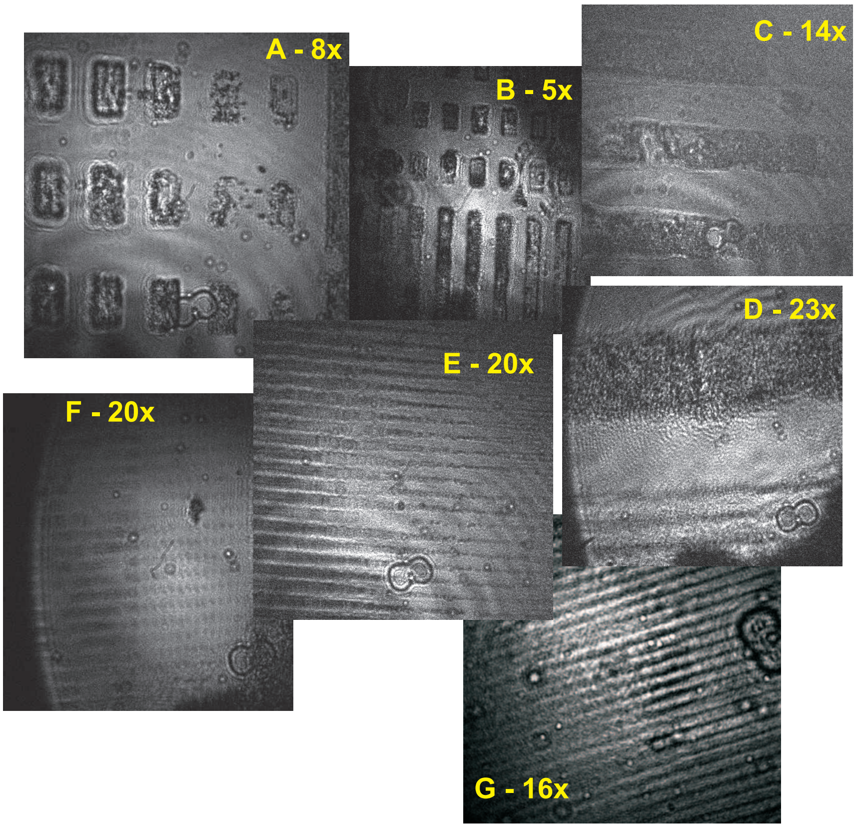

Figure 8.4: *Resume of the SFG microscopy images obtained on an GaAs sample patterned with opaque polymer. A, B and C are 100 μm squares and lines, D is a mixed 100 and 10 μm width lines, E & G are 10 μm bands, and finally, F is 10 μm squares and stripes.*

The standard conditions for recording SFG images are the following : the CCD sensor temperature is -90°C (water cooling), the camera entrance is protected by three band pass filters plus one notch filter, any image is recorded in a fully dark room, and finally, the laser itself is contained in an opaque box to avoid light pollution from the optical pumping by flash lamps.

8.4 SFG imagery of alkanethiol patterns

The next step is to obtain SFG microscopy images from patterned molecular interfaces. The classical alkanethiol SAM has been micro-contact printed on platinum and analyzed by SFG imagery. Square and line patterns of 100 and 10 μm dimension have been probed in the methyl-methylene spectral region. The DDT molecule may look like a model molecule, but actually a spatial mapping of the structural conformation specific to interfacial molecular films is a very unusual information, even for as simple molecules as alkanes. Moreover, DDT is a fair choice to begin this set of measurement since the methyl SFG activity is especially important in the 3 μm spectral range, where the laser source is the more efficient.

Let us remember to the reader that since the first publication about SFG microscopy in 1999 by Flörsheimer et al., many progresses have been performed [Flörsheimer et al., 1999]. In this very first study, they have imaged (for 10 min.) methyl groups of a flat LB arachidic acid layer. In a second work by Kuhnke et al. (with another SFG spectrometer), they have imaged GaAs plates as we have done in the previous section. [Hoffmann et al., 2002] [Kuhnke et al., 2003]. However, it has required them two hours (7200 s) of exposure to obtain a contrasted image of the GaAs plate border. A few years later, we are now able to take real time (0.2 s) images of the sample! This is why the reader has to understand the exceptional performance of recording SFG images on samples for which the intensity is 30 to 1000 times weaker than the GaAs signal!

Until now, among the publications issued on SFG microscopy, half of them deal with alkanethiol layers while the others focus on GaAs plates, CO and CN groups, micro-particles and LB films [aforementioned papers + the following] [Cimatu et al., 2008] [Cimatu and Baldelli, 2007] [Cimatu and Baldelli, 2006b] [Cimatu et al., 2007] [Cimatu and Baldelli, 2006a] [Fu et al., 2007].

The figure 8.5 presents our results obtained for DDT printed films on platinum single crystal. The samples have been prepared as described in the chapter 6. The exposure duration is around 10 s in EM-CCD mode (amplification factor at maximal value). The IR frequency matches the methyl antisymmetric vibrational mode (2970 cm^{-1}) with a power of 100 mW, the visible source is a 100 mW beam at 532 nm of optical frequency. The polarization is ppp. Note that the blue color is false.

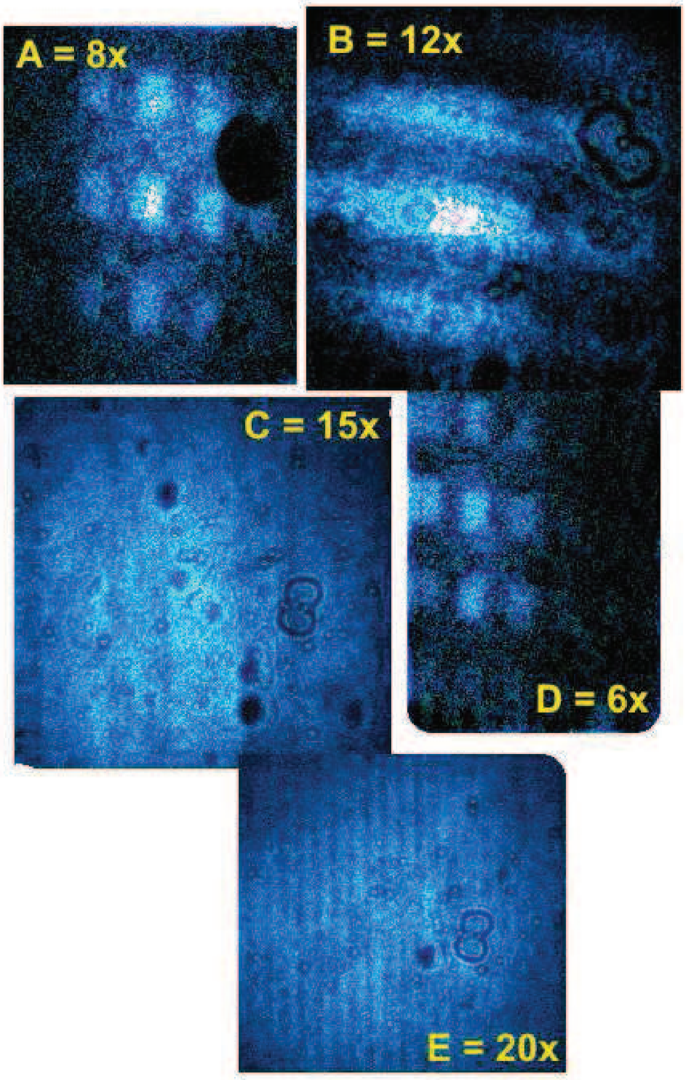

Figure 8.5: *SFG microscopy imaging of DDT squares and lines patterned by micro-contact printing onto platinum single crystal at the methyl vibrational frequency. The top four images show off 100 μm size features, while the bottom one presents 10 μm stripes. As we may observe, real samples lead to weaker intensity than the one obtained with non resonant GaAs plate sample, turning the SFG microscopy images into precious data.*

The images A and D display 100 μm squares with respectively a 8x and 6x magnification; the B presents 100 μm horizontal stripes with M = 12x; the C shows

100 μm vertical stripes with M = 15x; and finally the E illustrates 10 μm vertical stripes with M = 20x. As a matter of fact, the contrast is weaker than the one obtained on the GaAs plate.

8.5 SFG imagery of other molecules

With the goal to apply the SFG microscopy to biochemical systems studied in our laboratory, other vibrational signatures have been investigated. We have tried to record interfacial signatures in the 7 μm infrared range, first because this is a high challenge in the SFG microscopy field, and second because samples such as patterned lipid layers require such mid IR wavelength to be studied (as seen in chapter 7).

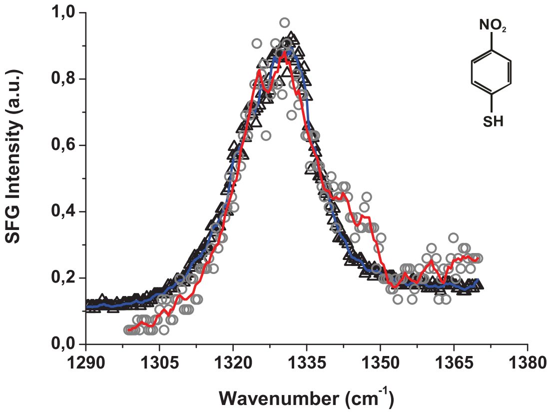

Figure 8.6: *SFG spectrum of NTP film onto platinum in ppp polarization set. The blue curve is the spectrum of a flat NTP film prepared by immersion, while the red one is a backfilling of NTP between printed DDT lines sizing 100* μ*m. The mode at 1330 cm*$^{-1}$ *is the* NO_2 *symmetric stretching.*

With the underlying idea to work with lipid patterned films, the laser IR OPO was set up with type I $AgGaS_2$ crystal (blue power curve in figure 8.2). The purpose was to be able to record both 3 and 7 μm range vibrational signature of the sample, one measurement performed straight after the other, leading to a coherent set of SFG spectra. The prepared sample is a 4-nitrothiophenol molecule (NTP - shown in figure 8.6) printed on a Pt substrate.

The NO_2 symmetric stretching mode is located at 1330 cm^{-1}, as shown by SFG spectroscopy (performed on the same laser system as the microscopy) in figure 8.6. Along with unpatterned NTP sample (blue curve), a SFG spectrum of a patterned NTP film presenting 100 μm stripes is shown (red curve). To realize this latter sample, we have firstly print DDT lines by μcp, with 100 μm space inbetween them. In a second step, we have done a backfilling of NTP (immersion of the sample in a 1 mM solution for 1 hour). This lead to a more stable layer because the substrate is entirely covered, what would not be the case if we had only printed the NTP directly on the clean platinum.

Except that intensities have been normalized, the spectral signature shapes are close to each other, validating the patterning method through backfilling process. In figure 8.7 are presented the SFG images matching the spectra of figure 8.6 and recorded in ppp polarization set at 1330 cm^{-1}. While the visible power is still high (100 mW - 532 nm), the infrared one is much lower (12 mW - 7,7 μm). This results consequently in longer imaging acquisition durations (100 s), what leads to a higher optical polution of the SFG signal and thus to less contrasted images.

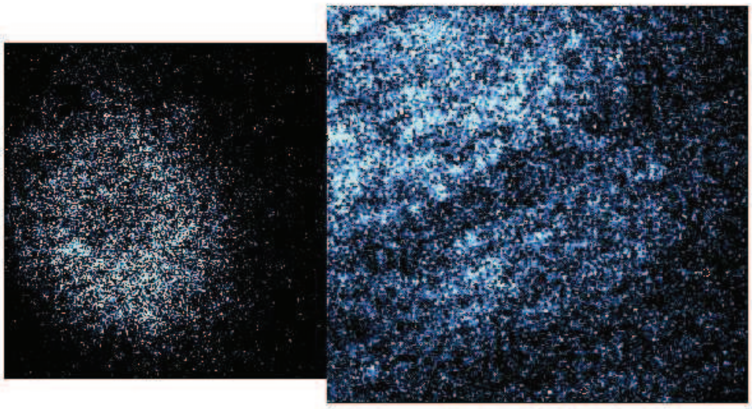

Figure 8.7: *SFG microscopy imaging of NTP flat film (left) and patterned film (backfilling over 100 μm DDT line shaped patterns).*

The left side image of the figure 8.7 is the one of a flat NTP film. We see the circular laser spot shape which is very focussed at the interface because of the weak IR power. The right side image shows 100 μm line patterns realized through backfilling chemisorption of NTP inbetween DDT stripes. Those are to our knowledge, among the first SFG images obtained in the 7 μm range, not to mention the spatial patterning.

8.6 Perspectives

This chapter presents the first SFG microscopy images realized with our new laser-microscope set up. The image acquisition represents a very first step initiated only a few months ago. Besides technical difficulties that had to be overcome (those latter requiring always longer than firstly estimated...), the system has reached a certain maturity allowing now to spend more time on imaging samples than on set up adjustments (this step actually spreads over more than one year).

This encouraging breakthrough a very recent science field application has now to be further explored. Many biochemical systems/devices are targeted for SFG microscopy, much of them having been well characterized by SFG spectroscopy. The sole micro-contact printing method coupled with SFG microscopy involves a lot of interesting model devices based on patterned structures to be investigated. This may be even more extended since stamp tools turn out to be compatible with amphiphilic/lipid molecules. This allows to realize a broad range of solid supported patterned films realized from a Langmuir-Blodgett apparatus.

The information that may be retrieved from SFG microscopy is nothing else than spatially resolved spectroscopy, fully able to provide the conformation of specific chemicals as well as their orientations. These data are precious since very few techniques are able to characterize the molecular conformation from symmetry considerations, along with a spatial resolution ability dedicated to interfaces. Other topics like supported metallic nanoparticles are very interesting for microscopy studies since they reinforced SFG signals and materialized an adequate platform for more complex chemical functionalizations [Tourillon et al., 2007]. We may also consider to investigate the spatially resolved SFG response of DNA samples, biotin-avidin specific recognition, antigen-antibody binding through lipid layers (such as DNP), as long as the SFG intensity is not too weak.

8.7 Resume

This chapter was dedicated to the SFG microscopy imaging technique. After having introduced the necessity of high intensity IR and visible beams, requiring a state of the art laser set up, we have described the technical upgrade realized on our new microscope system in comparison with the first set up allocated to spectroscopic measurements. A more efficient amplification step enables to obtain a more intense pump beam, and consequently a higher intensity output from both OPOs. The second part was devoted to the image acquisition principle. The CCD device as well as the intermediate optics (a single lens) have been described and positioned to get clear SFG image of the sample surface. We have seen that for a lens of given focal length, the distance between the sample and the CCD defines the magnification as well as a precise lens position to obtain a clear SFG image. We have then applied the method to a GaAs sample because of its strong non resonant background, after what DDT patterned films have been imaged. Finally, we have broadened the spectral region of investigation to nitrothiophenol layers in the 7 μm range. Spectrum and images of symmetric NO_2 stretching vibrations have been obtained for flat and patterned films. This work opens the way to novel investigations in many field of surface sciences.

8.8 Bibliography

[Cimatu and Baldelli, 2006a] Cimatu, K. and Baldelli, S. (2006a). Sum frequency generation imaging microscopy of co on platinum. Journal of the American Chemical Society, 128(50):16016–16017.

[Cimatu and Baldelli, 2006b] Cimatu, K. and Baldelli, S. (2006b). Sum frequency generation microscopy of microcontact-printed mixed self-assembled monolayers. Journal of Physical Chemistry B, 110(4):1807–1813.

[Cimatu and Baldelli, 2007] Cimatu, K. and Baldelli, S. (2007). Spatially resolved surface analysis of an octadecanethiol self-assembled monolayer on mild steel using sum frequency generation imaging microscopy. Journal of Physical Chemistry C, 111(19):7137–7143.

[Cimatu and Baldelli, 2008] Cimatu, K. and Baldelli, S. (2008). Chemical imaging of corrosion: Sum frequency generation imaging microscopy of cyanide on gold at the solid-liquid interface. Journal of the American Chemical Society, 130(25):8030–8037.

[Cimatu et al., 2008] Cimatu, K., Moore, H. J., Barriet, D., Chinwangso, P., Lee, T. R., and Baldelli, S. (2008). Sum frequency generation imaging microscopy of patterned self-assembled monolayers with terminal -ch3, -och3, -cf2cf3, -c = c, -phenyl, and -cyclopropyl groups. Journal of Physical Chemistry C, 112(37):14529–14537.

[Cimatu et al., 2007] Cimatu, K., Moore, H. J., Lee, T. R., and Baldelli, S. (2007). Sum frequency generation imaging of microcontact-printed monolayers derived from aliphatic dithiocarboxylic acids: Contrast based on terminal-group orientation. Journal of Physical Chemistry C, 111(32):11751–11755.

[Flörsheimer et al., 1999] Flörsheimer, M., Brillert, C., and Fuchs, H. (1999). Chemical imaging of interfaces by sum frequency microscopy. Langmuir, 15(17):5437–5439.

[Fu et al., 2007] Fu, Y., Wang, H. F., Shi, R. Y., and Cheng, J. X. (2007). Second harmonic and sum frequency generation imaging of fibrous astroglial filaments in ex vivo spinal tissues. Biophysical Journal, 92(9):3251–3259.

[Hedberg et al., 2007] Hedberg, J., Leygraft, C., Cimatu, K., and Baldelli, S. (2007). Adsorption and structure of octadecanethiol on zinc surfaces as probed by sum frequency generation spectroscopy, imaging, and electrochemical techniques. Journal of Physical Chemistry C, 111(47):17587–17596.

[Hoffmann et al., 2002] Hoffmann, D. M. P., Kuhnke, K., and Kern, K. (2002). Sum-frequency generation microscope for opaque and reflecting samples. Review of Scientific Instruments, 73(9):3221–3226.

[Ji et al., 2006] Ji, N., Zhang, K., Yang, H., and Shen, Y. R. (2006). Three-dimensional chiral imaging by sum-frequency generation. Journal of the American Chemical Society, 128(11):3482–3483.

[Kuhnke et al., 2003] Kuhnke, K., Hoffmann, D. M. P., Wu, X. C., Bittner, A. M., and Kern, K. (2003). Chemical imaging of interfaces by sum-frequency generation microscopy: Application to patterned self-assembled monolayers. Applied Physics Letters, 83(18):3830–3832.

[Lis and Peremans, 2005] Lis, D. and Peremans, A. (2005). Development of an all-solid-state picosecond laser generating high-energy impulsion at low repetition rate for pumping optical parametric generator and amplifier (opg/opa). Master Thesis.

[Mani, 2004] Mani, A. (2004). Development of a sum-frequency generation spectrometer. Thesis.

[Shen et al., 2000] Shen, Y. Z., Swiatkiewicz, J., Winiarz, J., Markowicz, P., and Prasad, P. N. (2000). Second-harmonic and sum-frequency imaging of organic nanocrystals with photon scanning tunneling microscope. Applied Physics Letters, 77(19):2946–2948.

[Tourillon et al., 2007] Tourillon, G., Dreesen, L., Volcke, C., Sartenaer, Y., Thiry, P. A., and Peremans, A. (2007). Total internal reflection sum-frequency generation spectroscopy and dense gold nanoparticles monolayer: a route for probing adsorbed molecules. Nanotechnology, 18(41).

Conclusions and perspectives

This thesis focuses on the study of interfaces by second-order optical mechanisms (SFG and SHG, spectroscopy and microscopy). The first three chapters are dedicated to a theoretical review of the tools needed for subsequent experimental data processing. In a few words, after a validation of the dipolar approximation, the second-order electrical susceptibility $\chi^{(2)}$ has been designated as the key factor in such nonlinear optical activity. However, it is demonstrated that this susceptibility vanishes in centrosymmetric materials, meaning that excluding a few crystalline classes, interfaces are dedicated locations for those nonlinear effects to occur. Simplifications are further performed on the susceptibility tensor regarding interfacial symmetries, what finally leads to only four significant tensor components for second-order optical effects. From those latter components, we have set up mathematical expressions to describe the experimentally measured nonlinear intensities, this as well for SFG and SHG mechanisms. By comparison with experimental data, this enables a quantification of the second-order susceptibility tensor $\chi^{(2)}$, however only under certain conditions such as the use of specific polarization combinations of the beams.

In the cases of one successful quantification of the four components, a method allowing to retrieve molecular orientations is presented for both SFG and SHG. However, the latter is based on the assumption of one/few dominant second-order polarizability component(s) $\beta^{(2)}_{ijk}$ which involves practical limitations that turn this way to proceed quite restrictive. This fact underlines the necessity to a complete quantification of the second-order polarizability tensor $\beta^{(2)}$, which would allow the full determination of the molecular orientation for a broad panel of experimental configurations. In this context, to understand the origin of this nonlinear polarizability $\beta^{(2)}$ and to be able to calculate its element values, quantum mechanical considerations are presented in the third chapter. Those latter reveal the different resonant processes and allow to distinguish the SFG from the SHG mechanisms. The global theoretical background, summarized in the first three chapters, constitutes a support to extract informations from experimental data presented in the five subsequent chapters.

The first experimental part focuses on a SHG work realized at the University of Illinois in the frame of a scientific fellowship program. A liquid-solid interaction is observed through the reorientation of molecules physisorbed at the interface while under a liquid flow. The specific surface sensitivity of the second-order spectroscopy allows confining the observation within a nanometre layer adjacent to the interface, which turns this work very novel in the field. This study was a first test to validate the use of nonlinear optics for such fluid dynamics applications. Beyond those results, stand many perspectives of future works based on a wider range of surfaces, liquids, molecule species and broader physical constraints.

In the fifth chapter, we have briefly presented the SFG spectrometer as well as the OPOs principle to tune the laser optical frequencies. Next, the real strength and specificity of the SFG spectroscopy have been demonstrated through, on the one hand, the structural characterization of interfacial model monolayers, and on the other hand, the complete orientation determination of the involved molecules. Those results rely on many theoretical principles exposed in the first chapters and demonstrate the potentiality of nonlinear spectroscopies in the study of biochemical interfaces. Experimentally speaking, among a few ways to build-up self-assembled monolayers on solid substrates, immersion and micro-contact printing methods are compared regarding the structural quality of the as produced films. This work shows that μcp method is very efficient to form highly organized molecular films with micrometric patterns, all this within one second of print duration.

This ability to produce patterns of organized molecules being of high potential applications, it has been tested with several molecules, and more particularly, combined with Langmuir-Blodgett methods. Those latter, being specifically designed to build-up solid supported films of amphiphilic species (such as lipid entities), allow therefore to set up membrane-like model layers. After reviewing the LB techniques, we have successfully combined them with μcp to produce patterns of supported lipid films. Two patterning methods leading to two distinct layer configurations are demonstrated with DNP lipid molecules, this latter holding real antigenic properties.

Finally, in order to carry out a spatially resolved study of those various molecular patterns, a new SFG microscopy experiment is developed. We first expose the novelty of the involved technology, as well for the laser set up as for the CCD detection. Imaging processes are explained and demonstrated on a reference sample (GaAs), after what, images of real samples in the 3 μm and 7 μm ranges are recorded as well. The results exposed represent an achievement after two years of laser and CCD developments. Among the very few SFG microcopes set up in the world, our state of the art device should allow us to obtain highly significant scientific results in the spectroscopy/microscopy domain. Besides, the high potential and compatibility of the μcp method provide a wide panel of applications for SFG imaging technique. Everything remains to be done in this field!

Publications

Y. Sartenaer, G. Tourillon, L. Dreesen, **D. Lis**, A.A. Mani, P.A. Thiry, A. Peremans, *Sum-frequency generation spectroscopy of DNA monolayers*, Biosensors & Bioelectronics, 2007, 22, 2179-2183

D. Lis, A. Peremans, Y. Sartenaer, Y. Caudano, A.A. Mani, L. Dreesen, P.A. Thiry, J. Guthmuller, B. Champagne, F. Cecchet, *Self-Assembled Film Organization in Fast Microcontact Printing Investigated by Sum Frequency Generation Spectroscopy*, Journal of Physical Chemistry C, 2009, 113, 9857-9864

J. Guthmuller[1], F. Cecchet[2], **D. Lis**[2], Y. Caudano[2], A.A. Mani[2], P.A. Thiry[2], A. Peremans[2], B. Champagne[1], *Theoretical simulation of vibrational sum-frequency generation spectra from density functional theory: Application to p-nitrothiophenol and 2,4-dinitroaniline*, ChemPhysChem, 2009, 10, 12, 2132-2143

F. Cecchet[1], **D. Lis**[1], J. Guthmuller[2], B. Champagne[2], Y. Caudano[1], C. Silien[1], A.A. Mani[1], P.A. Thiry[1], A. Peremans[1], *Orientational analysis of dodecanethiol and p-nitrothiophenol SAMs on metals with polarisation-dependent SFG spectroscopy*, ChemPhysChem, in press

A. Peremans[1,4], **D. Lis**[1], F. Cechet[1], P. G. Schunemann[2], K. T. Zawilski[2], and V. Petrov[1], *Non-critical singly resonant synchronously pumped OPO for generation of picosecond pulses in the mid-infrared near 6.4 vm*, Optics Letters, 2009, 34, 20, 3053

A.A. Mani, **D. Lis**, L. Grawet, L. Dreesen, P.A. Thiry, A. Peremans, Ch. Silien, *High energy and short pulses generation by Nd:yttrium aluminum garnet laser mode-locked using frequency-doubling nonlinear mirror*, Optics communications, 2007, 276, 135-138

A.A. Mani[1], A.K. Jazmati[1], M.D. Zidan[1], F.G. Awad[1], L. Dreesen[2], Y. Caudano[2], C. Silien[2], Y. Sartenaer[2], **D. Lis**[2], L. Lamard[2], P.A. Thiry[2], A. Peremans[2], *Development of an all-solid-state pulsed picosecond laser system for nonlinear spectroscopy*, Physical & Chemical News, 2007, 36, 10-18

F. Cecchet[1], **D. Lis**[1], J. Guthmuller[2], B. Champagne[2], G. Fonder[3], Z. Mekhalif[3], Y. Caudano[1], A.A. Mani[1], P.A. Thiry[1], A. Peremans[1], *Theoretical Calculations and Experimental Measurements of the Vibrational Response of p-NTP SAMs: An Orientational Analysis*, Journal of Physical Chemistry C, submitted

D. Lis[1], A. Peremans[1], B. Sung Chul[2], S. Granick[2], *Liquid stress at surfaces probed by second harmonic generation spectroscopy*, Langmuir, to submit